The Dissertation Committee for Vishwanath Haily Dalvi certifies that this is the approved version of the following dissertation:

Molecular Dynamics Study of Solvation Phenomena to Guide Surfactant Design

Committee:

____

Peter J. Rossky, Supervisor

____

Keith P. Johnston

____

Brian A. Korgel

____

Thomas M. Truskett

____

Graeme Henkelman

Molecular Dynamics Study of Solvation Phenomena to Guide Surfactant Design

by

Vishwanath Haily Dalvi, B.Chem.Engg., M.S.

Dissertation

Presented to the Faculty of the Graduate School of

the University of Texas at Austin

in Partial Fulfillment

of the Requirements

for the Degree of

Doctor of Philosophy

The University of Texas at Austin

December, 2009

Dedicated to Gopal Chavan whose servant heart best reflects the nature of our Lord Jesus Christ.

Acknowledgements

This thesis is at least as much a result of the insights and sage advice of my advisor, Dr. Peter Rossky, as it is due to any of my efforts. I would like to thank Dr.Vibha Srinivasan for giving me a strong start, John Dowdle for his patient encouragement and discussions, Dr. Sangik Cho for his help with difficult calculations, and the other members of the Rossky group. I am also especially grateful for the discussions with Dr. Truskett as well as Gaurav Goel and Dr. Jeetain Mittal, both of the Truskett group. I really appreciate the support of Dr. Keith Johnston and Dr. Brian Korgel in terms of time as well as resources as I do the time given by Dr. Graeme Henkelman to serve on my committee. And none of this work would have been possible without the Texas Advanced Computing Center's generosity with the use of the Lonestar cluster for which I am deeply thankful. I am also grateful for the work done by T. Stockman, Kay Swift and Sylvia Jean to make for a hassle-free and delightful time at the University of Texas. And for all these blessings and others besides let it be said: *Soli Deo Gloria.*

Molecular Dynamics Study of Solvation Phenomena to Guide Surfactant Design

Vishwanath Haily Dalvi, Ph.D.

The University of Texas at Austin, 2009

Supervisor: Peter J. Rossky

Supercritical carbon-dioxide has long been considered an inexpensive, safe and environmentally benign alternative to organic solvents for use in industrial processing. However, at readily accessible conditions of temperature and pressure, it is by itself too poor a solvent for a large number of industrially important solutes and its use as solvent necessitates concomitant use of surfactants. Especially desirable are surfactants that stabilize dispersions of water droplets in carbon-dioxide. So far only molecules containing substantially fluorinated moieties e.g. fluoroalkanes and perfluorinated polyethers, as the CO_2-philes have proved effective in stabilizing dispersions in supercritical carbon-dioxide. These fluorocarbons are expensive, non-biodegradable and can degrade to form toxic and persistent environmental pollutants. Hence there is great interest in developing non-fluorous alternatives. Given the development of powerful computers, excellent molecular models and standardized molecular simulation packages we are in a position to augment the experiment-driven search for effective surfactants using the nanoscopic insights gleaned from analysis of the results of molecular simulations. We have developed protocols by which to use standard and freely available molecular simulation infrastructure to evaluate the effectiveness of surfactants that stabilize solid metal nanoparticles in supercritical fluids. From the results, which we validated against experimental observations, we were able to determine that the alkane-based surfactants, that are so effective in organic fluids, are ineffective or only partially effective in CO_2 because the weak C-H dipoles cannot make up for the energetic penalty incurred at the surfactant-fluid interface by CO_2 molecules due to loss of quadrupolar interactions with other CO_2 molecules. Though the effectiveness of purely alkane-based surfactants in carbon-dioxide can be improved by branching, they cannot approach the effectiveness of the fluoroalkanes. This is because the stronger C-F dipole can supply the required quadrupolar interactions and a unique geometry renders repulsive the fluorocarbons' electrostatic interactions with each other. We have also determined the source of the fluoroalkanes' hydrophobicity to be their size which offsets the effect of favourable electrostatic interactions with water. Hence we can provide guidelines for CO_2-philic yet hydrophobic surfactants.

Table of Contents

List of Tables

List of Figures

Chapter 1: Introduction

The motivation for this work comes from the continuing appeal (Johnston & da Rocha, 2009) of substituting flammable and often toxic organic solvents with the non-toxic, non-flammable and environmentally benign supercritical carbon dioxide ($ScCO_2$) for various industrial processes. Unfortunately $ScCO_2$ at ambient temperature and at a pressure less than 500 atm is too poor a solvent for a large number of industrially important solutes to be competitive with industrially used solvents and the effort to develop surfactants to stabilize liquid droplet emulsions in $ScCO_2$ is of considerable academic interest. Water-in-CO_2 emulsions are particularly desirable since they find wide application e.g. in enhanced oil recovery (Rossen, 1996), biology (Johnston, et al., 1996)(Harrison, Goveas, Johnston, & O'Rear, 1994), "green" chemistry (DeSimone, 2002) (Sagisaka, et al., 2008). Although attempts have been made to apply molecular simulations to gain insights into surfactant action at CO_2-water interfaces (da Rocha, Johnston, & Rossky, 2002) (Stone, da Rocha, Rossky, & Johnston, 2003), the problem of simulation of a fluid-fluid interface is one fraught with considerable difficulty. As a means to gain some headway, it was proposed to tackle the important, but rather simpler, problem of investigating surfactants (or passivating ligands as they are known) at *solid*-fluid interfaces particularly with a view to understanding the mechanism of stabilization of colloidal dispersions of ligand-passivated metal nanoparticles in $ScCO_2$.

As an illustration of the problem with use of $ScCO_2$ as solvent, we note a puzzle: Metal nanoparticles passivated by cheap and benign ligands e.g. dodecanethiol, disperse quite well in organic liquids like toluene (Brust, Walker, Bethell, Schiffrin, & Whyman, 1994) and n-hexane (Shah, Holmes, Doty, Johnston, & Korgel, 2000) (Anand, et al., 2008) and in organic supercritical solvents like supercritical ethane (Clarke, Waters, Johnson, Satherley, & Schiffrin, 2001) (Shah, Holmes, Johnston, & Korgel, 2002). However, in $ScCO_2$, under comparable conditions of temperature and pressure, these same nanoparticles would flocculate. In fact, CO_2 acts as an *anti*-solvent for dodecanethiol passivated nanoparticles (Gupta, Shah, Zhang, Saunders, Korgen, & Johnston, 2005) (Anand, et al., 2008) as well as organic-polymeric nanoparticles (Chang, Lee, & Lin, 2007) (Dixon, Johnston, & Bodmeier, 2004) dispersed in organic liquids. It was only the particles passivated with perfluorinated short-chain alkanes (Shah, Husain, Johnston, & Korgel, 2002) or perfluoropolyethers (Saunders & Korgel, 2004) that formed stable dispersion in $ScCO_2$. Similarly, fluorinated moieties stabilize emulsions of organic liquids (DeSimone & Wells, 2001) and water droplets (Keiper, Simhan, & DeSimone, 2002) in $ScCO_2$.

The ultimate goal of the endeavour of which this work is a part, is to develop non-fluorous surfactants to stabilize droplets of water or organic-liquids in $ScCO_2$ at ambient temperature and less than 500 atm pressure. We seek to avoid use of fluorinated moieties because these are expensive, practically xenobiotic (Resnati, 1993) and their degradation products are persistently toxic (Pelley, 2004). The search for such non-fluorous ligands is of continuing interest (Sarbu, Styranec, & Beckman, 2000)(Potluri, Xu, Enick, Beckman, & Hamiltion, 2002) (Anand, Bell, Fan, Enick, & Roberts, 2006) (Patel & Egorov, 2007) we seek to augment that search by using molecular simulations to gain physical insight into the mechanism of stabilization/solvation, which we will then use to develop guidelines for the design of experiments.

From that perspective, the dissertation is organized as follows:

In Chapter 2 we describe in detail the simulation and analytical protocol by which ligands are gauged for their effectiveness in stabilizing passivated solids in supercritical fluids. We use this in that same chapter to compare the effectiveness of n-dodecanethiol ligand in $ScCO_2$ and supercritical ethane and present an explanation for this phenomenon.

In Chapter 3 we apply the same method to the study of the solids passivated by perfluoroalkane moieties and solvated by $ScCO_2$. We identify the causes for the effectiveness of perfluorinated groups and suggest strategies to incorporate them with non-fluorous systems.

In Chapter 4 we analyse ligands with branched-alkane moieties that have proved to be partially effective in $ScCO_2$.

Finally in Chapter 5, we turn our attention to the other fluid-phase of interest i.e., water. There we use molecular simulations to study the difference between hydration of a hydrocarbon solute and its perfluorinated analogue. We also study the interaction of water with various hydrophobic surfaces.

The insights we have gained from this work can now be used to guide the design/screening of non-fluorous surfactants for water in CO_2 emulsions.

Chapter 2: Hydrocarbon Ligands for Nanoparticle Dispersions

2.1 Introduction

In the processing of nanoparticles, it is important to have reversible control on the stability of their colloidal dispersions (Murray, Norris, & Bawendi, 1993). Because their solvation power is a strong function of pressure, supercritical fluids promise to be excellent solvents for nanoparticle-processing not least due to their ability to afford *reversible* solvation which offers a great advantage over anti-solvent methods (Shah, Holmes, Johnston, & Korgel, 2002). Supercritical carbon-dioxide (ScCO_2) with its easily accessible critical condition, non-flammability and non-toxicity, would be especially suitable for large scale use. However nanoparticles of many interesting materials, e.g. metals, semi-conductors etc, need their surfaces to be passivated by capping ligands in order that they may disperse in common solvents under reasonably accessible conditions of temperature and pressure (Shah, Hanrath, Johnston, & Korgel, 2004). It is found that metal nanoparticles passivated by cheap and benign hydrocarbon ligands, e.g. short-chain alkanethiols, disperse effectively in organic liquids like toluene (Brust, Walker, Bethell, Schiffrin, & Whyman, 1994) and n-hexane (Shah, Holmes, Doty, Johnston, & Korgel, 2000) (Anand, et al., 2008) and in organic supercritical solvents like supercritical ethane (Clarke, Waters, Johnson, Satherley, & Schiffrin, 2001) (Shah, Holmes, Johnston, & Korgel, 2002). However, they remain flocculated in supercritical carbon-dioxide (Shah, Holmes, Doty, Johnston, & Korgel, 2000) (Anand, et al., 2008) under similar conditions. Capping ligands that have proved effective in dispersing nanoparticles in supercritical carbon-dioxide (ScCO_2) are, most commonly, perfluorinated short-chain alkanes (Shah, Husain, Johnston, & Korgel, 2002) or perfluoropolyethers (Saunders & Korgel, 2004). However, these ligands are expensive, practically xenobiotic (Resnati, 1993) and their oxidation products are persistently toxic (Pelley, 2004). In anticipation of future industrial scale processing of nanoparticles, there is interest in developing non-fluorous ligands that can effectively disperse nanoparticles in ScCO_2 (Sarbu, Styranec, & Beckman, 2000)(Potluri, Xu, Enick, Beckman, & Hamiltion, 2002) (Anand, Bell, Fan, Enick, & Roberts,

2006) (Patel & Egorov, 2007). Furthermore, insights gained from this endeavour can be readily applied to better understand how surfactants stabilize CO_2-water emulsions which are important for enhanced oil recovery (Rossen, 1996), biology (Johnston, et al., 1996)(Harrison, Goveas, Johnston, & O'Rear, 1994), “green” chemistry (DeSimone, 2002) (Sagisaka, et al., 2008) and other applications (Johnston & da Rocha, 2009).

Here we seek to understand the physical phenomena governing the stability of ligand-passivated-nanoparticle dispersions using atomistic molecular-dynamic (MD) simulations**.** We report our method in detail and make the case for its applicability in capturing the relevant physics. We also report our investigation of the effectiveness of the popular hydrocarbon ligand n-dodecanethiol in stabilizing nanoparticle dispersions in supercritical CO_2 and supercritical ethane, with the latter taken as representative of organic solvents.

Where the relevant data are available, we find excellent consistency of the simulation results with experimental observations. From the results, we have shown that the reason that dodecanethiol ligands are so effective in ethane and yet so ineffective in $ScCO_2$ is not just that they interact more strongly with ethane but also that CO_2, being smaller and possessing a fairly strong quadrupole, is more *autophilic* than ethane. Hence CO_2 has a *relatively* weaker affinity for the hydrocarbon ligands, compared to its own bulk, than ethane does. We have therefore concluded that if a ligand is to be effective in $ScCO_2$, its passivation layers on the nanoparticle surfaces should provide the interactions necessary to adequately compensate CO_2 not only for the loss of its van der Waals interactions with its bulk but also for its quadrupolar i.e. electrostatic interactions.

This paper is organized as follows: The relevant experimental observations are summarized in Section 2.2, the simulation strategy and setup in Section 2.3 and the results are reported and discussed in Section 2.4.

2.2 Experimental Observations

The experimental observations relevant to this work are: dodecanethiol passivated metal nanoparticles disperse in supercritical ethane but not in supercritical CO_2 at comparable conditions of temperature and pressure.

(a) It is found that dodecanethiol-capped silver nanocrystals do not disperse in $ScCO_2$ even at very high pressures (> 300 atm). However they disperse if n-hexane is added as a co-solvent in substantial amounts (>50%v/v) (Shah, Holmes, Doty, Johnston, & Korgel, 2000). Further, CO_2 is actually found to be an *anti*-solvent for dodecanethiol passivated nanoparticles (Gupta, Shah, Zhang, Saunders, Korgen, & Johnston, 2005) (Anand, et al., 2008) as well as organic-polymeric nanoparticles (Chang, Lee, & Lin, 2007) (Dixon, Johnston, & Bodmeier, 2004) dispersed in organic liquids.

(b) Dodecanethiol passivated gold nanoparticles were dissolved in supercritical ethane (Clarke, Waters, Johnson, Satherley, & Schiffrin, 2001), and a size selective dispersion by tuning solvent density (varying pressure between 138-414 atm at temperatures between 25-65^{o}C) was shown to be feasible for gold and silver nanoparticles stabilized by dodecanethiol (Shah, Holmes, Johnston, & Korgel, 2002). It was found that nanoparticles with diameters greater than 60Å flocculated at an ethane pressure of 312 atm at 308K.

2.3 Simulation Strategy and Computational Details

The goal of the method described in this paper is to determine how well a certain ligand-solvent set stabilizes a nanoparticle dispersion in that solvent compared to other ligand-solvent sets and then to determine the sources of the difference at the molecular level. We propose doing so using all-atom molecular dynamic simulations. If our simulations can reasonably reproduce the experimental observations, we can be confident that the relevant physical phenomena have been captured. Subsequent analysis of the molecular level causes of the behaviours can then be carried out. To obtain comparable insight by direct observation of experimental systems would require extraordinary ingenuity (Saunders, Shah, Park, Lim, Johnston, & Korgel, 2004).

This section is organized in sub-sections providing increasing levels of detail. Hence, in the the first sub-section, we propose a metric to quantify "effectiveness" and describe the hypothetical experiment by which to determine it. In the next sub-section we describe the conceptual design of the simulation scheme to realise the experiment via simulations. The third sub-section deals with the generation and processing of the primary data, i.e., data obtained from the simulations. It is only in the fourth sub-section that we describe the details of the molecular models and computational methods that we have employed.

2.3.1 Free Energy of Flocculation and Thought-Experiment to find it

To introduce our proposed metric by which various ligand-solvent combinations may be equitably compared with each other for their effectiveness in stabilizing dispersions of passivated nanoparticles, we construct the following thought-experiment. We imagine a pair of identical nanoparticles that are passivated by a certain type of ligand and placed in a large container at a fixed *large* distance or separation from each other. By "distance/separation", which we denote by *L*, we mean the separation between the surfaces of the nanoparticle *cores* and *not* the centre-to-centre distance *nor* the distance between ligand tips. We can also call this the *gap-width*. We fill the container with a solvent of our choice, which for this paper will be either CO_2 or ethane. The solvent is at a bulk pressure (P_{bulk}) and temperature (T) where it is supercritical. The separation between the particles is initially so large that there exists no appreciable *net* force on either of them. Now we bring the particles together *reversibly* while always noting the relationship between the average force between the particles and the interparticle separation. This allows us to integrate the forced data and thus calculate the potential-of-mean-force (PMF) between the particles as a function of separation for a given pressure, temperature and ligand-solvent set. At the equilibrium separation L_{eq}, the PMF is minimum and this value is denoted by $\mathcal{W}$, which we call the *free-energy of flocculation*. This is our metric of effectiveness and it is a function of bulk solvent pressure, temperature, nanoparticle diameter and the ligand-solvent set. We can equitably compare $\mathcal{W}$ for different ligand-solvent sets for a fixed nanoparticle core diameter, bulk solvent pressure and temperature. The more positive this number is, the more effective is the ligand-solvent system.

2.3.2 Conceptual Design of Simulation Setup to realise Thought-Experiment

The most straightforward method of simulating the thought-experiment would be to place two ligand-passivated nanoparticles in a very large simulation cell filled with explicit solvent molecules and calculate the mean-force between the particles for various values of L at a fixed pressure and temperature. Experimentally, the greatest difficulty has been encountered in stabilizing dispersions of large particles with core diameters >30Å (Clarke, Waters, Johnson, Satherley, & Schiffrin, 2001) (Anand, Bell, Fan, Enick, & Roberts, 2006) and the test of an effective ligand in a given solvent would be its ability to stabilize dispersions of large nanoparticles in that solvent. While there exist atomistic simulations of small core diameter (~10Å) nanoparticles in explicit solvent (Patel & Egorov, 2007), it would be infeasible to simulate a sufficiently dilute dispersion of just two ligand-passivated nanoparticles of approx. 60Å diameter, as shown schematically in Figure 2.1a, with explicit solvent; it would require a periodic box containing approximately 100,000 atoms. However, our ambition, which is to develop a general understanding of the phenomena involved, is relatively modest and we therefore feel justified in making an approximation to the full problem. Our conjecture, justified by our results, is that the physics of the solvated interactions between two passivated nanoparticles is influenced mostly by the confined region between them. A schematic of this region appears in Figure 2.1b. We can therefore gain molecular-level insight into the physical phenomena related to stability of ligand-passivated nanoparticle dispersions using a *slit-pore* geometry. Although the term “slit-pore” is conventionally used to indicate that the surfaces are planar, we simulate bumpy surfaces. This is to better approximate solvated interactions between the curved surfaces of two 60Å core-diameter ligand-passivated nanoparticles. The number of atoms per periodic box is now well under 10,000, and the computations are feasible. The Figure 2.1c shows a VMD (Humphrey, Dalke, & Schulten, 1996) visualization of a periodic cell of the simulation *sans* solvent.

To relate the results of the slit-pore simulations to interactions between two nanoparticles, we attribute the interactions within a single periodic image to a single pair of nanoparticles. Hence the “wall” of the slit-pore within a periodic image can now be interpreted as the “cheek” of one of the nanoparticles. Molecular simulations in slit-pore type geometries have been used to understand behavior of polymer-brush type passivation (Meredith, Sanchez, Johnston, & de Pablo, 1998) and also to study surfactant stabilized water-CO_2 interfaces (da Rocha, Johnston, & Rossky, 2002) (Stone, da Rocha, Rossky, & Johnston, 2003).

The use of slit-pore geometry, rather than simulating whole nanoparticles, introduces the complication that the simulation system itself does not contain a “bulk” region. Since the experiment we endeavour to simulate requires knowledge of mean-force of interaction between the (pseudo)nanoparticles at different separations but at equilibrium with *constant* bulk conditions, it is essential to know what bulk condition a given pore-solvent-density corresponds to. There are simulations which have attempted to include an explicit bulk-region connected to the slit pore region (Gao, Luedtke, & Landman, 1997). In that approach the bulk properties corresponding to a given confinement density are directly available but at the cost of a higher number of simulated particles. While these are good for simulating solvents, e.g. medium chain alkanes, whose excess chemical potentials are difficult to calculate, for simple solvent molecules like CO_2 or ethane an explicit bulk is not necessary. Instead we can connect bulk-solvent density to confined-solvent density using the knowledge that at equilibrium, the activity of solvent in the bulk (ξ_{bulk}) is the same as its activity in the pore.

The mean-force of interaction between the walls of the slit-pore in a single periodic simulation cell, which is also to be understood as the mean-force of interaction between the two nanoparticles of the thought-experiment, is simply the sum of the normal forces acting on the “wall-atoms” of any one wall of a periodic image of the slit-pore averaged over a full simulation. The wall-atoms are atoms that define the walls of the slit-pore and are rigidly held in place during a simulation.

Since the calculation of the PMF requires mean-force data for various values of *L* at constant activity, the most natural ensemble to carry out the simulation is the grand-canonical ensemble i.e. one in which volume, temperature and solvent-activity are externally imposed and mean-force and solvent-density are determined from the simulation (Frenkel & Smit, 2002). However, since we seek results over a wide range of bulk conditions, we have developed an efficient procedure to calculate PMF and hence $\mathcal{W}$ using canonical-ensemble simulations i.e. where volume, temperature and solvent-density are imposed while mean-force and solvent-activity are determined from the simulation. This procedure is described in the next section.

2.3.3 Generation of primary data and post-processing to obtain $\mathcal{W}$

In this section we describe the type of primary data to be generated and its post-processing.

2.3.3.1 Generation and fitting of primary data

We perform three types of simulations to obtain our primary data:

(a) Canonical ensemble simulations at different values of *L* and pore-solvent densities ($\rho_{pore}=N_{pore}/A_{pore}/L$ where N_{pore} is the number of solvent molecules in a single periodic image of the pore and A_{pore} is the corresponding cross sectional area) to obtain the mean-force within the solvated pore. In order to facilitate processing of this quantity we have chosen to recast it as normal *pressure* in the pore (P_{pore}) obtained by dividing the averaged mean-force on one wall of the simulation cell by its cross-sectional area. While the system is being simulated and after it has equilibrated, we store snapshots of the system configurations at regular intervals for use in the calculation of solvent-activity in pore. For a fixed value of *L* we have found that in the density range of our interest, the pore isothermal "equation of state" fits the following van der Waals form which is obtained from an analytical treatment of planar slit pores and involves an assumption of a flat density profile in the pore (Schoen & Diestler, 1998):

$$P_{pore}\left(\rho_{pore},L\right)=a_0+\frac{\rho_{pore}RT}{1-a_1\rho_{pore}}+a_2\rho_{pore}+a_3\rho_{pore}^2 \qquad \text{... (2.1)}$$

Here, *R* is the universal gas constant and a_0, a_1, a_2 and a_3 are the parameters to be fitted independently for each *L*. The corresponding curves for four values of *L* for ethane solvated pores are shown in Figure 2.2c. An apparent advantage of this approach is that the fit pressure appears to suppress the effect of random errors at individual state points on consequent results.

(b) Widom Insertion Calculations (Widom, 1963) (Frenkel & Smit, 2002) for the excess chemical potential (μ_{pore}^{ex}) as a function ρ_{pore} for different values of *L* using the configurational snapshots generated in the canonical ensemble simulations. These can be fitted to the following form (Schoen & Diestler, 1998):

$$\beta\mu_{pore}^{ex}\left(\rho_{pore},L\right)=a_{\mu0}-\ln\left(1-\rho_{pore}a_{\mu1}\right)+\frac{\rho_{pore}a_{\mu1}}{1-\rho_{pore}a_{\mu1}}+a_{\mu2}\rho_{pore} \qquad \text{... (2.2a)}$$

Here $\beta = (RT)^{-1}$ and *$a_{\mu 0}$, $a_{\mu 1}$, $a_{\mu 2}$* are parameters to be fitted independently for each *L*. The excess chemical potential is related to the activity by the simple relation:

$$\xi_{pore}(\rho_{pore}, L) = \rho_{pore} \exp(\beta \mu_{pore}^{ex}) \qquad \text{... (2.2b)}$$

The corresponding curves for four values of *L* for ethane solvated pores are shown in Figure 2.2a.

(c) Canonical ensemble simulations of pure solvent to get bulk equation of state for CO_2 and ethane. Simulations are run for a fixed number of solvent molecules and different sizes of the simulation cell, which is periodic in all three dimensions, and pressure is calculated in each case. This gives bulk solvent pressure (P_{bulk}) as a function of bulk solvent density (ρ_{bulk}). This data is then fitted to the following two-parameter form (Schoen & Diestler, 1998):

$$P_{bulk} = \frac{RT\rho_{builk}}{1-\rho_{bulk} b} - a_{bulk}\rho_{bulk}^2 \qquad \text{... (2.3a)}$$

$$b = \frac{2}{3}\pi\sigma_f^3 \text{ and } a_{bulk} = \frac{16\pi}{9}\sigma_f^3 \varepsilon_f \qquad \text{... (2.3b)}$$

Where σ_f and ε_f are fluid-specific constants that must be obtained by fitting equation 2.3 to the equation of state. The physical interpretation of the constants is that σ_f is the diameter of the core of the fluid particles while ε_f is their attractive energy parameter. The corresponding plot for ethane solvent appears in Figure 2.2d.

2.3.3.2 Further processing of data

To get $\mathcal{W}$ from the curves fitted to the primary data, we follow a procedure that is depicted in Figure 2.2. To start, we pick a value of activity ξ_{bulk} and for each *L* for which equation 2.2 is fitted we solve:

$$\xi_{pore}(\rho_{pore}, L) = \xi_{bulk} \qquad \text{... (2.4)}$$

This step is depicted graphically in Figure 2.2a as the horizontal line intersecting the activity-curves at the points $\rho_{pore}\left(\xi_{bulk}, L\right)$. We transfer these values over to the plot of 1/L vs. $\rho_{pore}\left(\xi_{bulk}, L\right)$ shown in Figure 2.2b. This we find can be fit to a simple linear form:

$$\rho_{pore}^{fit}\left(\xi_{bulk}, L\right) = \rho_{bulk}\left(\xi_{bulk}\right)\left(1 - \frac{2l_o}{L}\right) \quad \text{… (2.5)}$$

We defer the discussion of the implications of the excellent fit to a linear form over the entire range of gap-widths to Section 2.4. The quantity of immediate interest is ρ_{bulk} which we transfer over to the equation of state shown in Figure 2.2d to get the corresponding P_{bulk} for the given value of ξ_{bulk}. We will explain below why we use this process.

To calculate the potential of mean force, we transfer the values of ρ_{pore}^{fit} over to the plot of $P_{pore}(\rho_{pore}, L)$ vs. ρ_{pore} shown in Figure 2.2c from which we get a series of values of $P_{pore}\left(\xi_{bulk}, L\right)$. These we transfer over to the plot of $P_{pore}\left(\xi_{bulk}, L\right)$ vs. L shown in Figure 2.2f.

The conventional form of the potential of mean force (W_{PMF}) between a pair of nanoparticles is, in light of the discussion in section 2.3.2, as follows:

$$W_{PMF}^{conventional}\left(\xi_{bulk}, L\right) = \int_{\infty}^{L} \left[P_{pore}\left(\xi_{bulk}, L'\right) - P_{bulk}\left(\xi_{bulk}\right)\right] A_{pore}\, dL' \quad \text{… (2.6)}$$

Where $P_{bulk}\left(\xi_{bulk}\right)$ is the bulk solvent pressure corresponding to its given bulk activity and A_{pore} is the cross sectional area of a single periodic simulation cell. However, due to a subtlety which arises from use of a slit-pore geometry which is periodic in only two dimensions, this equation cannot be used as it is. The fact is that there is no simple way of incorporating long-range corrections to the van der Waals interactions in a structured slit-pore geometry and the standard molecular-dynamics packages do not do so. By “long-range” we mean van der Waals interactions between molecules separated by a distance greater than the van der Waals cut-off distance used in the simulation. Since we are seeking only a first-order understanding of the problem of particle disperison, we did not incorporate these corrections. Consequently, the calculated thermodynamic properties of the solvent in the slit-pore reflect the fact that the long-range van der Waals interactions are truncated. The complication arises from the fact that the molecular models of the solvents are designed in such a way that the thermodynamic properties calculated using these models fit empirical data only after long-range interactions are accounted for. Hence the solvent in the slit pore, where these interactions are truncated, corresponds imperfectly to the solvent represented by the molecular model. Specifically, the true value of P_{bulk} used in equation 2.6 is smaller than the value to which $P_{pore}\left(\xi_{bulk}, L\right)$ levels off at large *L.* Consequently, we need to replace P_{bulk} in equation 2.6 with an *effective* bulk value which represents the limiting slit-pore pressure at large gap with potential truncation. Hence we choose the value to which the P_{pore} *vs. L* curve levels off i.e.

$$P_{bulk}^{eff}\left(\xi_{bulk}\right) = \text{average}\left\{P_{pore}\left(\xi_{bulk}, L\right) : L \geq L_{trunc}\right\} \qquad \text{… (2.7)}$$

Where L_{trunc} is the gap-width where the P_{pore} *vs. L* curve levels off. We can now re-write the expression for potential of mean force as:

$$W_{PMF}\left(\xi_{bulk}, L\right) = \int_{L_{trunc}}^{L} \left[P_{pore}\left(\xi_{bulk}, L'\right) - P_{bulk}^{eff}\left(\xi_{bulk}\right)\right] A_{pore} dL' \qquad \text{… (2.8)}$$

and it is this value that appears in Figure 2.2e. The value of *L* where W_{PMF} is minimum is the equilibrium separation L_{eq} and the corresponding value is the free-energy of flocculation i.e.

$$\mathcal{U}(P_{bulk}) = W_{PMF}(\xi_{bulk}, L_{eq}) \qquad \text{… (2.9)}$$

We note that the long-range interactions are also truncated in the calculation of the excess chemical potential. That is why we cannot get an acceptable P_{bulk} directly from ξ_{bulk} and the equation of state and must instead go through the indirect process described above. However, the *structure* of the solvent, whose calculation does not involve corrections due to long-range interactions, remains the same with or without the long-range corrections. Hence even if long-range interactions were included in the calculation of ξ_{pore}, the relation between ρ_{bulk} obtained from equation 2.5 and the various ρ_{pore} would be substantially maintained and only the corresponding value of ξ_{bulk} would change. Even so, we cannot maintain that the solvent being simulated in the pores is the same as the solvent represented by its molecular model. It is however a very closely-related solvent and one whose W_{PMF} closely tracks that of the accurate one at the same density. The P_{bulk} obtained by the above procedure is used to establish points of comparison of simulation results with experimental observations.

2.3.4 Simulation Setup, Molecular Models and Computational Details

Each simulation-setup consists of 536 silver atoms (approximated by LJ particles) arranged in an FCC lattice to form two plates, each three atomic layers thick. The dimensions of the periodic system along the *x*- and *y*- directions i.e, along the face of the plates are 28.8Å by 29.92Å respectively (see Figure 2.1d). The system is periodic in these directions but not in the *z*-direction. The z-direction separation between the nearest silver atoms of the opposing plates is taken as the gap-width *L* (see Figure 2.1c). The plates are passivated by n-dodecanethiol ($C_{12}H_{25}SH$) ligands. We vary the number and type of solvent molecules (CO_2 and ethane) and the gap-width *L*. The ligand roots are distributed as shown in Figure 2.1d and the ligand surface-packing density is 16Å^2/ligand which is consistent with experimental observations (Korgel, Fullam, Connolly, & Fitzmaurice, 1998) (Shah, Husain, Johnston, & Korgel, 2002).

The total energy of the system is a sum of intra- and inter-molecular contributions. The intra-molecular interactions for the surfactants are represented as a sum of three terms as

$$E_{\text{intra}} = \sum E_{\text{stretch}} + \sum E_{\text{bend}} + \sum E_{\text{dihedral}} \,. \qquad \text{… (2.10)}$$

The bond stretching term is given by

$$E_{\text{stretch}} = \sum_i H_i^b \left(b_i - b_{oi}\right)^2, \qquad \text{... (2.11)}$$

where H_i^b is the bond stretching force constant, b_{oi} the equilibrium bond distance and b_i the instantaneous bond length of the i^{th} bond. The bond angle bending term is given by

$$E_{\text{bend}} = \sum_i H_i^\theta \left(\theta_i - \theta_{oi}\right)^2, \qquad \text{... (2.12)}$$

where H_i^θ is the bending force constant, θ_{oi} the equilibrium bond angle and θ_i the instantaneous i^{th} bond angle. The dihedral (or torsional) contributions to the intramolecular potential are represented by

$$E_{\text{dihedral}} = \sum_i \frac{1}{2} \sum_{n=1}^{3} k_{n,i} \left(1 + (-1)^{n+1} \cos(n\phi_i)\right), \qquad \text{... (2.13)}$$

where $k_{n,i}$ are the torsion parameters and ϕ_i is the i^{th} dihedral angle.

The intermolecular interactions between non-bonded pairs are given by a sum of dispersion (12-6 LJ) and electrostatic terms. The resulting equation for intermolecular interactions is

$$E_{\text{inter}} = \sum_i \sum_{j>i} \left\{ 4\varepsilon_{ij} \left[\left(\frac{\sigma_{ij}}{r_{ij}}\right)^{12} - \left(\frac{\sigma_{ij}}{r_{ij}}\right)^{6} \right] + \frac{1}{4\pi\varepsilon_o} \frac{q_i q_j}{r_{ij}} \right\}. \qquad \text{... (2.14)}$$

Here q_i, q_j are the charges centered on the atoms of the different molecules and r_{ij} is the distance between the sites *i* and *j*. The LJ parameters (σ_{ij}, ε_{ij}) for interaction between dissimilar atoms are calculated using the standard Lorenz-Berthelot combining and mixing rules given by

$$\varepsilon_{ij} = \sqrt{\varepsilon_i \varepsilon_j} \text{ and } \sigma_{ij} = 0.5\left(\sigma_i + \sigma_j\right). \qquad \text{... (2.10)}$$

All simulations are run at a temperature of 308K at which temperature the experiments with nanoparticle size selective fractionation using ethane were done (Shah, Holmes, Johnston, & Korgel, 2002). The simulations are implemented using a modified version of the DL_POLY 2.15 package (Smith

& Forester, 2003) and the results visualized by VMD (Humphrey, Dalke, & Schulten, 1996). The default force field used is OPLS-AA (Jorgensen, 2002) except for carbon-dioxide which is modeled using the EPM2 model (Harris & Yung, 1995), ethane which is modeled using the TraPPE united-atom model (Martin & Siepmann, 1998) and Ag whose LJ parameters (σ_{Ag}=2.708Å, ε_{Ag}=0.2668kcal/mol) are set to approximate long range attractive interaction between Xe (Berry, Rice, & Ross, 2000) and Ag(111) calculated ab-initio (Vidali, Ihm, Kim, & Cole, 1991) (Gatica, Li, Trasca, Cole, & Diehl, 2008). These molecular models are essentially the same as those used to investigate surfactant behavior at water-CO_2 interfaces (da Rocha, Johnston, & Rossky, 2002) (Stone, da Rocha, Rossky, & Johnston, 2003).

To run the canonical ensemble calculations to get P_{pore}, the silver (Ag) particles and the sulfur (S) atoms are fixed rigidly in position. Each simulation is run at a temperature of 308K enforced by a Nose Hoover thermostat with a time constant of 100-fs. The simulation timestep is 1-fs. For each simulation, an equilibration run of 50ps is followed by a production run of ~100ps which is sufficient time to get a reliable value of the pressure as verified by convergence tests (Flyvbjerg & Petersen, 1989). An ortho-rhombic periodic cell is employed with lengths of 28.8Å, 29.92Å and 400.0Å in the x-, y- and z- directions respectively. The z-direction's dimensions are chosen as more than 5 times the maximum gap-width employed to ensure that even upon including periodicity in the z direction these images of the system are "invisible" to each other. This way we can employ three-dimensional Ewald summation for the electrostatics, while retaining the correct physics of the problem (Frenkel & Smit, 2002). Configurations are written out every 100 timesteps for use in Widom insertion calculations (Widom, 1963) to evaluate activity. The force on a single plate is calculated as the sum of all z-direction forces on the frozen particles (Ag and S) composing the plate. This satisfies the mechanical definition of pressure as force per unit area on the confining wall of a fluid. However, this also means that there are no long range corrections applied to the force. Hence a cutoff radius of 14.3Å (maximum possible) is applied in the x and y directions while 30Å is applied in the z direction. This enables most, but not all, of the contributions to the normal forces to be accounted for.

For each slit-pore simulation run a series of configurations is generated. The excess chemical potential is calculated using the Widom Insertion method (Widom, 1963) (Frenkel & Smit, 2002). For a given configuration of N solvent molecules, the configurational energy U_N is calculated. Then a molecule with random position coordinates is added to the configuration list. Multiple insertions of one particle are then achieved simply by changing, at random, the position of this molecule and noting the resulting configurational energy U_{N+1}. Note that the inserted molecule is always within the gap between the plates. In this simulation 10,000 such insertions are executed for each configuration. For the x-y direction, the potential cutoff is 14.3Å and for the z direction cutoff is 30Å. Ewald summation is used but there is no long range correction applied to the van der Waals contribution to the potential energy. This implies that the calculated chemical potential is *higher* than what it would be if the long range correction were applied, but it is consistent with the way the pressure is calculated.

To get equation of state for the bulk solvent, 266 solvent molecules are placed in square periodic cells of different side lengths and the simulations are run in the canonical ensemble at T=308K enforced by a Nose-Hoover thermostat with 0.1ps time constant. The simulation timestep is 1-fs. Van der Waals interactions are cut-off after 10Å, 3-D Ewald summations are employed for electrostatics, each simulation is equilibrated for 50ps and followed by a production run of 200ps at the end of which average isotropic pressure is determined. Long range corrections *are* applied when calculating pressure for the bulk solvent equation of state.

We have chosen four values of P_{bulk} viz. 150 atm, 200 atm, 250 atm and 300 atm, which are in the range of experimental interest, to calculate W_{PMF} and $\mathcal{W}$.

2.4 Results and Discussion

The first aspect of the results to be noted is the linearity of the ρ_{pore} *vs.* $1/L$ plots for both CO_2 (Figure 2.3) and ethane (Figure 2.4) solvated pores. Using methods described in section 2.3, P_{pore} *vs.* L curves corresponding to different values of P_{bulk} are calculated for CO_2 (Figure 2.5) and ethane (Figure 2.6). Using these and equation 2.8 we obtain W_{PMF} *vs.* L curves for CO_2 (Figure 2.7) and ethane (Figure 2.8). Density profiles in a large gap (L=100Å) slit pore for both solvent and ligand appear in Figure 2.9 (CO_2) and Figure 2.10 (ethane). Using $L_{eq}=43Å$ for CO_2 and $L_{eq}=47Å$ for ethane, $\mathcal{W}$ *vs.* P_{bulk} (see equation 2.9) plots for both CO_2 and ethane appear in Figure 2.11. In the absence of solvent, equilibrium occurs at $L_{eq\text{-}vac}=43Å$, for $L<L_{eq\text{-}vac}$, the overlap of ligand regions causes huge repulsive interactions. Also, upon fitting the equations of state to an equation of the form of equation 2.3 we get the van der Waals parameters for bulk ethane ($\varepsilon_f = 0.809\text{kcal/mol}, \sigma_f = 3.43\mathring{A}$) and bulk CO_2 ($\varepsilon_f = 0.807\text{kcal/mol}, \sigma_f = 2.9\mathring{A}$).

We will first discuss the consistency of our results with experimental observations. Next we will comment on the applicability of models developed for polymer brushes in describing systems of densely packed short chain ligands. Then we will examine the implications of the linearity of the ρ_{pore} *vs.* $1/L$ which allow us to make simplifying assumptions in order to develop a simple interpretive model to describe the behavior of the two systems. Using this model we will determine the molecular level causes of the difference in performance of the hydrocarbon ligand in the two solvents. Finally we will propose strategies to improve the performance of ligands in CO_2.

2.4.1 Consistency with experimental observations

It is clear from an examination of the $\mathcal{W}$ *vs.* P_{bulk} curves in Figure 2.11 that our metric for effectiveness i.e. $\mathcal{W}$ is significantly more positive when ethane is the solvent than when CO_2 is the solvent. Clearly ethane is the better solvent for n-dodecanethiol passivated molecules. This is consistent with experimental observations (Shah, Holmes, Johnston, & Korgel, 2002) (Shah, Holmes, Doty, Johnston, &

Korgel, 2000). While conducting experiments with ethane as the solvent (Shah, Holmes, Johnston, & Korgel, 2002) it was shown that at 308 K (same as our temperature), n-dodecanethiol passivated silver nanoparticles with diameter greater than 60Å flocculated at pressures less than 312 atm which agrees well with the figure of 272 atm for flocculation of 60Å diameter particles that we obtain from our simulations if we choose as the stability criterion at the reasonable value of $\mathcal{W} = -1.5k_BT$ (Shah, Holmes, Johnston, & Korgel, 2002).

2.4.2 Solvent does not "solvate" ligands

In a number of instances (Meredith, Sanchez, Johnston, & de Pablo, 1998) (Fernandez-Nieves, Fernandez-Barbero, Vincent, & de las Nieves, 2001) (Shah, Holmes, Johnston, & Korgel, 2002) (Patel & Egorov, 2007), the greater effectiveness of ligands is attributed to more repulsive "steric" interaction as ligands from the two nanoparticle surfaces interdigitate/overlap. The repulsive steric interaction can be both osmotic (due to the resistance to rejection of solvent from among the ligands) and elastic (due to the resistance of the ligands to confinement). Interpreted in a general way, these models imply that better solvation of the ligands by solvent leads to a more repulsive $\mathcal{W}$.

However, as is clear from the ligand and solvent density profiles (Figure 2.9 for CO_2 and Figure 2.10 for ethane), the ligand regions are not penetrated by the solvent. The model of passivated-particles used for polymer brushes (Meredith, Sanchez, Johnston, & de Pablo, 1998) (Fernandez-Nieves, Fernandez-Barbero, Vincent, & de las Nieves, 2001) or sparsely packed ligands (Patel & Egorov, 2007) evidently does not hold for the present case of dense passivation by short-chain ligands. The passivated surface in this case is much harder and smoother than it would be in case of a polymer brush; the solvent only interacts with the ligand *tips.* Furthermore, the repulsion evident for the more effective system (i.e. with ethane as solvent) can be seen from Figure 2.8 and Figure 2.10 to be clearly set up before the ligands from opposite faces touch each other. Interdigitation of ligands does not play a role in stabilization in this case. Also, since the ligand region is densely packed, the ligand configurations don't vary under influence of solvent or interaction with the opposite surface; ligand entropy is not a significant component in stabilization, either.

2.4.3 Linearity of ρ_{pore} *vs.* $1/L$ plots

The fact that equation 2.5 describes the ρ_{pore} *vs.*$1/L$ plots rather well implies that the density profile in the slit pore can be approximated by a step function whose value is ρ_{bulk} at $z>l_o$ and $z<L-l_o$ and zero elsewhere. Hence l_o is a measure of the thickness of the passivating layer. This is consistent with the relatively narrow and low peaks in the density profile for large gap-widths seen in Figure 2.9 and Figure 2.10. This is also consistent with the fact that the equations 2.1 and 2.2 derived from an assumption of step-function density profile fit their corresponding data rather well. Further, the lack of noticeable upward deviation from linearity of ρ_{pore} as L decreases implies that the solvent structure in our chosen pressure range is determined primarily by short range interactions and that the interaction with the walls of the pore merely affects the osmotic resistance of the solvent to leave the pore.

2.4.4 Interpretation of $\mathcal{W}$

Since the solvent density profile is fairly uniform across the pore and can be adequately approximated by a step function, it makes sense to try to develop a simple model by which to better understand the contributions to $\mathcal{W}$ for the two systems. We consider $\mathcal{W}$ to be composed of 3 types of contributions: W_{vac} (due to direct interaction between ligands on opposite faces), W_{self} (contribution due to solvent cohesive interaction with its own bulk) and W_{wall} (contribution due to solvent interaction with the walls). Of these, we already know W_{vac} from our simulations in vacuum. W_{wall} is the difference in wall-fluid interaction free energy when the gap-width is very large and when the gap-width is some finite value of L and we need a route to estimate it. If $u_{fw}(z')$ is the interaction free energy of a single solvent molecule at a distance z' from a ligand-passivated wall, then:

$$W_{wall}(L) = A_{pore}\rho_{bulk}\int_{l_o}^{L-l_l}\left[u_{fw}(z') + u_{fw}(L-z')\right]dz' - 2A_{pore}\rho_{bulk}\int_{l_o}^{\infty}u_{fw}(z')dz' \qquad \text{... (2.11)}$$

In equation 2.11, we have used the approximation justified in section 2.4.2 of the density profile as a step function with value of ρ_{bulk} between l_o and L-l_o and zero elsewhere. We have also assumed a planar pore to facilitate analysis. The first term of the right hand side is the total free energy of interaction of solvent in a slit of gap-width L and the second term is the same value when the walls are infinitely separated.

In order to use equation 2.11 to calculate W_{wall}, we need to obtain u_{fw}. For this we use the density profiles (Figure 2.9, Figure 2.10) and a simple density-functional approach. In doing this we will have used the non-uniformity in the density-profile to obtain u_{fw} but will have assumed a flat density profile when calculating W_{wall}. This is only justified because the accuracy with which we calculate W_{wall} is much lower than the accuracy with which we can calculate the density profiles, but the result is sufficient for our purposes.

Let,

$$U_{fw}(z) = u_{fw}\left(\frac{L}{2} - |z|\right) + u_{fw}\left(\frac{L}{2} + |z|\right) \qquad \text{… (2.12)}$$

Here $\frac{L}{2} - |z|$ is perpendicular distance from one wall and $\frac{L}{2} + |z|$ is perpendicular distance from another when z is the z-coordinate of position within the pore as defined in Figure 2.1c.

Since each point in the slit pore is at equilibrium with the bulk, the chemical potentials (μ) are the same. Taking a density-functional theory approach (Evans, Marconi, & Tarazona, 1986) with the weighted density approximation (Tarazona, Marconi, & Evans, 1987) we can write:

$$\mu = U_{fw}(z) + \mu_{id}\left(\rho_p(z)\right) + \mu_{ref}^{ex}\left(\overline{\rho}_p(z)\right) + \mu_{MF}(z) \qquad \text{… (2.13)}$$

Here, $\rho_p(z)$ is the solvent density at a particular point in the pore (see Figure 2.9 and Figure 2.10), U_{fw} is the contribution to the chemical potential due to interaction of solvent molecule with the walls and μ_{id} is the ideal gas component of the chemical potential. μ_{ref}^{ex} is the excess chemical potential of the reference system calculated at the weighted-average density $\overline{\rho}_p(z)$. The reference system in our case is the hard-sphere fluid with the van der Waals approximation applied to the pair-distribution function (Schoen & Diestler, 1998). Finally, μ_{MF} is the contribution to the chemical potential due to the non-hard-core interactions with other solvent molecules in the mean-field approximation. The various quantities have the following expressions:

$$\mu_{id}(\rho) = RT\ln\left(\Lambda^3\rho\right) \qquad \text{… (2.14)}$$

where Λ is the thermal deBroglie wavelength. From the analysis on a van der Waals type fluid (Schoen & Diestler, 1998):

$$\mu_{ref}^{ex}\left(\overline{\rho}_p(z)\right) = -RT\ln\left(1-\overline{\rho}_p(z)b\right) + RT\left(\frac{\overline{\rho}_p(z)b}{1-\overline{\rho}_p(z)b}\right) \qquad \text{… (2.15)}$$

The overbar on $\overline{\rho}_p$ indicates that it is a weighted density and the weight we use is simply the volume fraction of the solvent particle in a given thin slab of the pore region i.e.

$$\overline{\rho}_p(z) = \int_{-L/2}^{L/2} \rho_p(z)w(z-z')dz \qquad \text{… (2.16a)}$$

Where,

$$w(z) = \begin{cases} 3\left(\sigma_f^2 - z^2\right)/4\pi\sigma_f^3 & \forall z \le \sigma_f \\ 0 & \forall z > \sigma_f \end{cases} \qquad \text{… (2.16b)}$$

And the mean-field component is simply given by:

$$\mu_{MF}(z)=\int_{-L/2}^{L/2}\rho_p(z')dz'\int_{\sigma_f}^{\infty}dr_{xy}\,2\pi r_{xy}u_{ff}(r) \quad \text{... (2.17)}$$

and

$$r=\sqrt{\left[r_{xy}^2+(z-z')^2\right]},\quad u_{ff}(r)=4\varepsilon_f\left(\frac{\sigma_f^{12}}{r^{12}}-\frac{\sigma_f^6}{r^6}\right) \quad \text{... (2.18)}$$

Where ε_f and σ_f are obtained from the equation of state via a fit to equation 2.3.

Since the pore is at equilibrium with the bulk we have:

$$\mu=\mu_{id}(\rho_{bulk})+\mu_{bulk}^{ex} \quad \text{... (2.19)}$$

From the van der Waals equation of state (Schoen & Diestler, 1998):

$$\mu_{bulk}^{ex}=-RT\ln(1-\rho_{bulk}b)+RT\left(\frac{\rho_{bulk}b}{1-\rho_{bulk}b}\right)-2a_{bulk}\rho_{bulk} \quad \text{... (2.20)}$$

Where a_{bulk} and b are the same as in equation 2.3b. Hence equation μ from equations 2.13 and 2.19 and using equation 2.14 we get:

$$U_{fw}(z)=RT\ln\left(\frac{\rho_{bulk}}{\rho_p(z)}\right)+\mu_{bulk}^{ex}-\mu_{ref}^{ex}(\overline{\rho}_p(z))-\mu_{MF}(z) \quad \text{... (2.21)}$$

Since we are using density profile in a slit-pore with widely separated walls (*L=100Å*) and since $u_{fw}(z')\rightarrow 0$ at large values of *z'*, we can write:

$$U_{fw}(z)=u_{fw}\left(\frac{L}{2}-|z|\right) \quad \text{... (2.22)}$$

The plots of u_{fw} obtained from this procedure are smoothed by fitting to the following form:

$$u_{fw}(z') = \left(1 - \tanh\left(\frac{z'-z_o}{\alpha}\right)\right)\left[u_o\left(1 - e^{-u_1(z'-z_1)}\right)^2 + u_2(z'-z_1)^2\right] + \left(1 + \tanh\left(\frac{z'-z_o}{\alpha}\right)\right)\left[\left(\frac{u_3}{z'^9} - \frac{u_4}{z'^3}\right)e^{-u_5 z'}\right]$$

… (2.23)

where z_o, z_1, α, u_1, u_2, u_3, u_4 and u_5 are constants to be fitted to the $u_{fw}(z')$ points generated using equations 2.21 and 2.22 and the wide-gap density profile. Figure 2.12 shows the plots of $u_{fw}(z')$ for CO_2 and ethane. This we can use in equation 2.11 to get W_{wall}. When substituting in equation 2.11 to get W_{wall}, we find that it is preferable to use value of l_o as that distance at which u_{fw} in Figure 2.12 first crosses zero rather than using the value obtained from a fit of equation 2.5 to Figure 2.3 or Figure 2.4 (for CO_2 or ethane, respectively), since the latter yields a value of W_{wall} that is more sensitive to errors in the density profiles. W_{self} is obtained simply by $W_{self}= W_{PMF}-W_{wall}$.

2.4.5 Reasons for Effectiveness of Ethane over CO_2

Since we want to establish the contributions to the *difference* in the effectiveness of the ligands in the two solvents, for $P_{bulk}=300atm$, we plot the difference in W_{PMF}, W_{wall} and W_{self} between CO_2 solvated pore and e*thane* solvated pore (ethane value subtracted from CO_2 value) for various values of L. We call the terms ΔW_{PMF}, ΔW_{wall} and ΔW_{self}, respectively. This plot appears in Figure 2.13. It must be noted that ΔW_{wall} is *positive* for the wider gap-widths and only becomes negative near $L_{eq\text{-vac}}$. This is due to the longer range of the wall-solvent interaction potential in case of CO_2 coupled with a higher molar density of CO_2 compared to ethane at the same pressure. This offsets the fact, evident from Figure 2.12, that CO_2 has a lower *specific molar* affinity for the ligands. However, in spite of a more repulsive osmotic interaction (W_{wall}), it is clear from Figure 2.13 that CO_2 is a poorer solvent than ethane. The ΔW_{self} line in Figure 2.13 is consistently negative and closely tracks the ΔW_{PMF} line i.e. CO_2 interacts more strongly with its own bulk than ethane does, and, further, that the bulk of the added interactions are due to the quadrupoles. This is also consistent with the following observations:

1. Using a standard database (http://webbook.nist.gov/chemistry/fluid/) we can calculate (Allada, 1984) the Hildebrand solubility parameters (δ) for supercritical ethane and CO_2 at 308K and 300atm which yield δ_{ethane}=12.0 $(J/cm^3)^{0.5}$ and δ_{CO2}=14.6 $(J/cm^3)^{0.5}$ i.e. CO_2 has the higher cohesive energy density. This is also consistent with the fact that melting point of CO_2 is 216.5K against ethane's 90.35K and that the critical pressure is 72.79 atm at a critical temperature of 304.16K vs. ethane's 48.09 atm at 305.33K.
2. Quadrupolar interactions contribute as much as 20% of the solvent-solvent interactions of CO_2 (Myers & Prausnitz, 1965) so that the incentive for CO_2 to occupy the confined-region between the ligand-passivated surfaces, where it must forgo the enthalpic benefit of these interactions, is lower. Ethane molecules on the other hand interact almost exclusively via dispersion interactions which the passivating ligands can sufficiently provide. Hence, measures of affinity such as the Flory-Huggins interaction parameter will *misleadingly* show CO_2 to be a better solvent than ethane for dodecane ligands ($\delta_{dodecane}$=16.3 $(J/cm^3)^{0.5}$) (O'Neill, et al., 1998) (Shah, 2003).
3. It is noted that for polymers dissolved in supercritical CO_2, solvation is governed by polymer-polymer interaction rather than polymer solvent interaction (O'Neill, et al., 1998) and that CO_2 is an excellent anti-solvent for dodecanethiol passivated nanoparticles (Gupta, Shah, Zhang, Saunders, Korgen, & Johnston, 2005) (Anand, et al., 2008) as well as organic-polymeric nanoparticles (Chang, Lee, & Lin, 2007)(Dixon, Johnston, & Bodmeier, 2004).

2.4.6 Deceptiveness of Bulk Fluid Properties and Design of Experiments

The most popular experiment to select for possible ligands is probably the cloud-point determination where the prospective ligand is dissolved at a high pressure in the supercritical solvent and pressure is gradually reduced until flocculation starts. The pressure where flocculation begins is the cloud point and the lower it is, the more effective the ligand might be expected to be (Anand, Bell, Fan, Enick, & Roberts,

2006) (Shah, Husain, Johnston, & Korgel, 2002) (Potluri, Xu, Enick, Beckman, & Hamiltion, 2002) (Sarbu, Styranec, & Beckman, 2000). As seen from our simulations, however the configurations of the ligands in the passivating layer are very different from ligands in bulk fluid. Most importantly, the ligands in the passivation layer have a rigid orientation and only their *tips* are accessible to the solvent – whereas the bulk ligands have their lateral surfaces exposed as well. Hence it is possible that a selection criterion based on bulk behavior would lead to rejection of good candidates and/or acceptance of bad candidates. Experiments must be designed to reflect the heterogenous character of the passivated nanoparticle surfaces. The use of atomic-force microscopy, as suggested recently by a research group (Wu & da Rocha, 2008), promises to yield more reliable criteria.

2.4.7 Design of Ligands

We have gained some insight into how ligand-passivated nanoparticle emulsions are stabilized. Since CO_2 is especially fond of its bulk, a more CO_2-philic ligand would definitely improve performance by increasing the enthalpic benefit of leaving the bulk for the confinement – something that is achieved with the perfluoroalkanes (Shah, Husain, Johnston, & Korgel, 2002) (Shah, Holmes, Doty, Johnston, & Korgel, 2000). A ligand that is less auto-philic would also improve performance. These two attributes of the ligands often work counter to each other – CO_2-philicity is bought at the expense of greater autophilicity. We will explore the implications of this in subsequent papers.

2.5 Conclusion

We have developed a simulation protocol that yields molecular level insight into the physical phenomena related to the effectiveness of capping ligands in stabilizing nanoparticle dispersions. We have used this method first to study a n-dodecanethiol ligand passivated system solvated by CO_2 and ethane and the results are consistent with empirical observation. We conclude that the effectiveness of ethane is due to a lower preference for its bulk over confinement compared to CO_2. Hence, ligands that interact with CO_2 more strongly should be more effective in stabilizing nanoparticle dispersions in supercritical CO_2. We have also suggested that experiments intended to find effective ligands should seek to probe ligand-behaviour *not* in an isotropic bulk system but in heterogenous conditions similar to the ligand-solvent interface of passivated nanoparticles. In the next paper we will examine the moderately effective perfluorocarbon ligands to determine the reason for their effectiveness and to test consistency with our present interpretations.

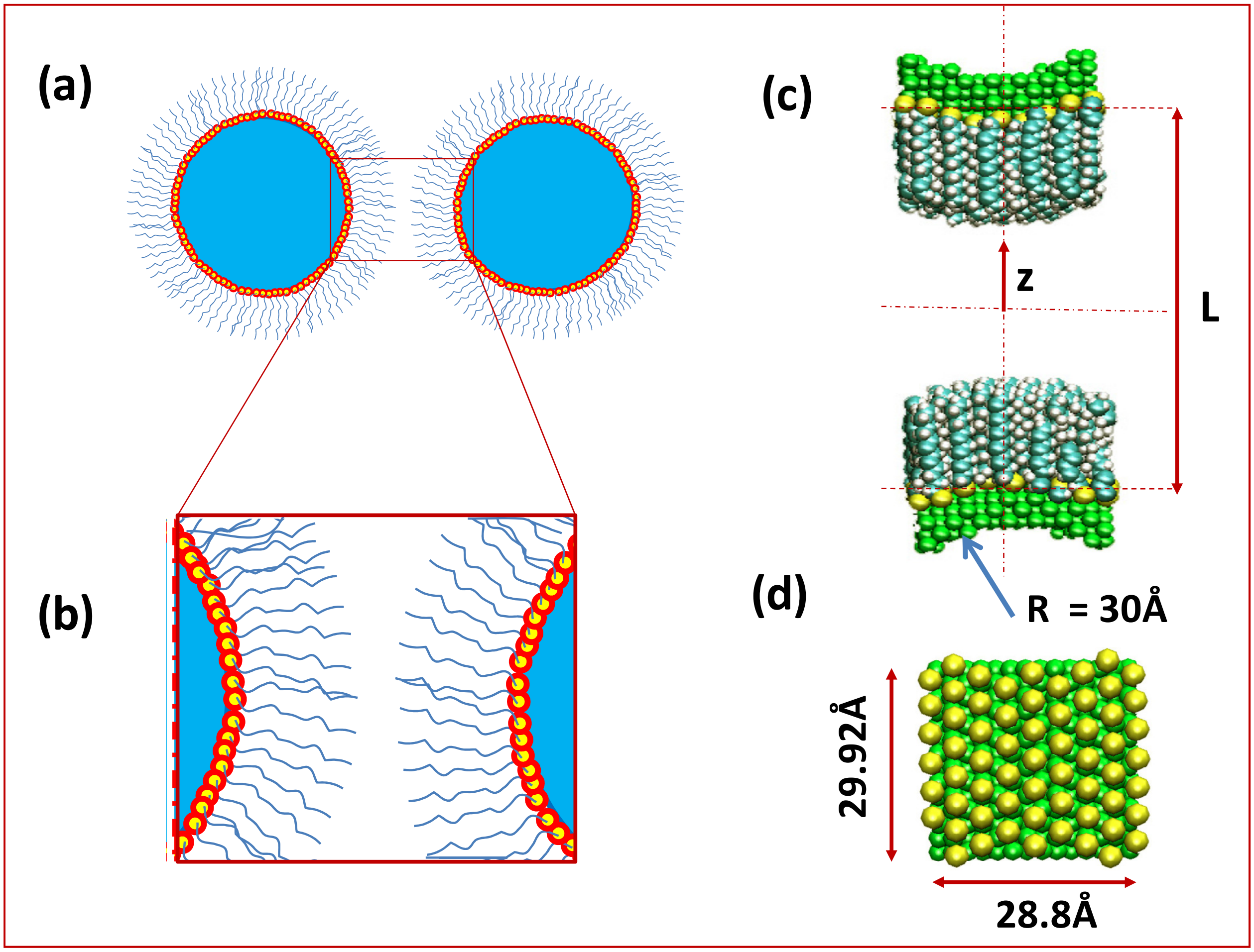

Figure 2.1: The simulation setup. (a) Schematic of a pair of ligand passivated nanoparticles. To simulate a pair of sufficiently diluted nanoparticles of diameter ~60Å, which is an experimentally interesting particle size, we would require a particle number of the order of 100,000. However, (b) comparable insight may be obtained at much lower computational cost (<10,000 particles per periodic box) by examination of a slit-pore with bumpy walls, a periodic image of which is shown schematically. Each "wall" of the slit-pore can be interpreted as the "cheek" of one of the nanoparticles (c) The same system set-up for MD simulations is visualized using VMD (Humphrey, Dalke, & Schulten, 1996). The ligands are dodecanethiol ($C_{12}H_{25}SH$) with the terminal-S group shown in yellow. (d) The distribution of roots (shown by yellow S atoms) on a plate is shown. See text for more details.

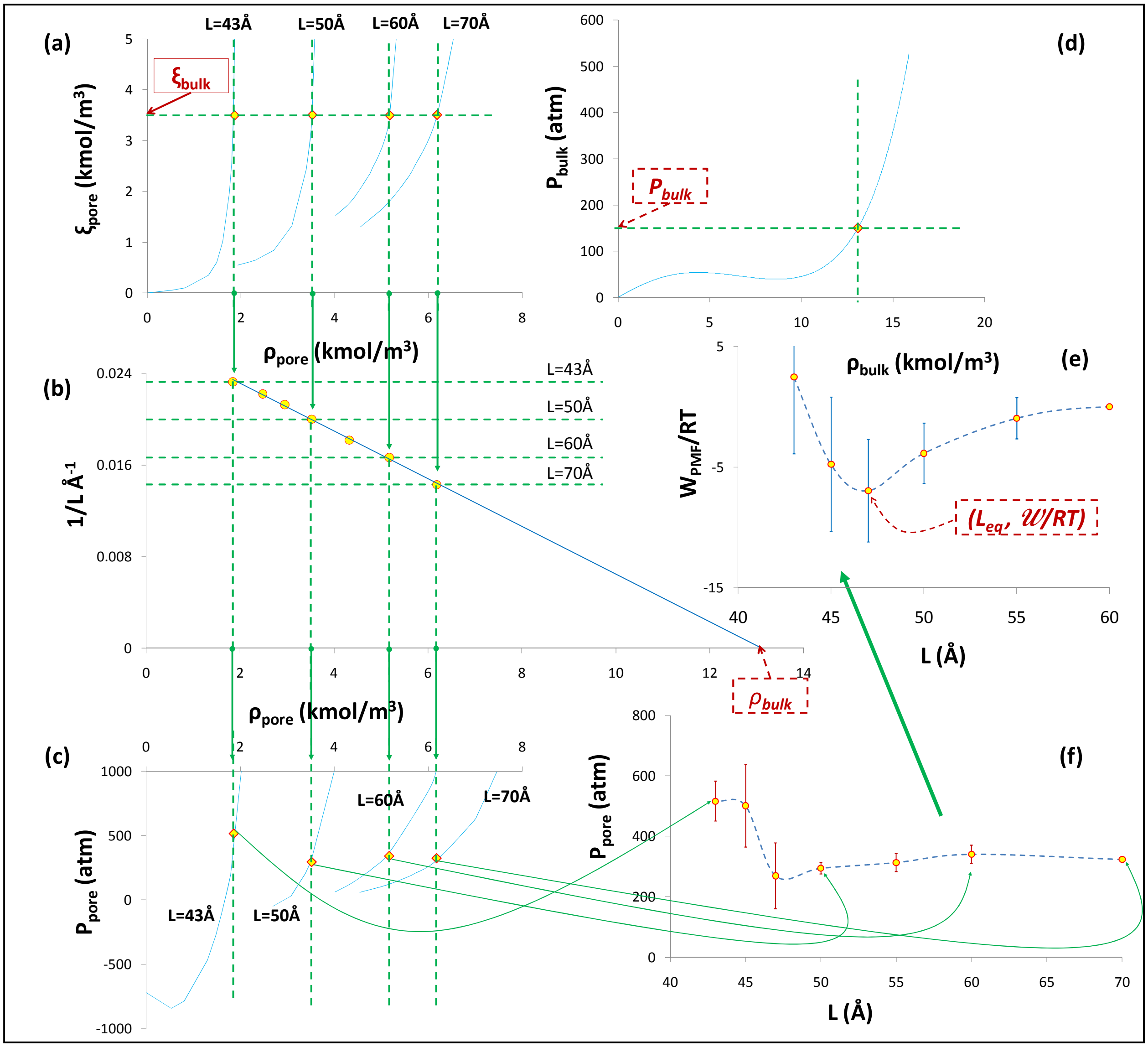

Figure 2.2: Illustration of the post-processing of simulation data. This multi-panelled figure is in support of the text in **Section 2.3.3**. The straight broken lines (▬ ▬ ▬) denote projections onto the axes they intersect. The arrows (➡) denote transfer of information across panels. Externally imposed quantities are framed in a solid-sided rectangle (ξ_{bulk}) while derived quantities are framed in a broken-sided rectange (P_{bulk}). The above illustrations are for ethane as solvent. The panels are as follows: (a) Solvent activity in pore vs. pore solvent density for different gap-widths (L). (b) Inverse gap-width vs. pore solvent density. The points fall on a straight line. (c) Normal pressure on walls of the pore vs. pore solvent density (d) Isothermal equation of state of bulk solvent using molecular model of solvent. (e) Potential of mean force curve at fixed pore-solvent activity corresponding to P_{bulk} for various gap-widths (f) Normal pressure in slit-pore at fixed pore-solvent activity and various gap-widths.

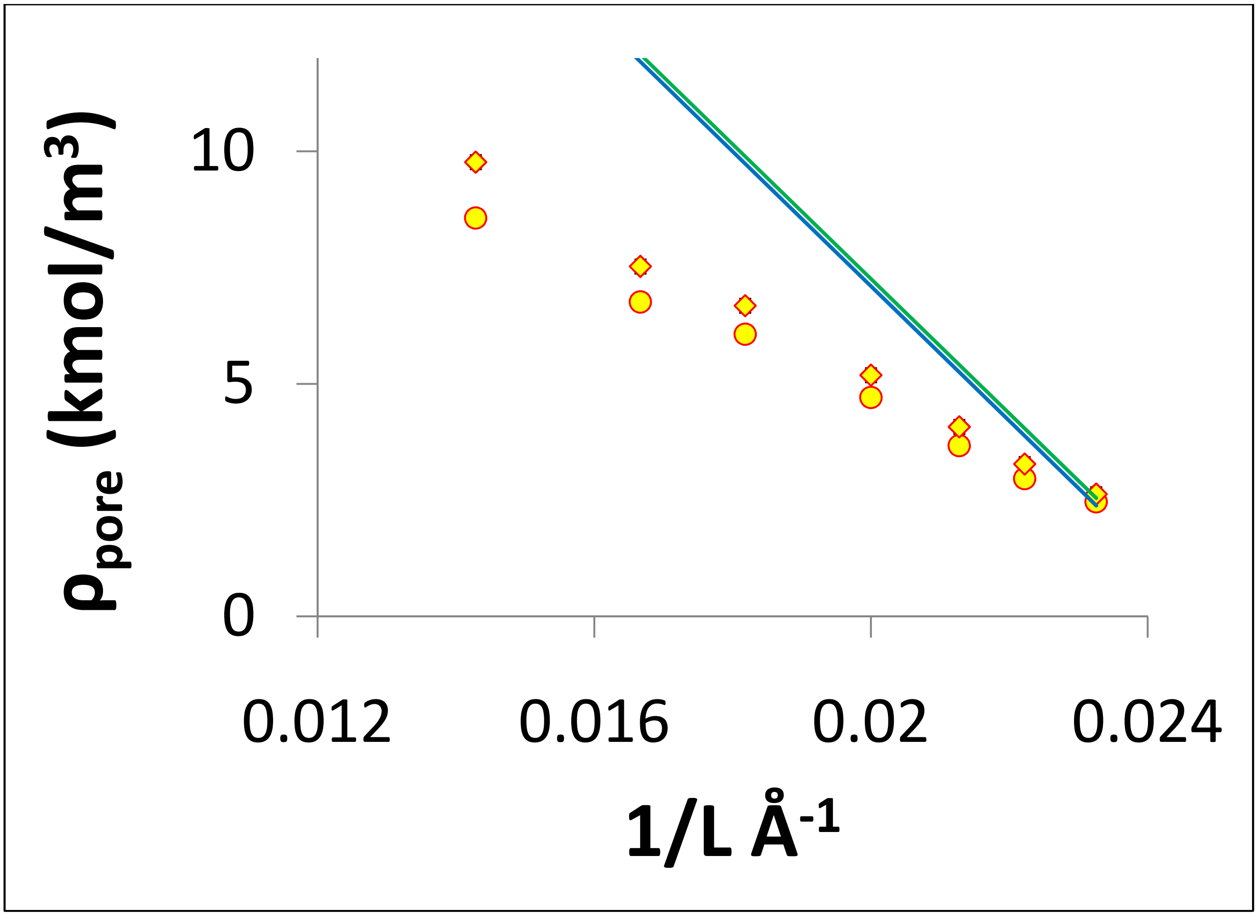

Figure 2.3: Plot of ρ_{pore} vs. 1/L for dodecanethiol passivated slit pore with CO_2 as solvent. The symbols are the result of solutions of equation 2.4 while the solid lines are the straight line fits through them (see equation 2.5). Two bulk pressures are represented with P_{bulk}=*150 atm (* ○ *)* and P_{bulk}=*300 atm (*◇*).* The error bars for the fit are about the size of the symbols.

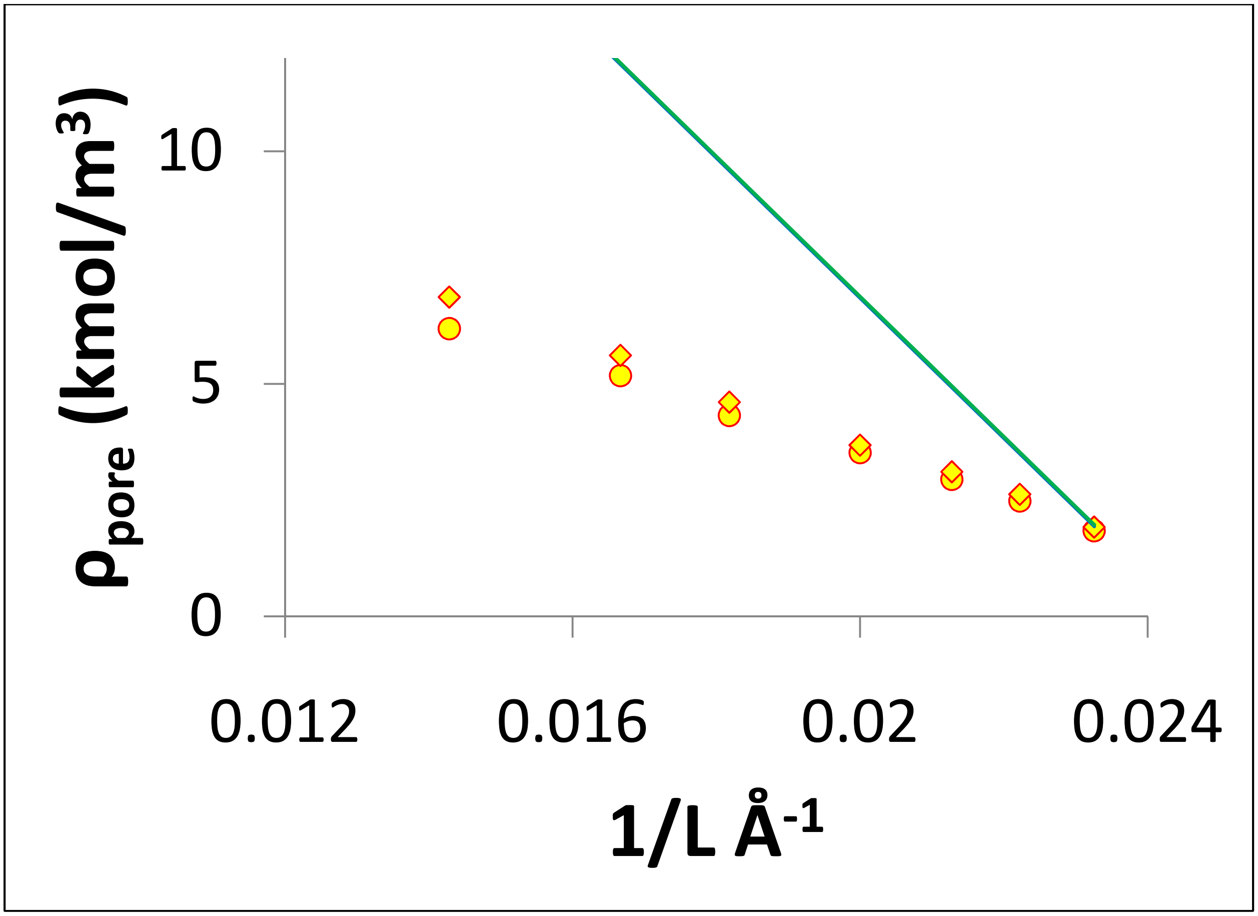

Figure 2.4: Plot of ρ_{pore} vs. 1/L for dodecanethiol passivated slit pore with ethane as solvent. The symbols are the result of solutions of equation 2.4 while the solid lines are the straight line fits through them (see equation 2.5). Two bulk pressures are represented with P_{bulk}*=150 atm (* ● *)* and P_{bulk}*=300 atm (*◆*).* The error bars for the fit are about the size of the symbols.

.

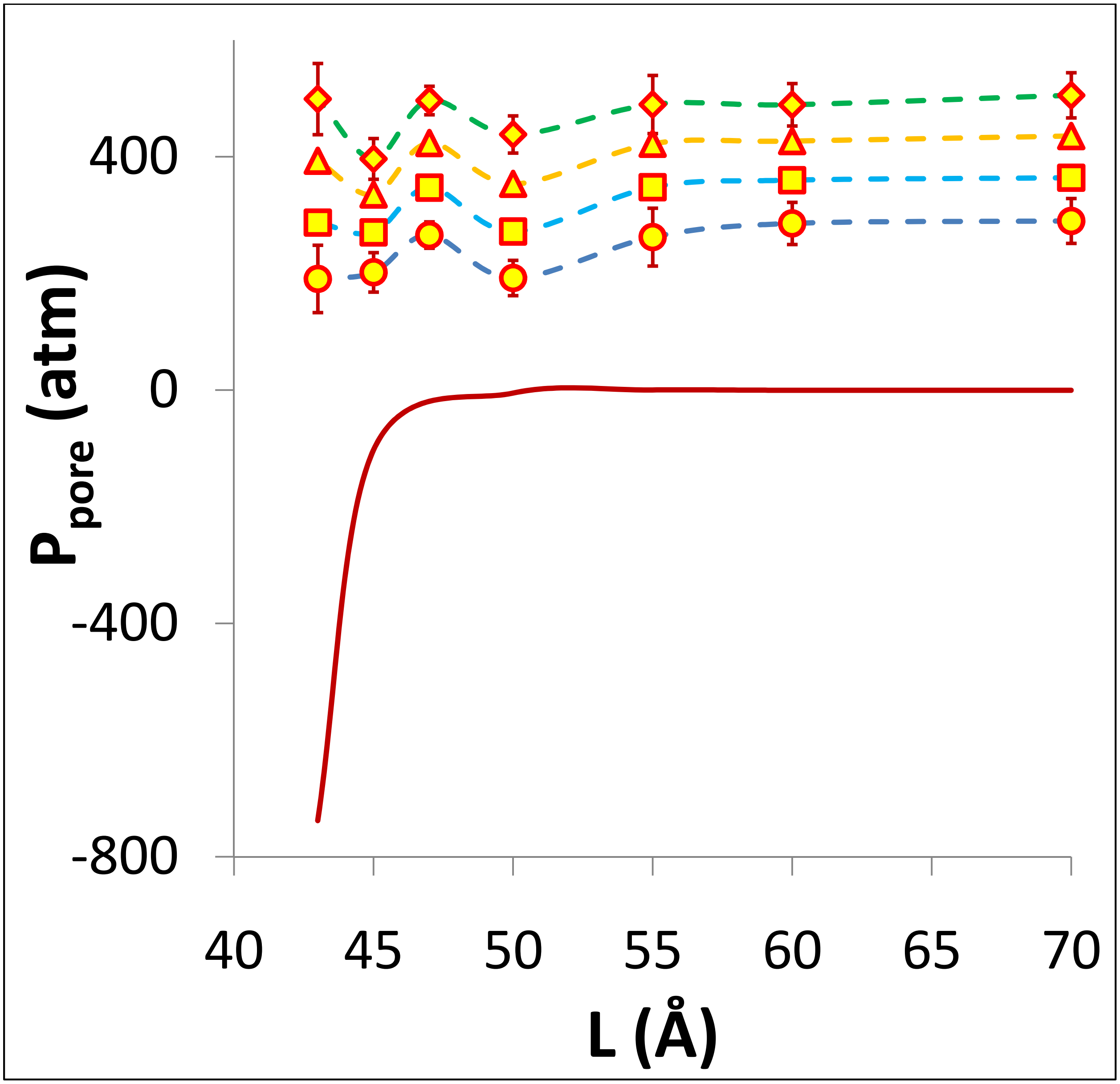

Figure 2.5: Plot of P_{pore} *vs. L* calculated using the procedure described in section 2.3 for dodecanethiol passivated pores solvated by CO_2 for various values of bulk pressures. The symbols are the result of said calculation for various values of *L* while the broken lines are meant to guide the eye. The four bulk pressures represented are $P_{bulk}=150$ *atm* (○), *Pbulk=200atm* (□), *Pbulk=250atm* (△) and $P_{bulk}=300$ *atm* (◇). The solid line is the corresponding curve for interactions in vacuum. For clarity, only error bars for $P_{bulk}=150$ *atm* and $P_{bulk}=300atm$ are shown. The error bars for the other pressures are similar. Interactions for *L<43Å* are strongly repulsive (high P_{pore}) and the corresponding values are not shown.

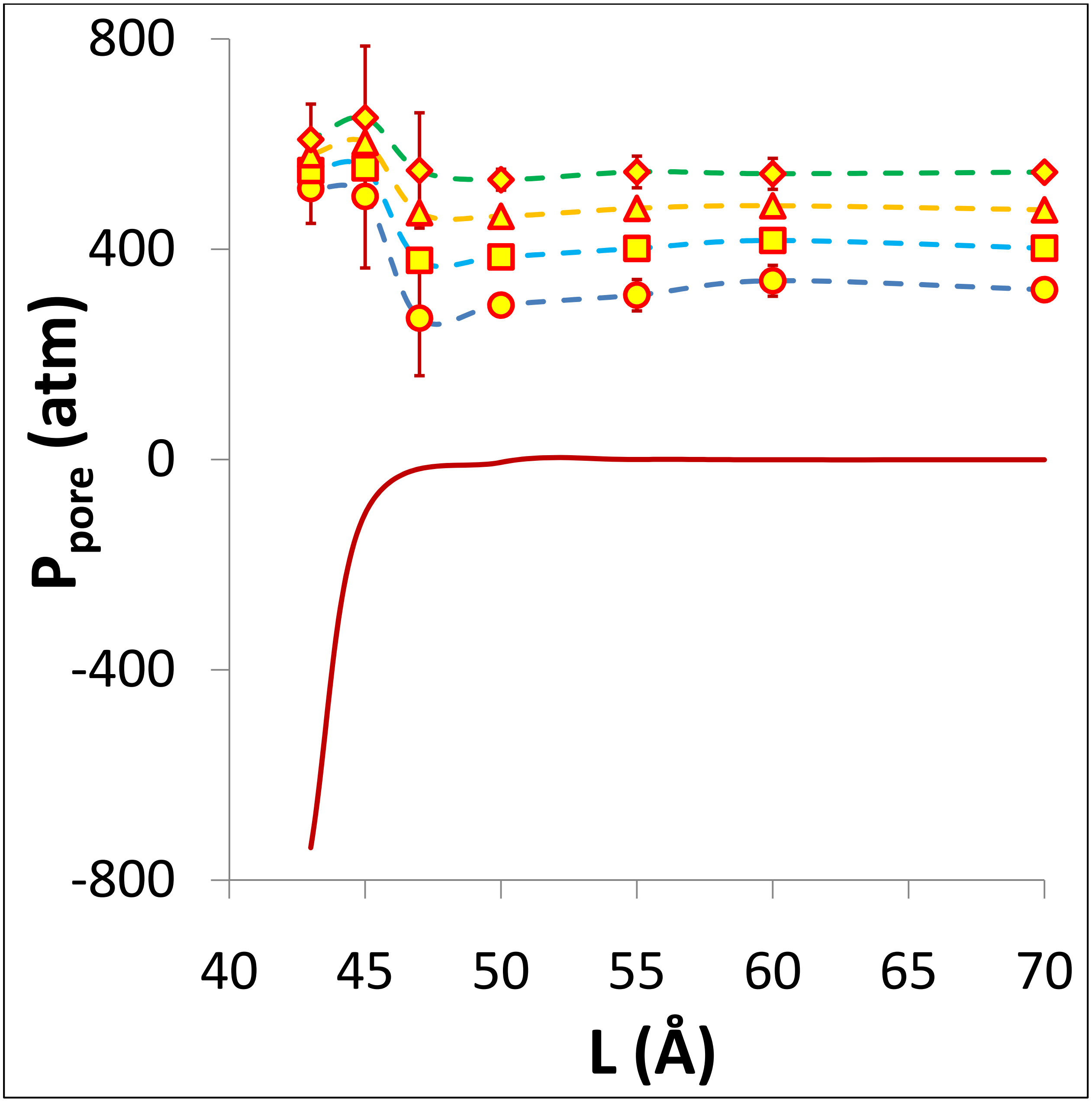

Figure 2.6: Plot of P_{pore} *vs. L* calculated using the procedure described in section 2.3 for dodecanethiol passivated pores solvated by Ethane for various values of bulk pressures. The symbols are the result of said calculation for various values of *L* while the broken lines are meant to guide the eye. The four bulk pressures represented are $P_{bulk}=150$ *atm* (○), *Pbulk=200atm* (□), *Pbulk=250atm* (△) and $P_{bulk}=300$ *atm* (◇). The solid line is the corresponding curve for interactions in vacuum. For clarity, only error bars for $P_{bulk}=150$ *atm* and $P_{bulk}=300$*atm* are shown. The error bars for the other pressures are similar. Interactions for *L<43Å* are strongly repulsive (high P_{pore}) and the corresponding values are not shown.

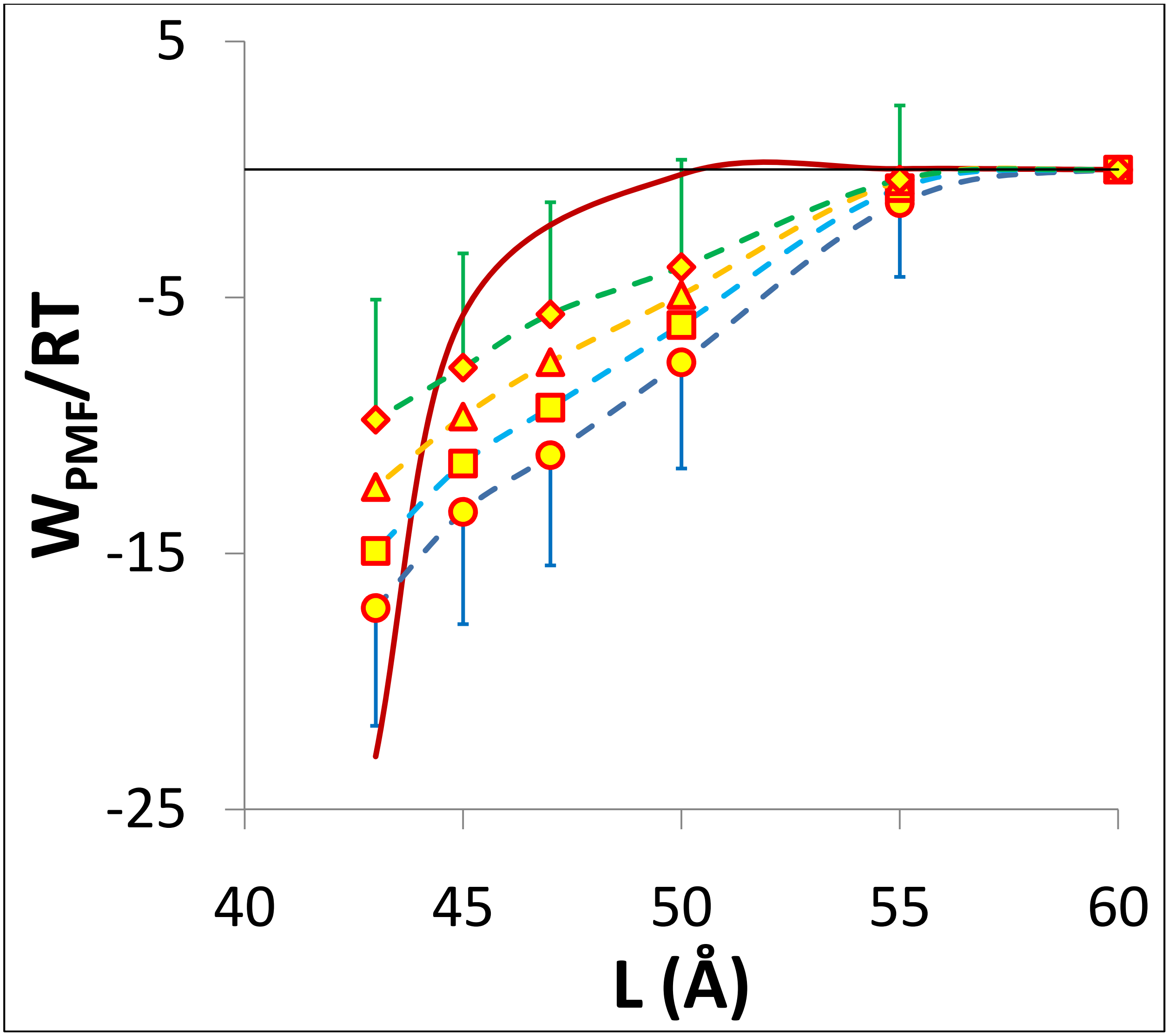

Figure 2.7: Potential of mean force of interaction between plates for dodecanethiol passivated slit pores solvated by CO_2 at various bulk pressures calculated as described in section 2.3. For the calculation P_{bulk}^{eff} is calculated using $L_{trunc}=60Å$ (see equation 2.7). The PMF corresponding to a single periodic image is attributed to a pair of particles to calculate the PMF per mole. The symbols are the result of said calculation for various values of *L* while the broken lines are meant to guide the eye. The four bulk pressures represented are $P_{bulk}=150$ *atm* (○), *Pbulk=200atm* (□), *Pbulk=250atm* (△) and $P_{bulk}=300$ *atm* (◇). The solid line is the corresponding curve for interactions in vacuum. For clarity, only the lower error bars for $P_{bulk}=150$ *atm* and the upper error bars for $P_{bulk}=300atm$ are shown. For this case, $L_{eq}=43$ *Å* and is the values for *L<43 Å* are not shown. For *L<43 Å*, the ligands compress and the interactions are repulsive.

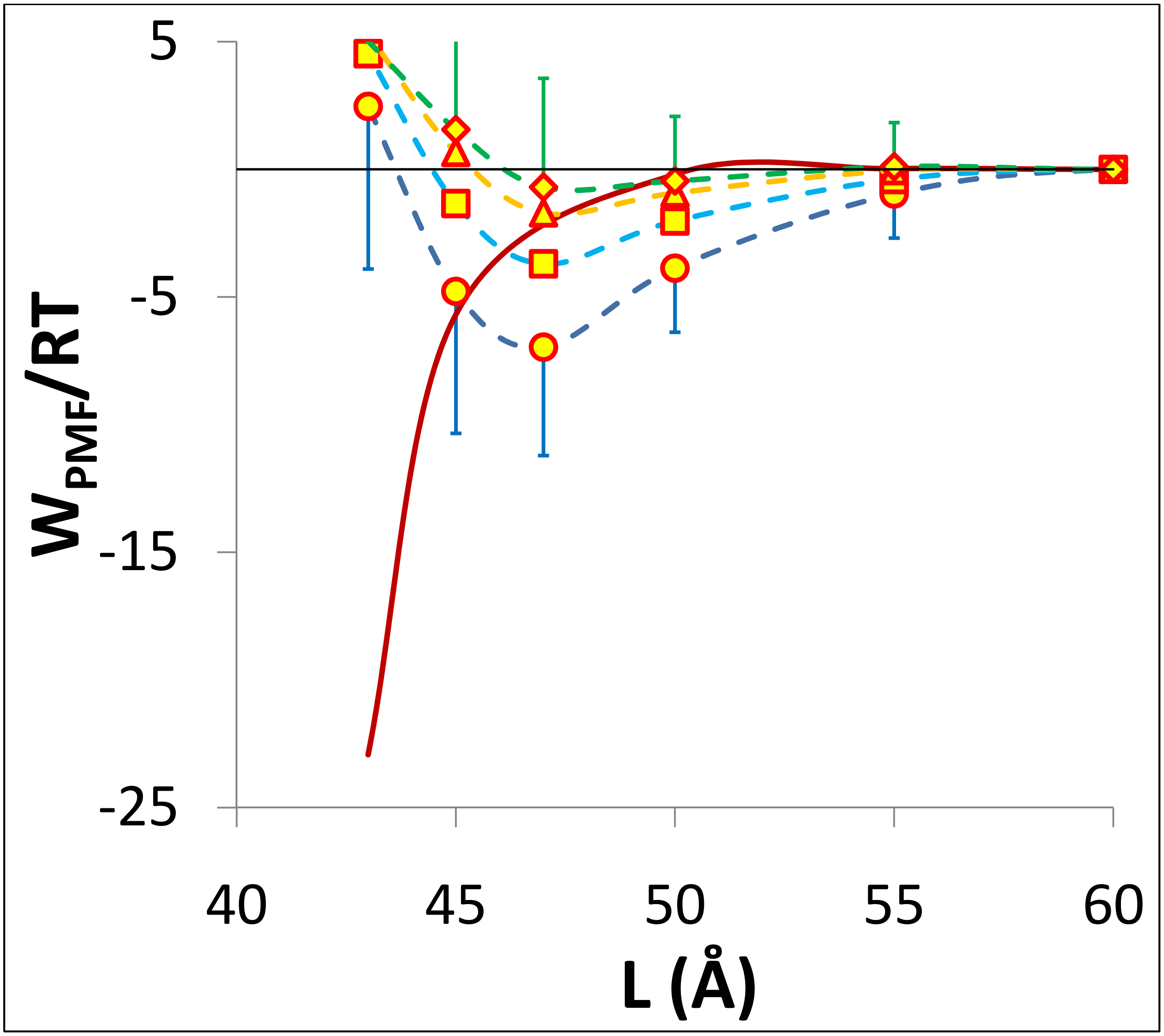

Figure 2.8: Potential of mean force of interaction between plates for dodecanethiol passivated slit pores solvated by ethane at various bulk pressures calculated as described in section 2.3**.** For the calculation P_{bulk}^{eff} is calculated using L_{trunc}*=60Å* (see equation 2.7). The free energy corresponding to a single periodic image is attributed to a pair of particles to calculate the free energy per mole. The symbols are the result of said calculation for various values of *L* while the broken lines are meant to guide the eye. The four bulk pressures represented are P_{bulk}*=150 atm (* ○ *), Pbulk=200atm (*□*), Pbulk=250atm (*△*)* and P_{bulk}*=300 atm (*◇*).* The solid line is the corresponding curve for interactions in vacuum. For clarity, only the lower error bars for P_{bulk}*=150 atm* and the upper error bars for P_{bulk}*=300atm* are shown. The values for *L<43 Å* are not shown. For *L<43 Å*, the ligands compress and the interactions are repulsive.

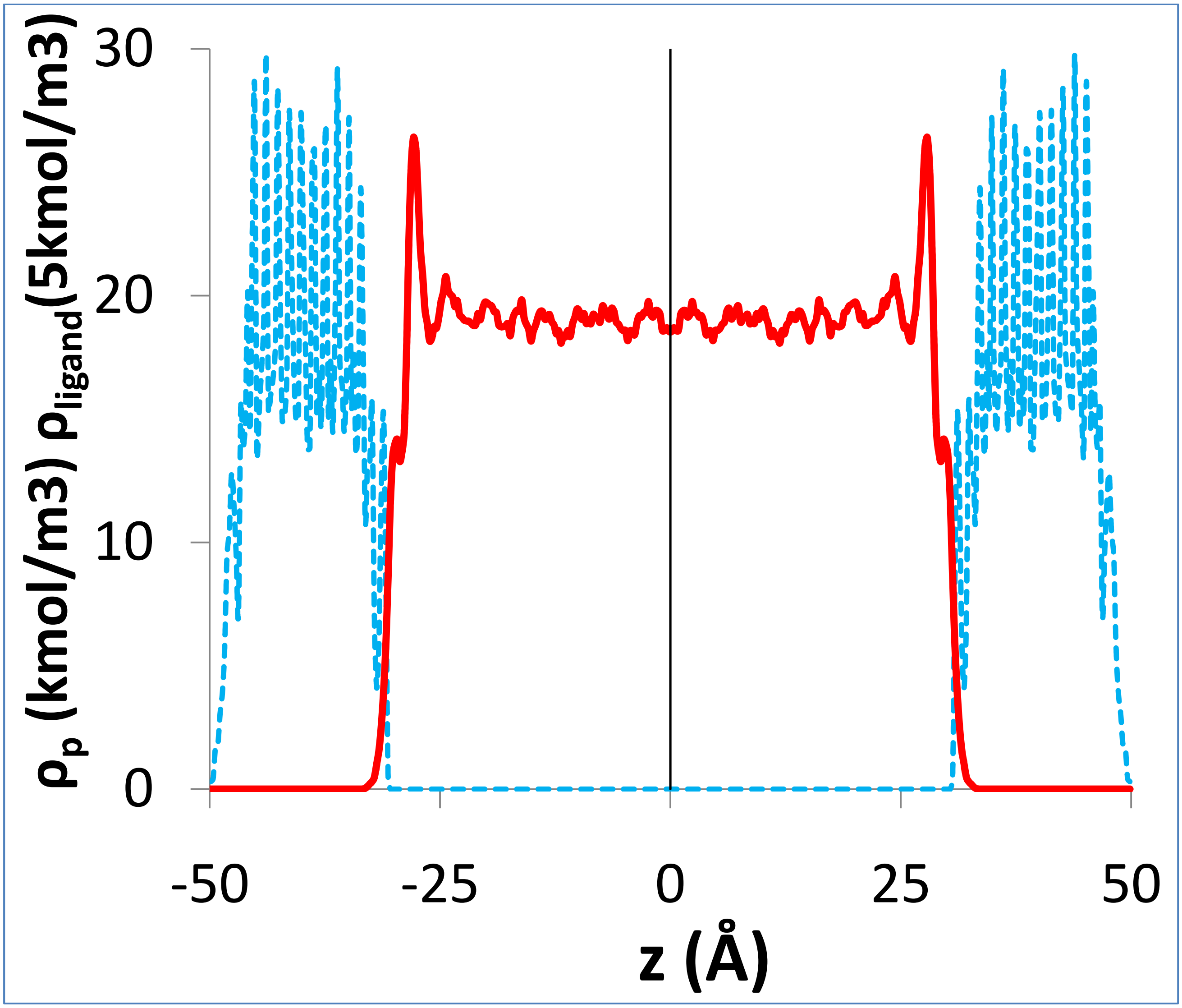

Figure 2.9: Density profile for a slit pore of gap-width $L=100\text{Å}$ passivated by n-dodecanethiol ligands and solvated by CO_2 at a bulk pressure of $P_{bulk}=172\ atm$. The density profile of the C atoms of the ligand (ρ_{ligand}) is shown by the broken line (■ ■) while the solvent density profile ρ_p is the solid line (▬). The density profile is determined using the entire cross section of the periodic image of the slit pore.

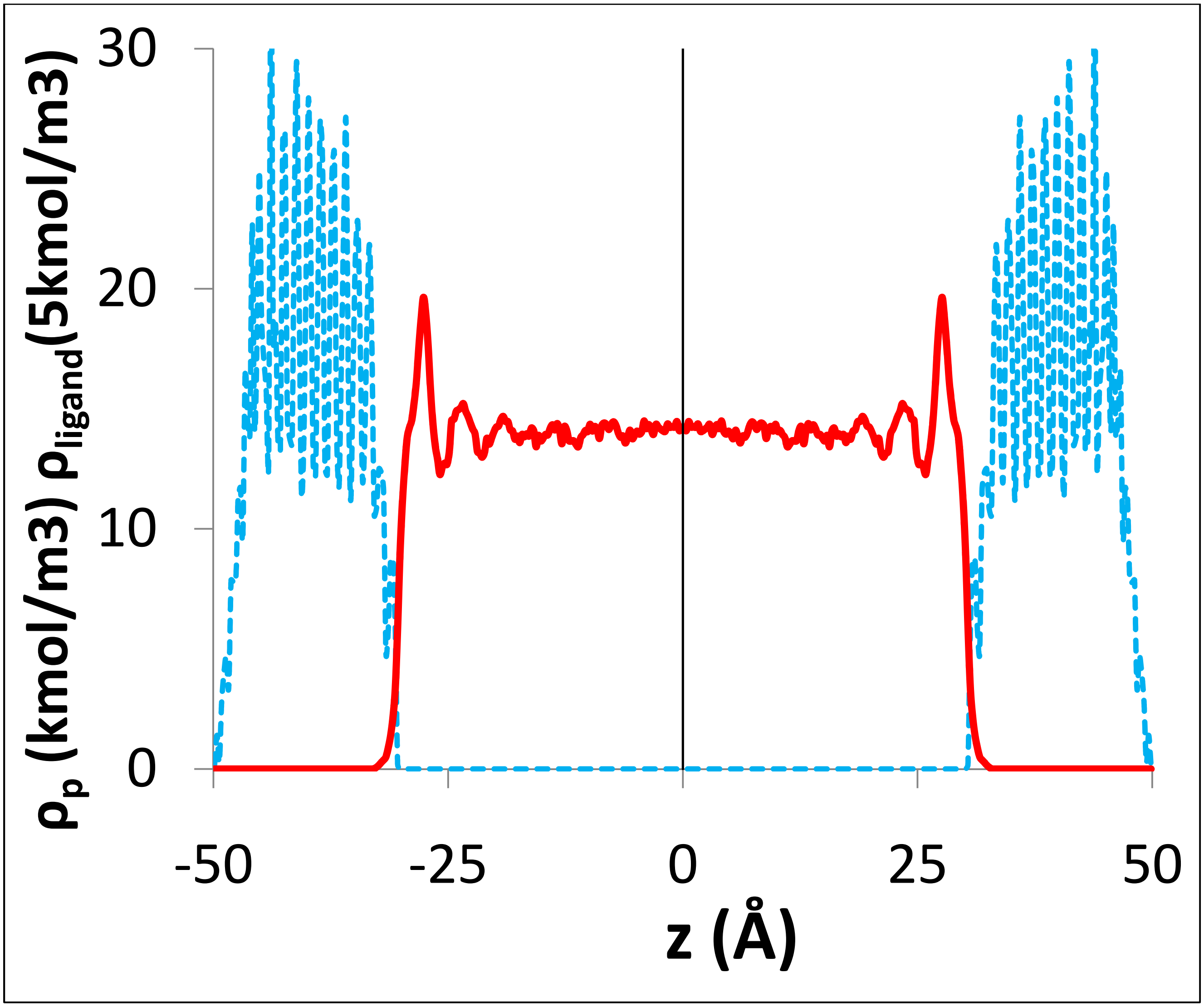

Figure 2.10: Density profile for a slit pore of gap-width $L=100\text{Å}$ passivated by n-dodecanethiol ligands and solvated by Ethane at a bulk pressure of $P_{bulk}=223\ atm$. The density profile of the C atoms of the ligand (ρ_{ligand}) is shown by the broken line (■ ■) while the solvent density profile ρ_p is the solid line (▬). The density profile is determined using the entire cross section of the periodic image of the slit pore.

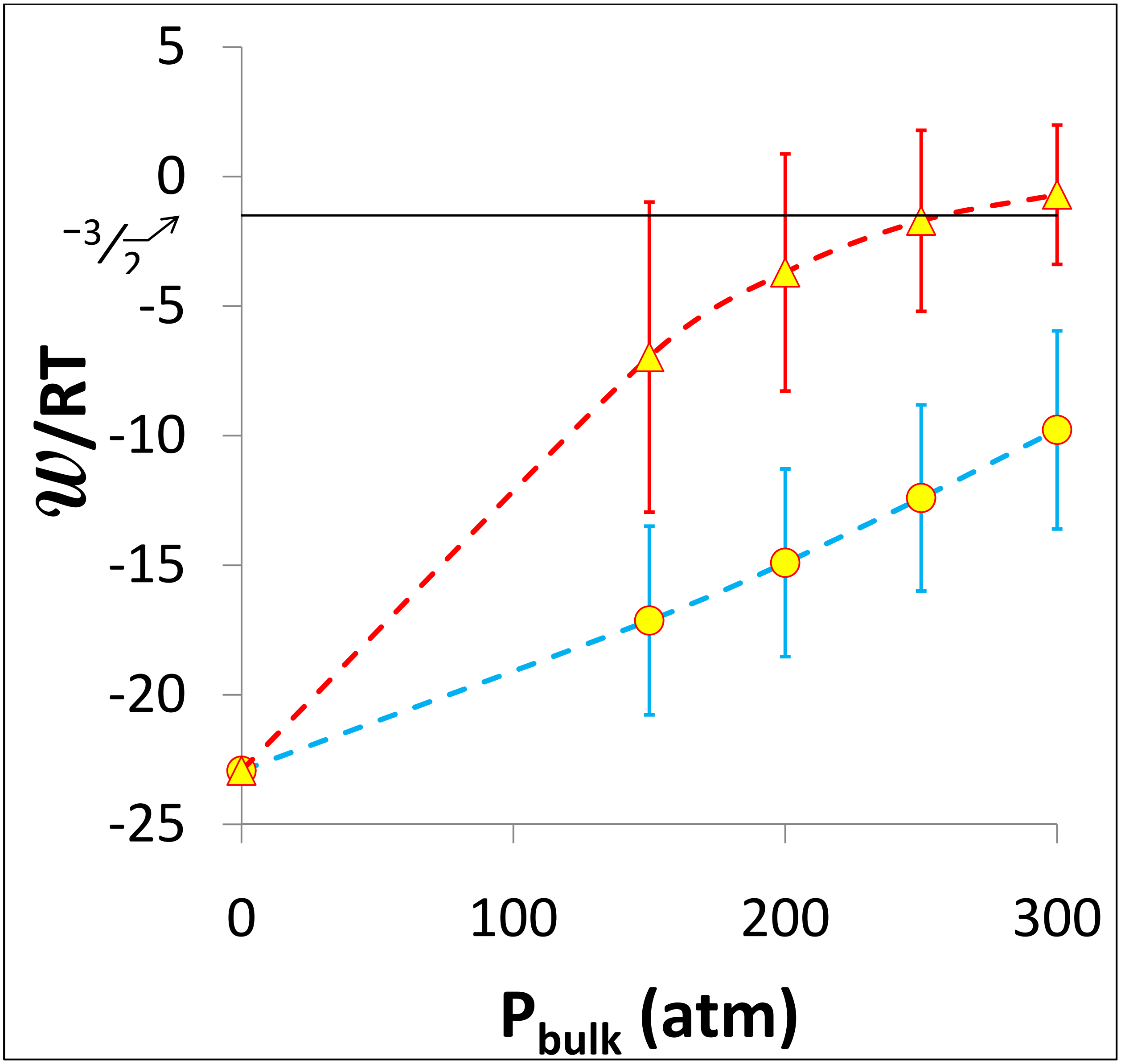

Figure 2.11: Plot of $\mathcal{W}$ v/s P_{bulk} (see equation 2.9) for n-dodecanethiol passivated slit pores solvated by CO_2 *(○* and *L_{eq}=43Å)* and Ethane *(△* and *L_{eq}=47Å).* The interactions for a single periodic image are attributed to a single particle pair or nanoparticles. The thin solid horizontal line corresponds to -1.5RT so that $\mathcal{W}$ values greater than this imply a thermodynamically stable dispersion. The dotted lines are guides to the eye.

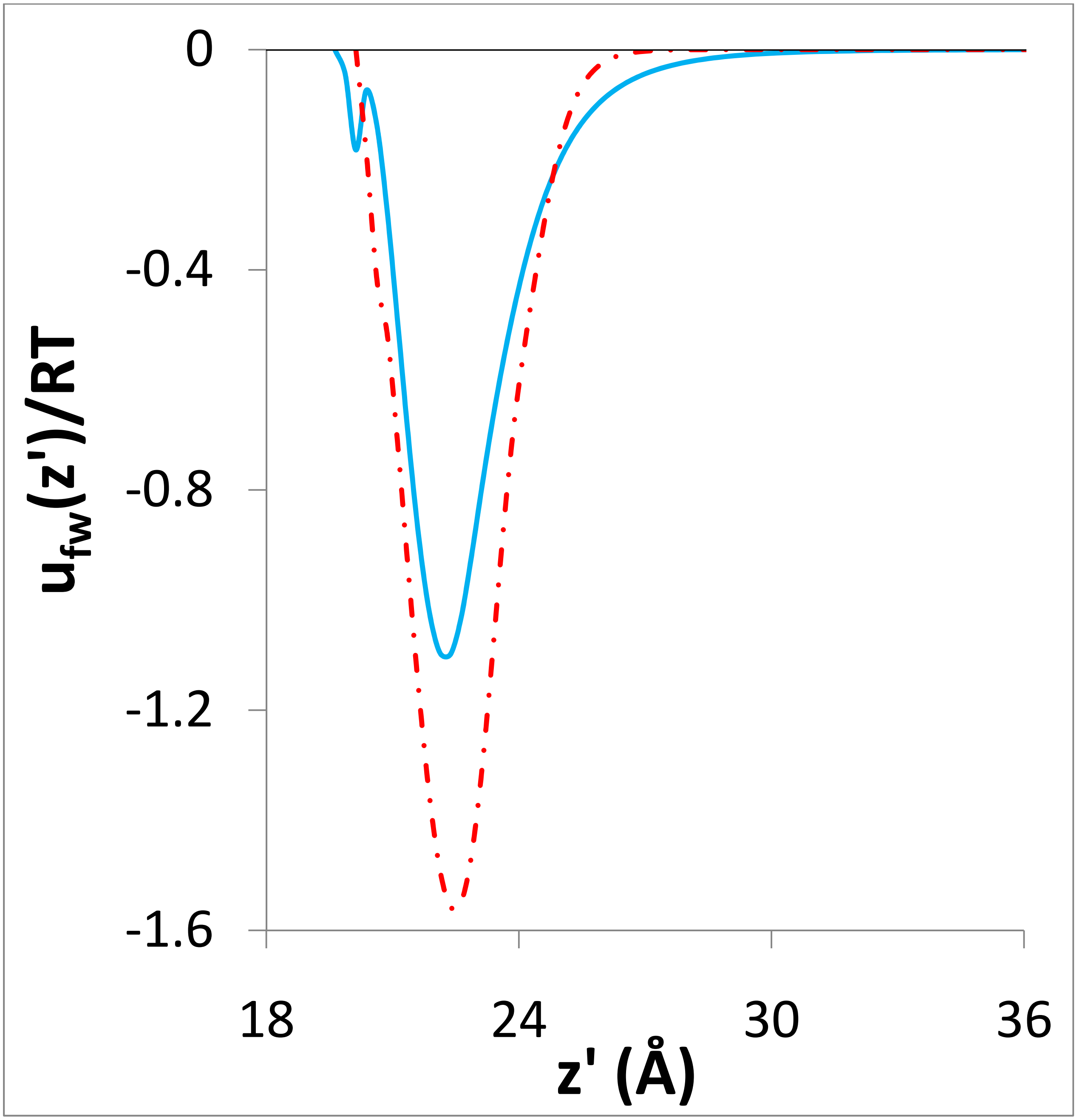

Figure 2.12: Wall-solvent interaction potential calculated using density profiles for wide slit pores (L=100Å) and the equation 2.21. The solid line (▬) is for CO_2 while the dotted-and-dashed line is for ethane (▬ ▪ ▬ ▪ ▬). Here *z′* is the perpendicular distance from the wall.

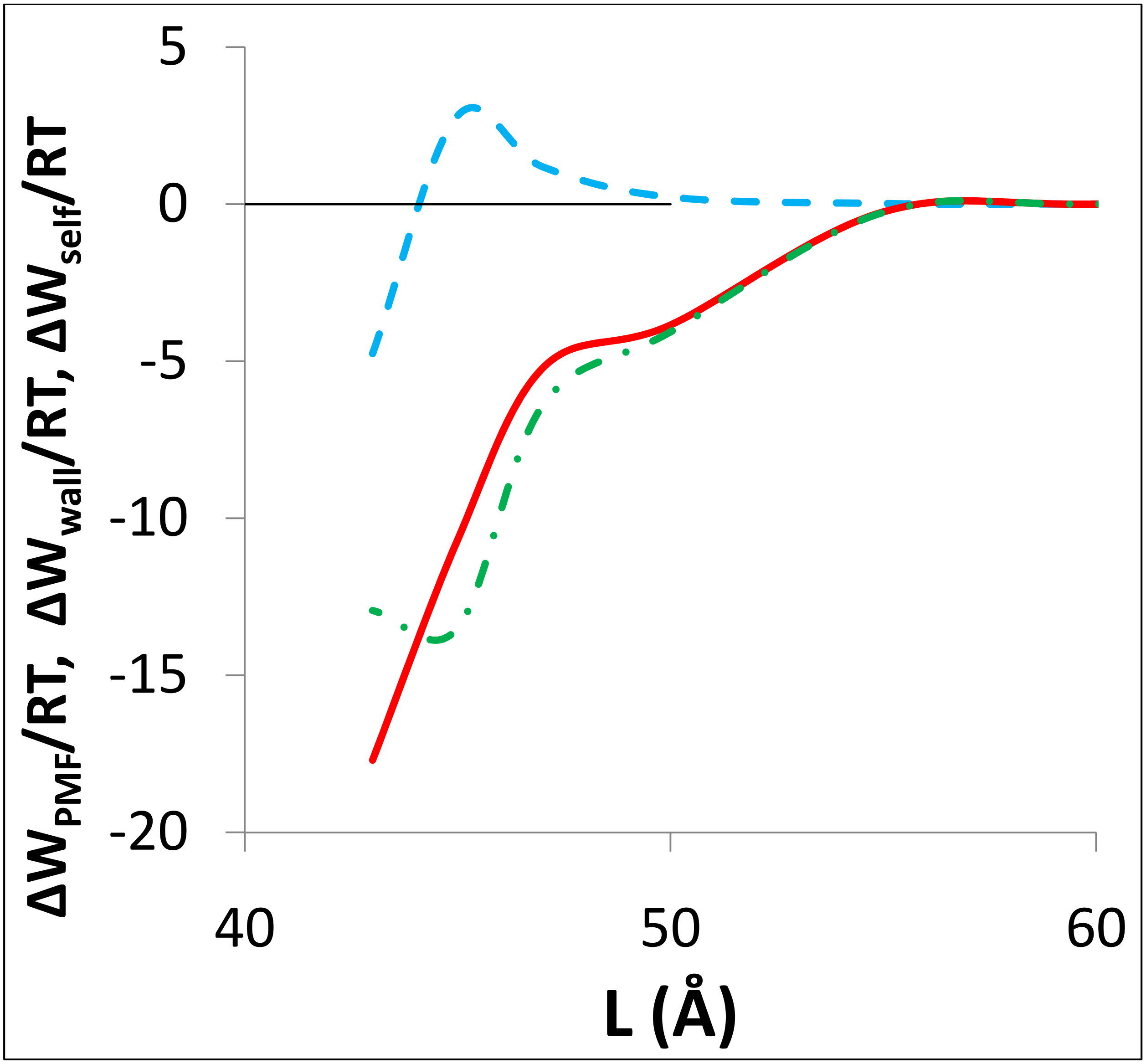

Figure 2.13: Plot showing difference in the solvation free energy W_{PMF} between CO_2 solvated pore and Ethane solvated pore (ethane value subtracted from CO_2 value) for different values of L for $P_{bulk}=300atm$. The solid line (▬▬▬) is ΔW_{PMF}, the broken line (▬ ▬ ▬)is ΔW_{wall} (measuring difference in affinity for the ligands) and the dotted-and-dashed line (▬ ▪ ▬) is ΔW_{self} (measuring difference in affinity for solvent bulk).

Chapter 3: Fluorocarbon Ligands for Nanoparticle Dispersions

3.1 Introduction

A proper understanding and control of the synthesis and assembly of nanoparticles is essential in order to cheaply and efficiently implement the great variety of promising new technologies collectively termed "nanotechnology". To collect, separate and deposit nanoparticles after synthesis, it is particularly important to be able to create and control their dispersions in a fluid media (Murray, Norris, & Bawendi, 1993). Bare nanoparticles of many interesting materials (metals, semiconductors, etc.) have high surface energies and need their surfaces passivated by capping ligands to disperse, at reasonable conditions of pressure and temperature, in common solvents (Shah, Hanrath, Johnston, & Korgel, 2004). The stability of dispersions of such ligand-passivated nanoparticles depends critically on the properties of the ligand-tail, the solvent, as well as conditions of temperature and pressure. Understanding the physical phenomena governing stability of ligand-passivated nanoparticle dispersions is of academic as well as industrial importance since certain solvents and ligands are more suited to large-scale applications than others (Sarbu, Styranec, & Beckman, 2000)(Potluri, Xu, Enick, Beckman, & Hamiltion, 2002) (Anand, Bell, Fan, Enick, & Roberts, 2006) (Patel & Egorov, 2007). Among the solvents, supercritical-fluids whose solvation power is a strong function of pressure would allow reversible and tunable stabilization of nanoparticle dispersions. Of these, supercritical carbon dioxide (ScCO_2) with its easily-accessed critical region combined with non-flammability and non-toxicity would be especially attractive. However, only nanoparticles capped with ligands whose tails are composed of perfluoropolyethers (Saunders & Korgel, 2004) and perfluoroalkanes (Shah, Husain, Johnston, & Korgel, 2002) have so far been identified as forming stable dispersions in ScCO_2 at convenient conditions of temperature (near ambient) and pressure (<500 bar). These ligands are expensive, practically xenobiotic (Resnati, 1993) and can form degradation products that are environmentally persistent and toxic (Pelley, 2004). On the other hand, cheap and benign hydrocarbon-tailed ligands e.g. dodecanethiol, which do effectively disperse nanoparticles in organic solvents like toluene (Brust, Walker, Bethell, Schiffrin, & Whyman, 1994), hexane (Shah, Holmes, Doty, Johnston, & Korgel, 2000) and supercritical ethane (Clarke, Waters, Johnson, Satherley, & Schiffrin, 2001) (Shah, Holmes, Johnston, & Korgel, 2002) under similar conditions, prove ineffective in ScCO_2. Indeed CO_2 is actually found to be an *anti*-solvent for dodecanethiol passivated gold nanoparticles (Gupta, Shah, Zhang, Saunders, Korgen, & Johnston, 2005) as well as organic-polymeric nanoparticles dispersed in toluene (Chang, Lee, & Lin, 2007) (Dixon, Johnston, & Bodmeier, 2004). In anticipation of industrial-scale processing of nanoparticles, there is continuing interest in developing a non-fluorous ligand for dispersing nanoparticles in ScCO_2 (Sarbu, Styranec, & Beckman, 2000) (Potluri, Xu, Enick, Beckman, & Hamiltion, 2002) (Anand, Bell, Fan, Enick, & Roberts, 2006). Furthermore, insights gained from such an endeavour are relevant to understanding the role of surfactants in CO_2-water emulsions (da Rocha, Johnston, & Rossky, 2002) (Stone, da Rocha, Rossky, & Johnston, 2003) – pertinent to enhanced oil recovery (Rossen, 1996), biology (Johnston, et al., 1996) (Harrison, Goveas, Johnston, & O'Rear, 1994), “green” chemistry (DeSimone, 2002) (Sagisaka, et al., 2008) and other applications (Johnston & da Rocha, 2009).

In the previous chapter we proposed a method for using molecular simulations to gauge the effectiveness of certain ligand-solvent combinations and the various factors influencing it. We used the method to determine that the reasons for the effectiveness of n-dodecanethiol ligands in supercritical ethane (Shah, Holmes, Johnston, & Korgel, 2002) and its ineffectiveness in supercritical CO_2 (Shah, Holmes, Doty, Johnston, & Korgel, 2000) is not just that CO_2 interacts somewhat more weakly with the ligands in comparison to ethane but also because CO_2, being smaller and possessing a strong quadrupole that ethane lacks, is more cohesive. Hence, comparing ethane and CO_2, CO_2 has a significantly weaker affinity for the dodecanethiol ligands, *compared to its own bulk*. We have therefore concluded that if a ligand is to be effective in ScCO_2, its passivation layers on the nanoparticle surfaces should provide the interactions necessary to adequately compensate CO_2 not only for the loss of its Van der Waals interactions with its bulk but also for its quadrupolar interactions.

Here we examine two common experimentally studied fluorocarbon ligands - perfluorooctanethiol (Shah, Husain, et al. 2001). and perfluorodecanethiol (Shah, Husain, Johnston, & Korgel, 2002) – which are known to stabilize dispersions of silver nanoparticles in $ScCO_2$. Our simulations capture this phenomenon and are used to demonstrate that fluorocarbons are effective in $ScCO_2$ for three reasons: First, they are relatively CO_2-philic, owing significantly to electrostatic interactions between dipolar C-F bonds and the quadrupoles of CO_2. Second, the fluorocarbons have a geometry that ensures that their local dipoles are always *adverse* to those of other fluorocarbons so that the electrostatic interactions between fluorocarbon molecules are always *repulsive*. Finally, the fluorocarbon ligands, being fatter, pack more sparsely than the corresponding hydrocarbon ligands. Hence fluorocarbon-passivated surfaces have a weaker dispersion interaction with each other and with CO_2, although for CO_2 this is offset by higher electrostatic interactions. These attributes allow fluorocarbons to behave like good ligands in $ScCO_2$, where they have relatively high affinity for the solvent and relatively low affinity for themselves.

This chapter is organized as follows: The relevant experimental observations are summarized in Section 3.2, the simulation strategy and setup in Section 3.3 and the results are reported and discussed in Section 3.4.

3.2 Experimental Observations

The experimental observations that are relevant to this work are: perfluoroalkane passivated metal nanoparticles disperse in supercritical CO_2 at conditions of pressure and temperature where n-dodecanethiol passivated nanoparticles do not disperse.

1. It is found that dodecanethiol-capped silver nanocrystals do not disperse in $ScCO_2$ even at very high pressures (> 300 atm). However they disperse if n-hexane is added as a co-solvent in substantial amounts (>50%v/v) (Shah, Holmes, Doty, Johnston, & Korgel, 2000). Further, CO_2 is actually found to be an *anti*-solvent for dodecanethiol passivated gold nanoparticles (Gupta, Shah, Zhang, Saunders, Korgen, & Johnston, 2005) as well as organic-polymeric nanoparticles dispersed in toluene(Chang, Lee, & Lin, 2007), (Dixon, Johnston, & Bodmeier, 2004).
2. Silver nanoparticles were successfully synthesized in $ScCO_2$ (at 80^oC and 276 atm) in the presence of perfluoro-octanethiol ligands. The ligands controlled particle growth (size range 26-107Å diameter) and prevented flocculation during synthesis. It was noted that once the perfluoro-octanethiol-passivated particles were precipitated, they could not be redispersed in $ScCO_2$ (Shah, Husain, et al. 2001).
3. Silver nanoparticles capped with perfluoro-decanethiol ligands could be redispersed at 80^oC and 276 atm (Shah, Husain, Johnston, & Korgel, 2002). Perfluorodecanethiol capped particles could be dispersed in liquid CO_2 at 25^oC at pressures as low as 62 atm (Shah, Holmes, Doty, Johnston, & Korgel, 2000).

3.3 Simulation Strategy and Computational Details

Since our simulation strategy is described in detail in the previous chapter, we will only reproduce the salient points here. Our goal is to gain an insight into the physical phenomena that occur in the solvent region between two ligand-passivated spheres. This region is marked in Figure 3.1a. To save considerably on computational effort without loss of physical insight, we generate a *slit-pore* whose walls are "bumpy" with the radius of curvature of the bumps being equal to the nanoparticle size (see Figure 3.1b,c). To better reflect experimental data and compare with our other simulations, we have taken this to be a particle of *60Å* diameter. The setup with perfluorodecanethiol ligands is shown in Figure 3.1c. The system consists of 536 silver atoms approximated by LJ particles arranged in an FCC lattice to form two plates, each three atomic layers thick. The ligand roots (S-atoms) are distributed on the inner surface of the plates (see Figure 3.1d). The dimensions of the periodic system for both cases along the *x*- and *y*- directions i.e. along the face of the plates are 28.8Å by 29.92Å respectively. The system is periodic in these directions but not in the *z*-direction. The z-direction separation between the nearest silver atoms of the opposite plates is taken as the gap-width *L* (see Figure 3.1c). The ligands' molecular structures are shown in Figure 3.1e (for perfluorodecanethiol) and Figure 3.1f (for perfluorooctanethiol). The dynamics are implemented using the DL_POLY 2.15 package (Smith & Forester, 2003) and the results visualized using VMD (Humphrey, Dalke, & Schulten, 1996). The force field used is OPLS-AA (Jorgensen, 2002) except for carbon-dioxide which is modeled using the EPM2 model (Harris & Yung, 1995) and Ag whose LJ parameters (σ_{Ag}=2.708Å, ε_{Ag}=0.2668kcal/mol) are set to approximate long range attractive interaction between Xe (Berry, Rice, & Ross, 2000) and Ag(111) calculated ab-initio (Vidali, Ihm, Kim, & Cole, 1991) (Gatica, Li, Trasca, Cole, & Diehl, 2008). These molecular models are essentially the same as those used to investigate surfactant behavior at water-CO_2 interfaces (da Rocha, Johnston, & Rossky, 2002) (Stone, da Rocha, Rossky, & Johnston, 2003) except for the dihedral potentials of the fluorocarbon backbone that are truncated to three terms instead of four (to eliminate an unphysical bimodal energy well) and for the partial charges on the fluorinated groups. The OPLS-AA (Jorgensen, 2002) value for the partial charge on F of perfluoroalkanes is -0.12e except for monoalkyl fluorides where it is -0.2e. In an application to fluoroalkanes, Li et al (2006) (Li, Li, Eleftheriou, & Zhou, 2006) consider the latter to include F on CF_3 groups of perfluoroalkanes. The higher terminal group charge is consistent with the fact that the partial charge of F in CF_3 of CF_3CHFCF_3 has been calculated *ab-initio* to vary with environment from -0.158e to -0.205e (Peguin & da Rocha, 2008) and that the partial charge on F of CF_4 is calculated to be -0.17e (Raveendran & Wallen, 2003), -0.2376e (Jang, Blanco, Goddard III, Cladwell, & Ross, 2003), -0.15e (Potter, Tildesley, Burgess, & Rogers, 1997), -0.189e (Gough, Pearlman, & Kollman, 1993). We recalculated partial charges on perfluoropentane using ESP charge fitting with basis 6-31G(p,d) using the available routine in GAMESS (Schmidt, et al., 1993) to yield average values of $q_F(CF_3)=-0.17e$ and $q_F(CF_2)=-0.12e$ in agreement with the above mentioned values. The charges on the carbons of CF_3 and CF_2 groups are adjusted to make the groups individually charge-neutral.

The ligand packing density on the nanoparticle surface is obtained indirectly. From a study of dodecanethiol ligands on Ag(111) surfaces, it appears that they pack according to their molecular cross sectional area on planar surface so that the density is 18.9Å^2/ligand (Fenter, Eisenberger, Li, Camillone III, Bernasek, & Scoles, 1991), unlike the same ligands on Au(111) surfaces where the packing (21.19Å^2/ligand) is dictated by the surface (Ulman, 1989) (Rovida & Pratesi, 1981) (Sellers, Ulman, Shnidman, & Eilers, 1993). On a curved surface, the ligands pack more densely with a density of 16Å^2/ligand (Korgel, Fullam, Connolly, & Fitzmaurice, 1998). To determine fluorocarbon packing density, we allow each ligand a density of 28.3Å^2/ligand corresponding to their molecular cross-sectional area (Kirsch, 2004) at a distance of 6.15Å from the nanoparticle surface. This distance incorporates the distance of the S atom from the surface Ag atoms (=1Å taken to be same as the Au-S distance (Jadzinsky, Calero, Ackerson, Bushnell, & Kornberg, 2007)) and the length of the $S\text{-}CH_2\text{-}CH_2\text{-}CF_2$ linker stretch

(5.15Å). Since this density is at a radius of 30+6.15Å, the density of the packing at the surface (i.e. radius of 30+1Å) is 20.8Å^2/ligand. Hence, the distribution of the ligand roots according to a hexagonal lattice corresponds to a lattice spacing of 4.8Å (Figure 3.1d).

The metric used to quantify effectiveness is the *free energy of flocculation* $\mathcal{W}$ which is calculated using the procedure described in detail in chapter 1. We will quickly reproduce the salient points here. $\mathcal{W}$ is given by:

$$\mathcal{W}(P_{bulk}) = W_{PMF}(\xi_{bulk}, L_{eq}) \qquad \text{… (3.1)}$$

where ξ_{bulk} is the externally imposed (bulk) solvent activity, W_{PMF} is the potential of mean force between opposing walls of solvated slit-pore, L_{eq} is the equilibrium gap-width (free energy minimum) and P_{bulk} is the nominal bulk pressure corresponding to ξ_{bulk}. W_{PMF} is given by:

$$W_{PMF}(\xi_{bulk}, L) = \int_{L_{trunc}}^{L} \left[P_{pore}(\xi_{bulk}, L') - P_{bulk}^{eff}(\xi_{bulk}) \right] A_{pore}\, dL' \qquad \text{… (3.2)}$$

where L_{trunc} is the gap-width at which $P_{pore}(\xi_{bulk}, L)$ (the normal pressure in the pore at the given activity and gap-width L), no longer varies with increasing L, reaching the value $P_{bulk}^{eff}(\xi_{bulk})$. A_{pore} is the cross-sectional area in the pore. $P_{bulk}^{eff}(\xi_{bulk})$ is the averaging over $L \geq L_{trunc}$:

$$P_{bulk}^{eff}(\xi_{bulk}) = \text{average}\left\{ P_{pore}(\xi_{bulk}, L) : L \geq L_{trunc} \right\} \qquad \text{… (3.3)}$$

Using a series of canonical ensemble simulations (Frenkel & Smit, 2002) for fixed *L's* and different values of pore density ($\rho_{pore}=N_{pore}/A_{pore}/L$ where N_{pore} is the number of solvent molecules in a single periodic image of the pore) we fit the isothermal equation of state for gap-width L to the following van der Waals form which is obtained from an analytical treatment of planar slit pores and involves an assumption of a flat density profile in the pore (Schoen & Diestler, 1998):

$$P_{pore}\left(\rho_{pore}, L\right) = a_0 + \frac{\rho_{pore} RT}{1 - a_1 \rho_{pore}} + a_2 \rho_{pore} + a_3 \rho_{pore}^2 \qquad \text{… (3.4)}$$

Here, *R* is the universal gas constant and a_0, a_1, a_2 and a_3 are the parameters to be fitted independently for each *L*. An apparent advantage of this approach is that the fit pressure appears to suppress the effect of random errors at individual state points on consequent results. From the configurational snapshots generated during the canonical ensemble simulations, the excess chemical potential in the pore (μ_{pore}^{ex}) is calculated using Widom insertions (Widom, 1963) (Frenkel & Smit, 2002). These can be fitted to the following form (Schoen & Diestler, 1998):

$$\beta\mu_{pore}^{ex}\left(\rho_{pore}, L\right) = a_{\mu 0} - \ln\left(1 - \rho_{pore} a_{\mu 1}\right) + \frac{\rho_{pore} a_{\mu 1}}{1 - \rho_{pore} a_{\mu 1}} + a_{\mu 2} \rho_{pore} \qquad \text{… (3.5a)}$$

Here $\beta = (RT)^{-1}$ and $a_{\mu 0}$, $a_{\mu 1}$, $a_{\mu 2}$ are parameters to be fitted independently for each *L*. The excess chemical potential is related to the activity by the simple relation:

$$\xi_{pore}\left(\rho_{pore}, L\right) = \rho_{pore} \exp\left(\beta\mu_{pore}^{ex}\right) \qquad \text{… (3.5b)}$$

The value of pore density at a given *L* and ξ_{bulk} is obtained by solving:

$$\xi_{pore}\left(\rho_{pore}, L\right) = \xi_{bulk} \qquad \text{… (3.6)}$$

We find that for a fixed ξ_{bulk} the pore density values fit the following simple form:

$$\rho_{pore}^{fit}\left(\xi_{bulk}, L\right) = \rho_{bulk}\left(\xi_{bulk}\right)\left(1 - \frac{2l_o}{L}\right) \qquad \text{… (3.7)}$$

where ρ_{bulk} is the bulk density corresponding to ξ_{bulk} and l_o is a constant. It is these values of $\rho_{pore}^{fit}\left(\xi_{bulk}, L\right)$ that are used with equation 3.4 to get P_{pore} values for equations 3.2 and 3.3. P_{bulk} is obtained from ρ_{bulk} and a separately calculated equation of state using the molecular model of the solvent. The data is then fitted to the following two-parameter form (Schoen & Diestler, 1998):

$$P_{bulk} = \frac{RT\rho_{builk}}{1-\rho_{bulk}b} - a_{bulk}\rho_{bulk}^{2} \qquad \text{… (3.8a)}$$

$$b = \frac{2}{3}\pi\sigma_f^3 \text{ and } a_{bulk} = \frac{16\pi}{9}\sigma_f^3\varepsilon_f \qquad \text{… (3.8b)}$$

Where σ_f and ε_f are fluid-specific characteristic constants obtained by fitting equation 3.8 to the equation of state. The physical interpretation of the constants is that σ_f is the diameter of the core of the fluid particles while ε_f is their attractive energy parameter. The details of the simulations are described in the previous chapter. We have obtained values of W_{PMF} and $\mathcal{W}$ corresponding to P_{bulk}*=150, 200, 250* and *300* atm.

3.4 Results and Discussion

The ρ_{pore} *vs.* $1/L$ plots for both types of passivation (see Figure 3.2 and Figure 3.3) in CO_2 solvated pores at $P_{bulk}>150atm$ are linear. Using the methods described in Section 3.3, P_{pore} *vs.* L curves for different values of P_{bulk} are calculated for CO_2 solvated pore passivated by perfluorodecanethiol (Figure 3.4) and perfluorooctanethiol (Figure 3.5) so that, using equation 3.2, we get W_{PMF} *vs.* L plots for various values of P_{bulk} (see Figure 3.6 and Figure 3.7). Density profiles in a large gap (L=100Å) slit pore for both solvent and ligand appear in Figure 3.8 and Figure 3.9 for perfluorodecanethiol and perfluorooctanethiol passivated pores respectively. Identifying L_{eq}=43Å (in vacuum, $L_{\text{eq-vac}}$=40Å) for perfluorodecanethiol passivated pore and L_{eq}=35Å ($L_{eq\text{-}vac}$=33Å) for perfluorooctanethiol passivated pore, we get, from equation 3.1, the $\mathcal{W}$ *vs.* P_{bulk} plots seen in Figure 3.10. In the absence of solvent, equilibrium occurs at $L_{eq\text{-}vac}$ and, for $L<L_{eq\text{-}vac}$, the overlap of ligand regions causes large repulsive interactions. Upon fitting the equation of state to the form of equation 3.8 we get parameters for CO_2 ($\varepsilon_f = 0.807\text{kcal/mol}$, $\sigma_f = 2.9\overset{\text{o}}{\text{A}}$).

After first discussing the consistency of our results with experimental observations, we will comment on the applicability of previous models developed for polymer brushes in describing systems of densely packed short chain ligands. We will then examine the implications of the linearity of the ρ_{pore} *vs.* $1/L$ to make simplifying assumptions in order to develop a simple interpretive model to describe the behavior of the two systems. Using this model we will determine the molecular level causes of the effectiveness of the fluorocarbon ligands in $ScCO_2$.

3.4.1 Consistency with Experimental Observations

We have in Figure 3.10 included for comparison the $\mathcal{W}$ *vs.* P_{bulk} plot for the dodecanethiol passivated pore ($L_{eq}=L_{vac}$=43Å) using data from the previous chapter. It is quite apparent that the systems are stabilized much better by the perfluorocarbon ligands than by the n-dodecanethiol ligands – consistent with experimental observations. The experiments on redispersion of perfluorodecanethiol passivated particles showed that at 353K (80^{o}C), the pressure for redispersion (*flocculation pressure*) of 20-40Å diameter nanoparticles is 272 atm. Our simulations are done at 308K and seek to approximate a 60Å diameter nanoparticle to better compare with our earlier results. To roughly estimate the anticipated flocculation pressure at 308K, we use the equality of the Flory-Huggins interaction parameter $\chi = \frac{v_{solvent}}{RT}\left(\delta_{solvent} - \delta_{solute}\right)^2$ (which should be less than 0.5 for good solvent conditions). Here $v_{solvent}$ is the molar volume, R is the universal gas constant, T is the temperature and $\delta_{solvent}, \delta_{solute}$ are the Hildebrand solubility parameters of the solvent (ScCO$_2$) and solute (ligand passivated nanoparticle), respectively. Using a standard database (http://webbook.nist.gov/chemistry/fluid/), we can calculate (Allada, 1984) at T=353K and P_{bulk}*=272atm*, $v_{solvent}^{353K}$=60.7cm^3/mol and $\delta_{solvent}^{353K}$=11.2 (J/cm^3)$^{0.5}$. Using dodecane at 500 atm as the solute, we get δ_{solute}^{353K}=15.8(J/cm^3)$^{0.5}$ so that for χ^{353K}=0.432. Now since the packing density of the ligands is independent of temperature at the given temperature range, we calculate for δ_{solute} the value for dodecane at 80atm at 308K (same density as dodecane at 500atm and 353K), i.e. δ_{solute}^{308K}=16.0(J/cm^3)$^{0.5}$. Using this value, to get χ^{308K}=0.432, we find the solvent pressure of 105 atm at 308K. The value obtained by simply equating solvent densities at the two conditions is nearly the same at 100 atm. Experiments with polymers dispersed in ScCO$_2$ (O'Neill, et al., 1998) have suggested that density is the natural variable determining solvation behavior.

In our simulations, we take the flocculation pressure to be one at which $\mathcal{W}$ *<-1.5k*$_B$*T* , which is a reasonable criterion(Shah, Holmes, Johnston, & Korgel, 2002). From the $\mathcal{W}$ *vs.* P_{bulk} plots (Figure 3.10) for a 60Å diameter nanoparticle passivated by perfluorodecanethiol, we find the flocculation pressure is ~150 atm. Since the experimental nanoparticles are smaller in diameter (20-40Å) than the one our simulation (60Å) represents, it is expected that the experimental flocculation pressure would be lower

(Fernandez-Nieves, Fernandez-Barbero, Vincent, & de las Nieves, 2001). We can see that the two fluorinated ligands appear to perform equally well. Hence we infer that the inablility of perfluorooctanethiol passivated nanoparticles to redisperse after precipitation (Shah, Husain, et al. 2001) has to do with phenomena in the flocculated state which our method is not designed to address.

3.4.2 Solvent does not "solvate" ligands

As we have noted in the last chapter, the ligands are too short and pack too densely to use models developed for polymer brushes (Meredith, Sanchez, Johnston, & de Pablo, 1998) (Fernandez-Nieves, Fernandez-Barbero, Vincent, & de las Nieves, 2001) (Shah, Holmes, Johnston, & Korgel, 2002) or sparsely packed ligands (Patel & Egorov, 2007) to apply. It is clear from the density profiles (Figure 3.8 and Figure 3.9) that the ligand region is not penetrated by the solvent. The passivated surface in this case is much harder and smoother than it would be in case of a polymer brush and the solvent only interacts with the ligand *tips*. Further, the onset of interfacial repulsion occurs *before* ligands can overlap. Repulsion is, to use standard terminology (Fernandez-Nieves, Fernandez-Barbero, Vincent, & de las Nieves, 2001) osmotic and not elastic.

3.4.3 Contribution to $\mathcal{W}$

The linearity of ρ_{pore} *vs.*$1/L$ plots in Figure 3.2 and Figure 3.3 implies that the density profile in the slit pore can be approximated by a step function whose value is ρ_{bulk} at $z>l_o$ and $z<L-l_o$ and zero elsewhere. Here l_o is a measure of the thickness of the passivating layer. Since the solvent density profile is fairly uniform across the pore and can be adequately approximated by a step function, it makes sense to try to use a simple model by which to better understand the contributions to $\mathcal{W}$ for the two systems. Such a model was developed in the previous chapter. We consider $\mathcal{W}$ to be composed of 3 types of contributions: W_{vac} (due to direct interaction between ligands on opposite faces), W_{self} (contribution due to solvent cohesive interaction with its own bulk) and W_{wall} (contribution due to solvent interaction with the walls). Of these, we already know W_{vac} from our simulations in vacuum. W_{wall} is the difference in

wall-fluid interaction free energy when the gap-width is very large and when the gap-width is some finite value of *L* and we need a route to estimate it. If $u_{fw}(z')$ is the interaction free energy of a single solvent molecule at a distance *z'* from a ligand-passivated wall, then:

$$W_{wall}(L) = A_{pore}\rho_{bulk}\int_{l_o}^{L-l_l}\left[u_{fw}(z') + u_{fw}(L-z')\right]dz' - 2A_{pore}\rho_{bulk}\int_{l_o}^{\infty}u_{fw}(z')dz' \qquad \text{... (3.9)}$$

The procedure to obtain a characteristic u_{fw} from a density functional theory and the solvent density profile at wide-gap pores is described in detail in the last chapter. These are displayed in Figure 3.11.

3.4.4 Effect of Electrostatics

To illustrate the effect of electrostatic interactions, we have run wide-gap simulations ($L=100Å$) for perfluorodecanethiol and perfluorooctanethiol slit pores with the charges on *F* atoms being replaced with the charges on H atoms of dodecanethiol. The charge on attached C atoms is adjusted accordingly while keeping all other things unchanged. We will call these the H-charged ligands (with a charge on 0.06e on each F) as opposed to the fully charged or F-charged ligands (with a charge of between -0.17 and -0.12 on each F). From the density profile, we have obtained the u_{fw} for each case (Figure 3.11). The well-depth of the wall-solvent interaction for H-charged and F-charged perfluorodecanethiol ligands is approximately the same but that for the the F-charged ligand has the greater range – due to the stronger electrostatic nature of the interaction. The effect of charge on u_{fw} is different for the two types of ligands because of difference in their structure at the ligand-solvent interface. The perfluorodecanethiol ligands are longer and hence the density of their tips at the ligand-solvent interface is lower. The negative charges on the fluorine on F-charged perfluorodecanethiol repel the negatively charged oxygen atoms of CO_2 reducing the CO_2 molecule attractive dispersion interactions in the hollows formed between neighbouring ligand-tips at the ligand-solvent interface. The finding, from first principles calculations, that binding-energies of CO_2 with short-chain (C1, C2) hydrocarbon clusters is stronger than that between CO_2 and short chain fluorocarbon clusters (Diep, Jordan, Johnson, &

Beckman, 1998) is consistent with this. For the shorter perfluorooctanethiol ligands, where the hollows at the ligand-solvent interface are spatially shallower due to denser packing of the ligand tips, one expects that the CO_2 molecules are in any case unable to benefit from enhanced dispersion interactions. Hence the well depth with the H-charged ligands is shallower than the electrostatically enhanced depth with the F-charged ligands. A calculation (not shown) with a *planar* surface passivated by F-charged and H-charged perfluorooctanethiol and solvated by CO_2 also enhanced attraction with F-charges – consistent with the argument just given.

The effect of electrostatics is demonstrated in Figure 3.12 where the difference in the $W_{vac}+W_{wall}$ values between the *H-charged* and *F-charged* ligands is plotted (H-charged value is subtracted from the F-charged value). It is clear that without the electrostatic interactions with quadrupole of CO_2, the fluorocarbon ligands would not have been as effective – they would have attracted each other more strongly and attracted CO_2 more weakly. The subtle advantage of the electrostatic interactions is (as seen from Figure 3.11) that they extend the *range* of attractive interaction of the wall with the solvent – making it that much more difficult to dislodge the solvent from the pore.

3.4.5 Reasons for Effectiveness of Fluorocarbons in CO_2

From our analysis, we can point out three reasons for the greater effectiveness of the fluorocarbon ligands over the hydrocarbon ligands:

1. Higher C-F bond dipole moment compared to C-H bond dipole moment allows fluorocarbons ligands to interact more strongly with quadrupole of CO_2 making them more CO_2 philic. Further, the *range* of interaction with solvent also increases – allowing osmotic repulsion to become significant at wider gap-widths or particle separations.
2. The unique geometry of fluoroalkanes (see Figure 3.13) where the positive charges are buried in a “shell” of negative charges ensures that the fluorocarbons always present an *adverse* dipole to themselves. This auto-repulsion results in a weaker ligand-ligand attractive interaction. The

Figure 3.13 also illustrates that there is a disadvantage of having a ligand with a strongly dipolar group which may not always be adversely oriented to groups from the other wall. The ability to reorient adverse dipoles is a possible reason why polyethyleneglycol based ligands (Fan, McLeod, Enick, & Roberts, 2006) are not effective capping ligands in $ScCO_2$.

3. An additional subtle advantage of the fluorine group is that the packing density of the perfluorocarbons (~20Å^2/ligand) is significantly lower than that of the hydrocarbons (~16Å^2/ligand (Shah, Husain, Johnston, & Korgel, 2002)) owing to the fact that fluorocarbons, with a molecular cross section of 28.3Å^2 (Kirsch, 2004), are fatter than the corresponding hydrocarbon whose molecular cross section is 18.9Å^2 (Fenter, Eisenberger, Li, Camillone III, Bernasek, & Scoles, 1991). Hence the dispersion interactions of fluorocarbon ligands with those on the opposing walls are weaker than with n-dodecanethiol ligands.

It is well known that the best stabilizations of colloidal systems are achieved when the colloids have a high affinity for the solvent and a low affinity for themselves (Israelachvilli, 1992) (Louis, Allahyarov, Lowen, & Roth, 2002) (Rabani & Egorov, 2002). Hence the fluorocarbons behave like "ideal" in these respects. The "mix" of geometry, electrostatics and dispersion interactions for fluoroalkanes all favour them over hydrocarbons for CO_2 solvent. The CO_2-philicity can be explained entirely on basis of electrostatic and dispersion interactions – precluding the need to postulate a "special" interaction between CO_2 and fluorocarbons. The significance of electrostatic interaction to the enhanced CO_2-philicity of the fluorocarbons is the subject of some controversy with some groups finding no significant electrostatic interactions between CO_2 and fluorocarbon (Costa Gomes & Padua, 2003) (Yee, Fulton, & Smith, 1992) and attributing enhanced solubility of CO_2 in fluorocarbons to the relative ease with which cavities form in fluorocarbon fluids due to lowered cohesive energy density (which, as we have seen, is itself significantly due to electrostatics). Other groups claim a significantly stronger interaction between CO_2 and fluorocarbons which is attributed to electrostatics (Cece, Jureller, Kerschner, & Moschner,

1996) and “site-specific” interactions have been invoked (Dardin, DeSimone, & Samulski, 1998). The controversy can be somewhat resolved by noting that electrostatics (a) play a rather unimportant role in the properties of bulk fluorocarbon fluids (Song, Rossky, & Maroncelli, 2003) and (b) have their effect masked, at short range, by the dispersion interactions. Hence calculations/measurements in bulk fluids or between pairs of molecules need not reveal the effect of electrostatics in a heterogeneous environment. However, in case of a heterogenous system which is also extended, the effect due to the addition of the relatively slowly decaying electrostatic interactions can play a much more significant role.

3.4.6 Explanation of experimental observations on alternative ligands

The various attributes of perfluorocarbons mentioned above also appear to account for the success of fluoroacrylate-based polymeric surfactants in stabilizing dispersions of organic liquids in $ScCO_2$ (DeSimone & Wells, 2001). The non-fluorous CO_2 philic functional groups that have been proposed in the literature incorporate either the oxygenated functional groups such as ethers (Fan, McLeod, Enick, & Roberts, 2006), carbonates (Sarbu, Styranec, & Beckman, 2000) and sugars (Potluri, Xu, Enick, Beckman, & Hamiltion, 2002) or stubby hydrocarbons incorporating tertiary alkanes (Fan, McLeod, Enick, & Roberts, 2006) (Anand, Bell, Fan, Enick, & Roberts, 2006). Of these only the last have seen some limited success as ligands for nanoparticle emulsions in $ScCO_2$. These we will deal with in the next chapter.

The failure of the oxygenates to be effective nanoparticle ligands is probably due to their flexibility and hence ability to reorient to convert an adverse dipole to a favourable one – resulting in stronger direct attractive interactions between particles (see cartoon in Figure 3.13). The various ligands have been selected/characterised on basis of cloud-point measurements i.e. their behavior as free ligands in bulk CO_2. However, the behavior of ligands restricted to a surface is quite different from their behavior in bulk liquid and this point must be noted when screening ligands.

3.5 Conclusion

In this chapter we have examined the reasons that perfluoroalkane ligands as much better at stabilizing ligand passivated nanoparticle dispersions in $ScCO_2$ than are the hydrocarbon ligands. We determined that the reason for this effectiveness was the C-F dipole moment which interacts with the quadrupole of CO_2, along with a peculiar structure of fluoroalkanes that ensure that the C-F dipoles of two fluoroalkane molecules are always adverse, in addition to a relatively weak dispersive interactions of the fluorocarbons with each other due to sparser packing on the nanoparticle surfaces. All of these make surfaces passivated by pefluoroalkanes simultaneously CO_2-philic and less auto-philic. The insights obtained from this analysis can be used as design guides for non-fluorous ligands effective in $ScCO_2$.

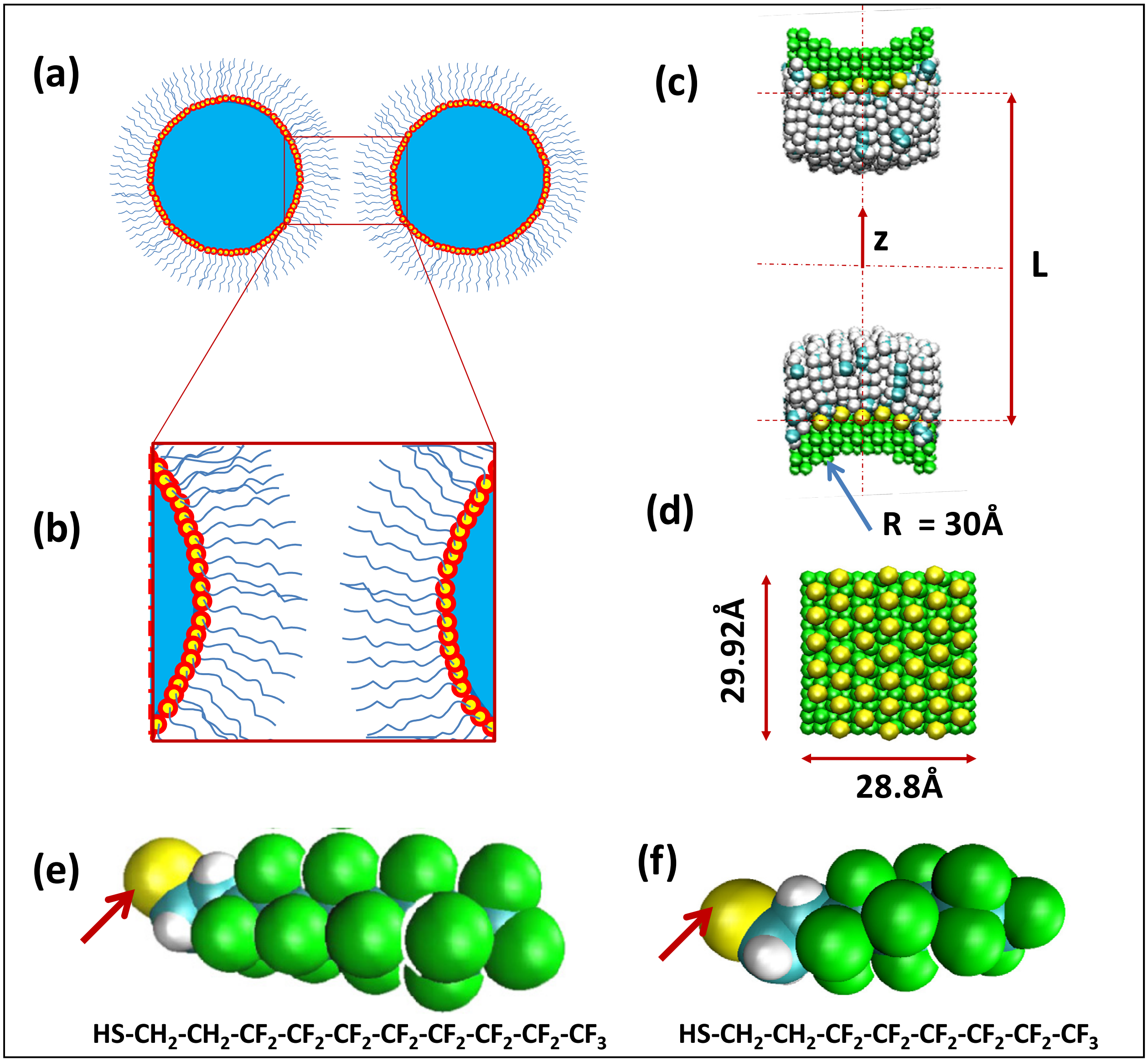

Figure 3.1: The simulation setup. (a) Schematic of a pair of ligand passivated nanoparticles in a solvent the interactions between which are modified by the passivating ligands. To simulate a pair of sufficiently diluted nanoparticles of the experimentally interesting diameter of ~60Å would require a particle number of the order of 100,000. However, (b) comparable insight may be obtained at much lower computational cost of <10,000 particles by examination of a slit-pore with bumpy walls, a periodic image of which is shown schematically. (c) The same system set-up for molecular dynamic simulations is visualized using VMD (Humphrey, Dalke, & Schulten, 1996). The ligands are perfluorodecanehiol ($C_{10}H_4F_{17}SH$) with the terminal-S group shown in yellow. (d) The distribution of roots, shown by yellow S atoms, on a single plate is shown. The ligand-root density is ~20Å^2/ligand and lattice spacing is 4.8 Å. (e) Space-filling model of perfluorodecanethiol (thiol H not shown) and its chemical formula. Sulfur root indicated by arrow. (f) Same for perfluorooctanethiol.

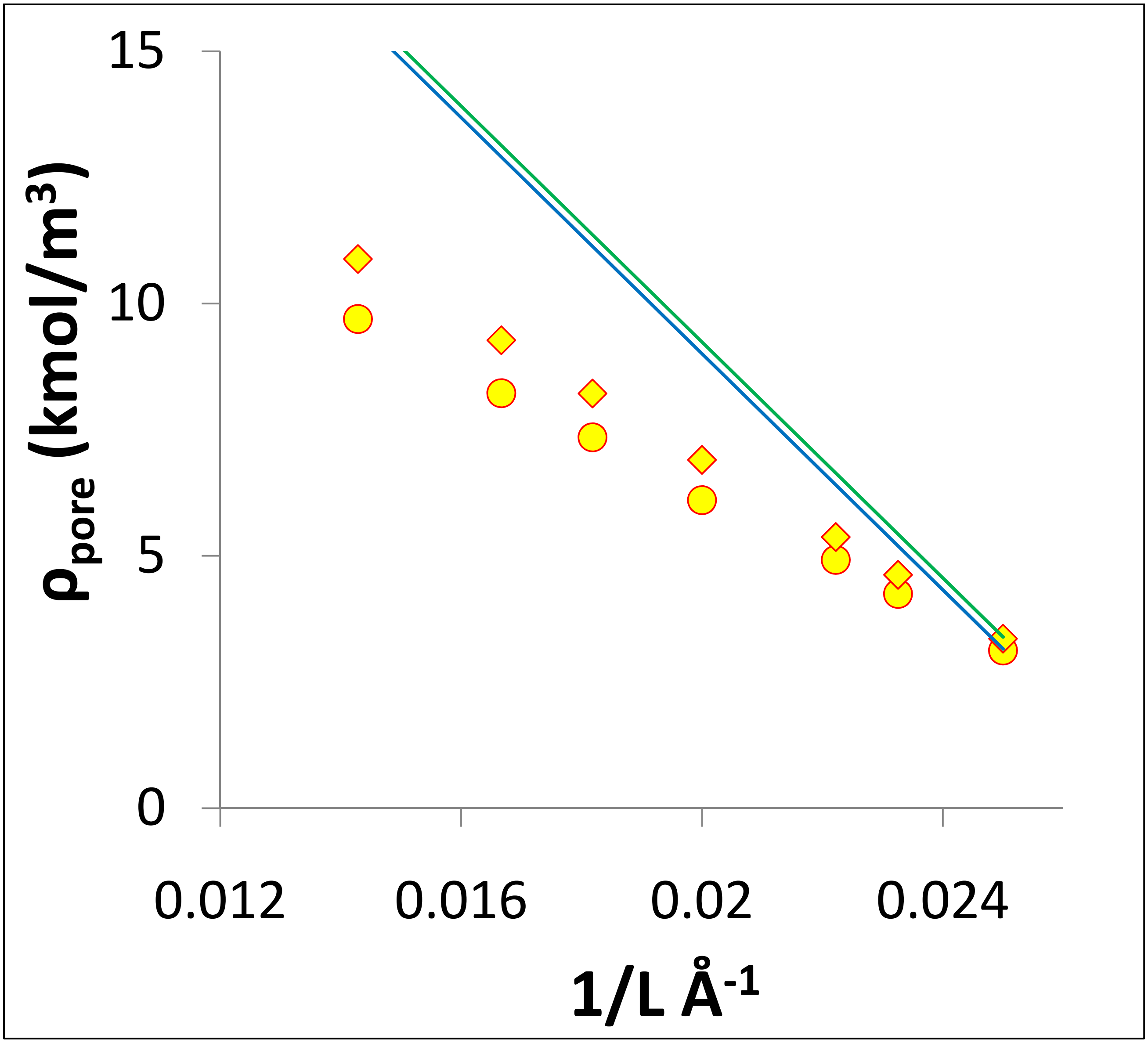

Figure 3.2: Plot of ρ_{pore} vs. 1/L for perfluorodecanethiol passivated slit pore with CO_2 as solvent. The symbols are the result of solutions of equation 3.6 while the solid lines are the straight line fits through them (see equation 3.7). Two bulk pressures are represented with P_{bulk}=*150 atm (*○*)* and P_{bulk}=*300 atm (*◇*).* The error bars for the fit are less than size of the symbols.

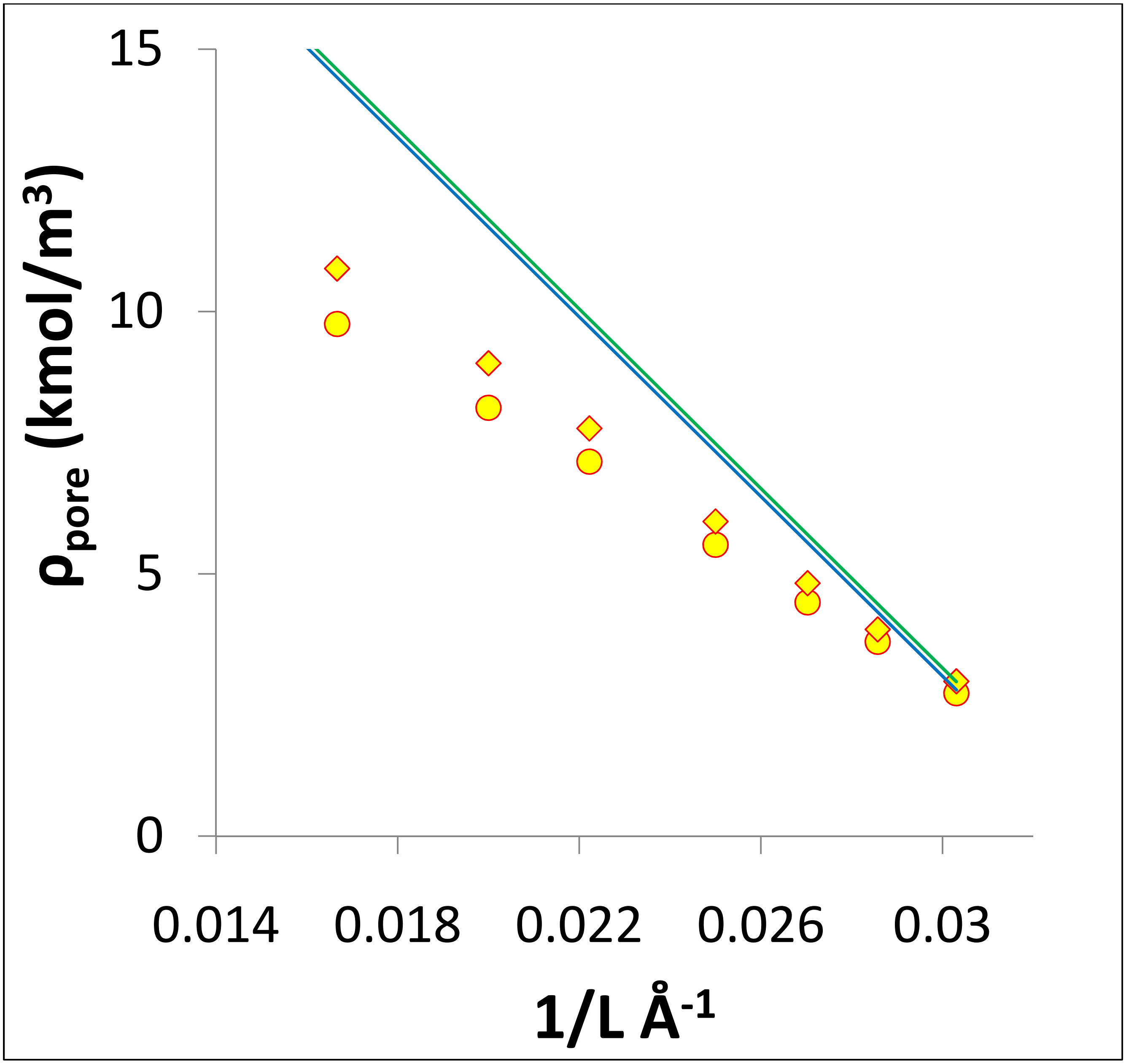

Figure 3.3: Plot of ρ_{pore} vs. 1/L for perfluorooctanethiol passivated slit pore with CO_2 as solvent. The symbols are the result of solutions of equation 3.6 while the solid lines are the straight line fits through them (see equation 3.7). Two bulk pressures are represented with P_{bulk}*=150 atm (* ○ *)* and P_{bulk}*=300 atm (* ◇ *).* The error bars for the fit are less than size of the symbols.

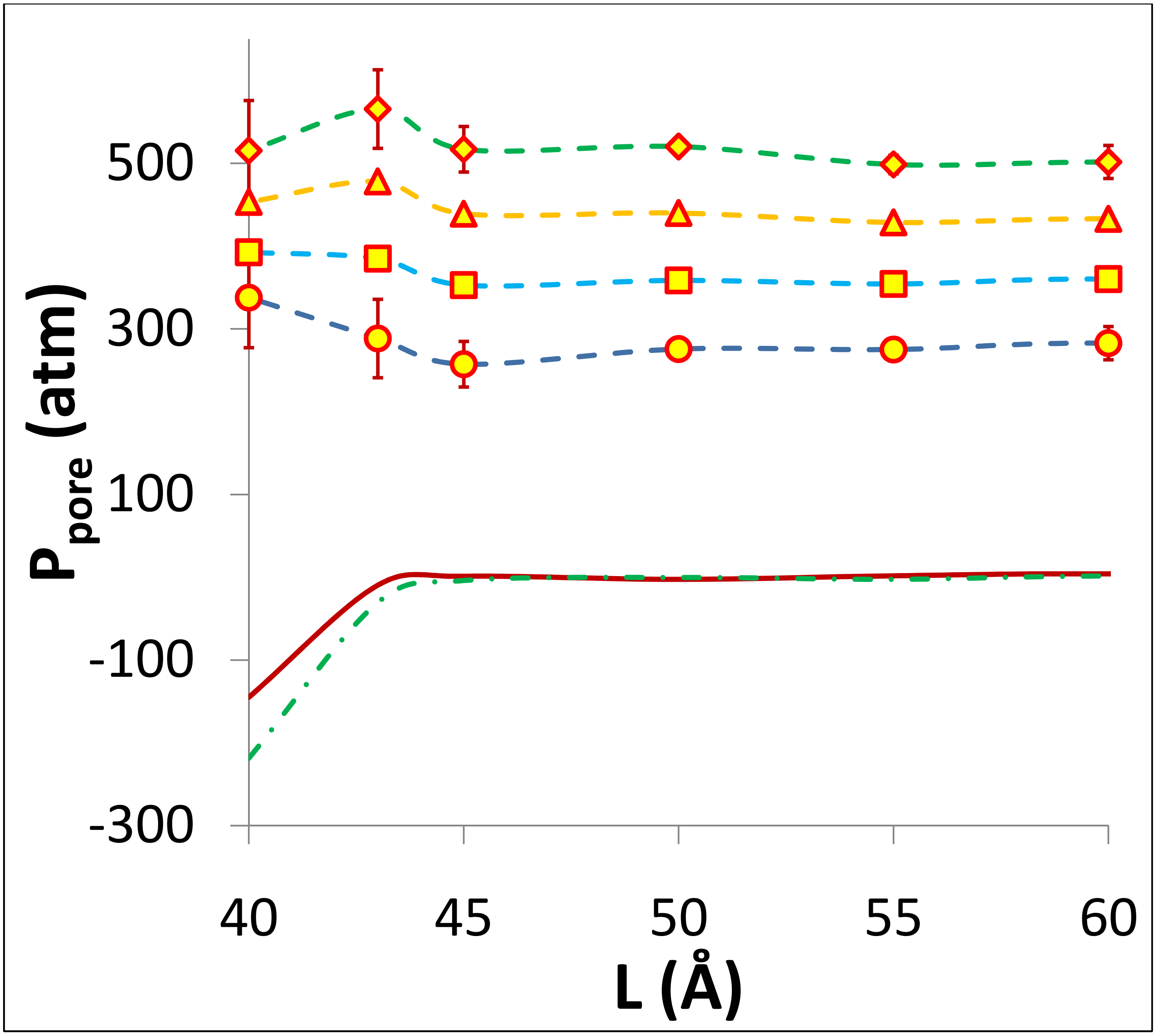

Figure 3.4: Plot of P_{pore} *vs. 1/L* calculated using the procedure described in section 3.3 for perfluorodecanethiol passivated pores solvated by CO_2 for various values of bulk pressures. The symbols are the result of said calculation for various values of *L* while the broken lines are meant to guide the eye. The four bulk pressures represented are $P_{bulk}=150$ *atm* (○), *Pbulk=200atm* (□), *Pbulk=250atm* (△) and $P_{bulk}=300$ *atm* (◇). The solid line (▬▬▬)is the corresponding curve for interactions in vacuum and the dotted and dashed line (▬ ▪ ▬) corresponds to interaction in vacuum if the F atoms had the same charge as the H atoms of n-dodecanethiol. For clarity, only error bars for $P_{bulk}=150$ *atm* and $P_{bulk}=300atm$ are shown. The error bars for the other pressures are similar. Interactions for *L<33Å* are strongly repulsive (high P_{pore}) and the corresponding values are not shown.

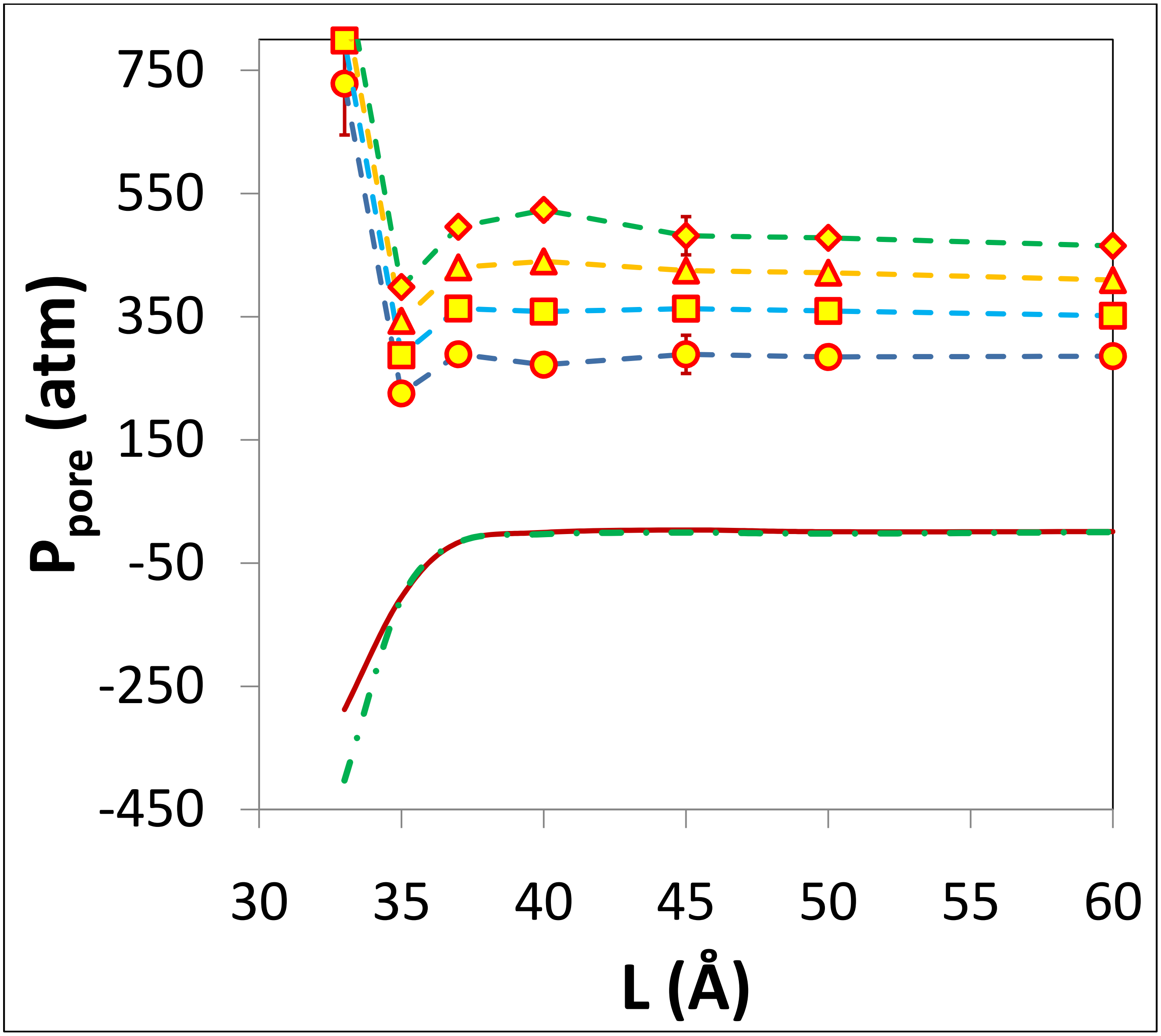

Figure 3.5: Plot of P_{pore} *vs. 1/L* calculated using the procedure described in section 3.3 for perfluorooctanethiol passivated pores solvated by CO$_2$ for various values of bulk pressures. The symbols are the result of the calculation for various values of *L* while the broken lines are meant to guide the eye. The four bulk pressures represented are $P_{bulk}=150$ *atm* (○), *Pbulk=200atm* (□), *Pbulk=250atm* (△) and $P_{bulk}=300$ *atm* (◇). The solid line (━━━━)is the corresponding curve for interactions in vacuum and the dotted and dashed line (▬ ▪ ▬) corresponds to interaction in vacuum if the F atoms had the same charge as the H atoms of n-dodecanethiol. For clarity, only error bars for $P_{bulk}=150$ *atm* and $P_{bulk}=300$*atm* are shown. The error bars for the other pressures are similar. Interactions for *L<33Å* are strongly repulsive (high P_{pore}) and the corresponding values are not shown.

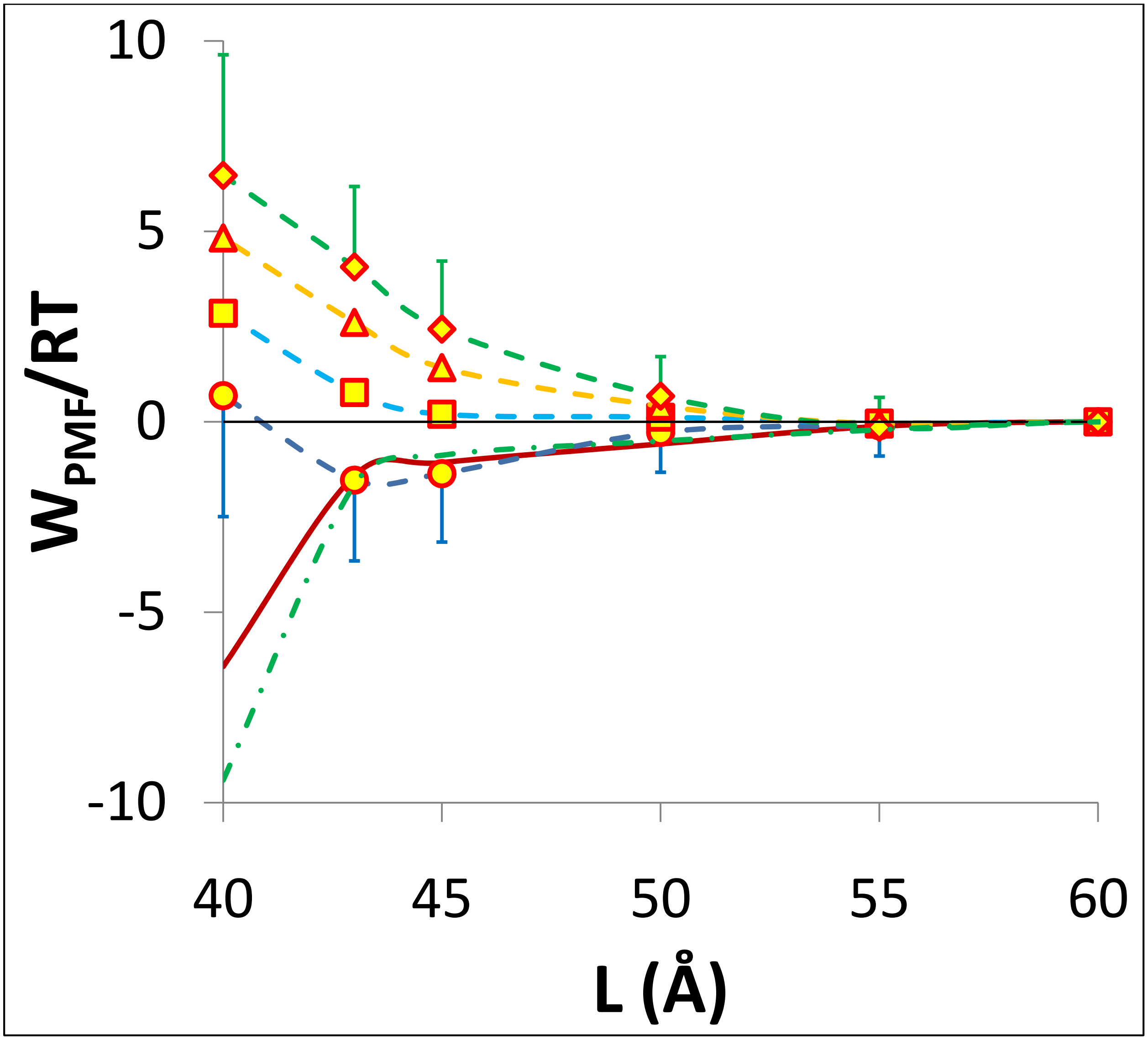

Figure 3.6: Potential of mean force of the slit-pore for perfluorodecanethiol passivated slit pores solvated by CO_2 at various pressures is calculated using equation 3.2 as shown in section 3.3. For the calculation P_{bulk}^{eff} is calculated using $L_{trunc}=60Å$ (see equation 3.3). The free energy corresponding to a single periodic image is attributed to a pair of particles to calculate the free energy per mole. The symbols are the result of said calculation for various values of *L* while the broken lines are meant to guide the eye. The four bulk pressures represented are $P_{bulk}=150$ *atm* (○), *Pbulk=200atm* (□), *Pbulk=250atm* (△) and $P_{bulk}=300$ *atm* (◇). The solid line (▬▬▬)is the corresponding curve for interactions in vacuum and the dotted and dashed line (▬ ▪ ▬) corresponds to interaction in vacuum if the F atoms had the same charge as the H atoms of n-dodecanethiol. For clarity, only lower error bars for $P_{bulk}=150$ *atm* and lower error bars for $P_{bulk}=300$*atm* are shown.

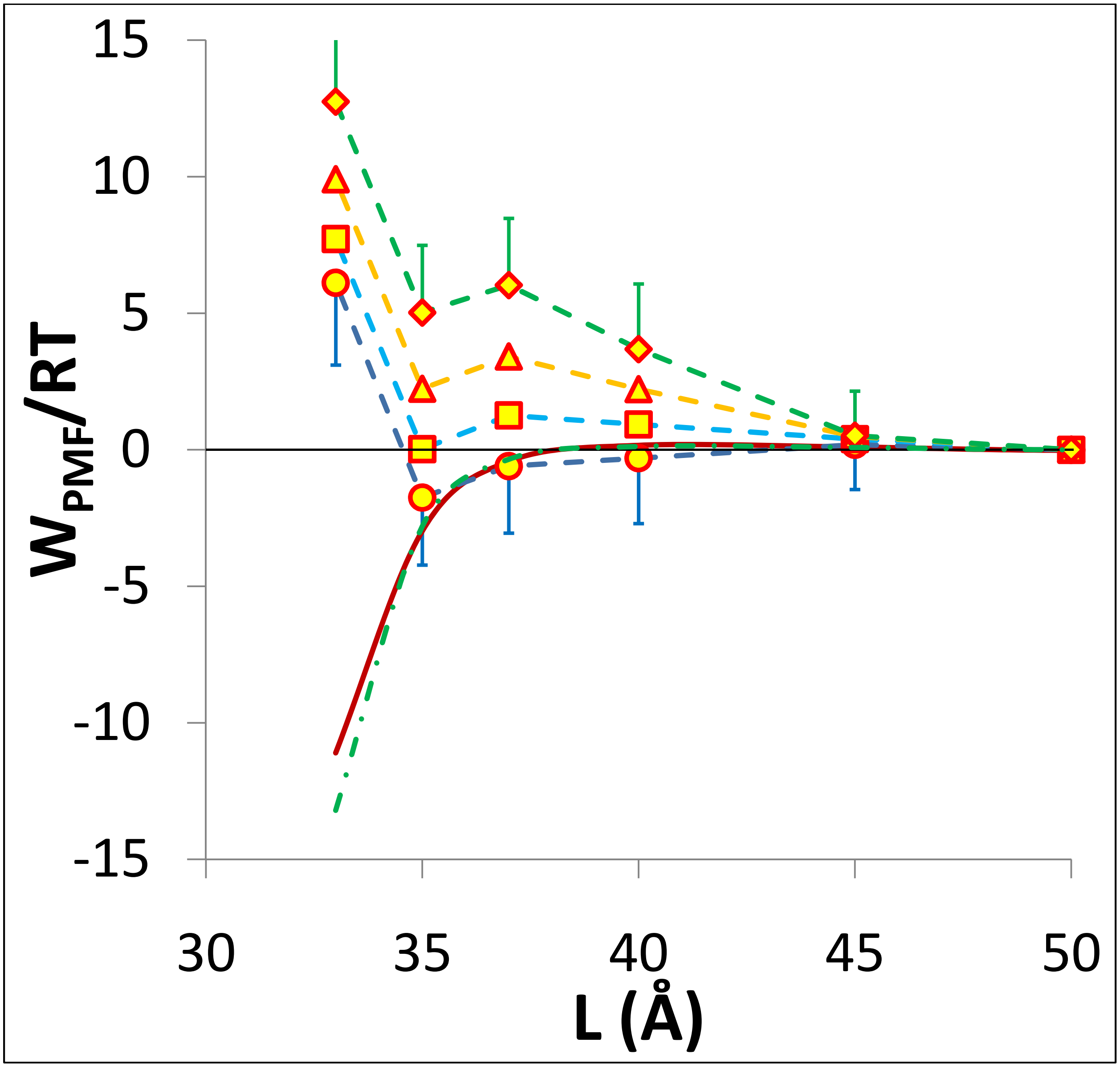

Figure 3.7: Potential of mean force of the slit-pore for perfluorodecanethiol passivated slit pores solvated by CO_2 at various pressures is calculated using equation 3.2 as shown in section 3.3. For the calculation P_{bulk}^{eff} is calculated using L_{trunc}=50Å (see equation 3.3). The free energy corresponding to a single periodic image is attributed to a pair of particles to calculate the free energy per mole. The symbols are the result of said calculation for various values of *L* while the broken lines are meant to guide the eye. The four bulk pressures represented are P_{bulk}*=150 atm* (○), *Pbulk=200atm* (□), *Pbulk=250atm* (△) and P_{bulk}*=300 atm* (◇). The solid line (▬▬)is the corresponding curve for interactions in vacuum and the dotted and dashed line (▬ ▪ ▬) corresponds to interaction in vacuum if the F atoms had the same charge as the H atoms of n-dodecanethiol. For clarity, only lower error bars for P_{bulk}*=150 atm* and only upper error bars for P_{bulk}*=300atm* are shown.

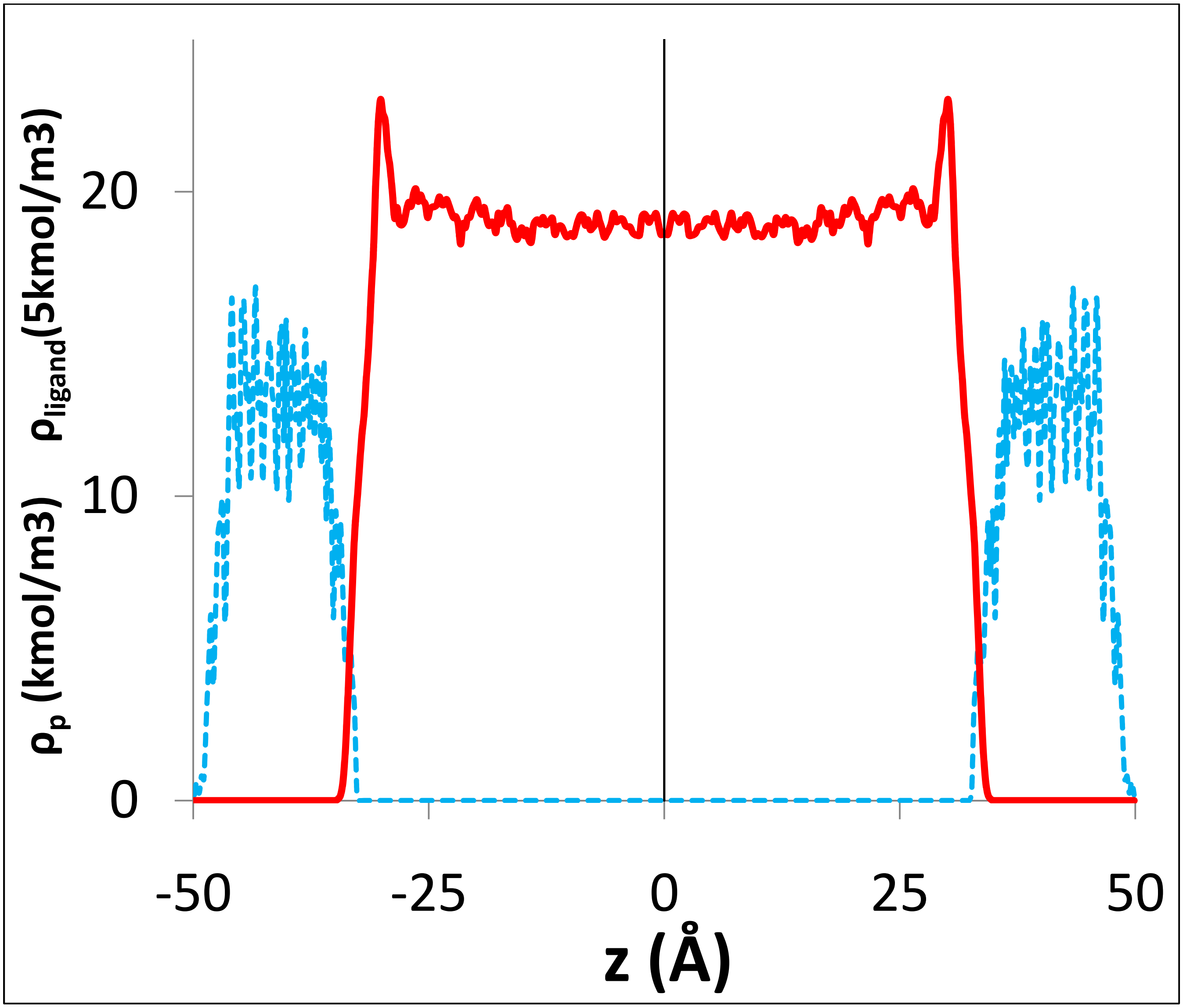

Figure 3.8: Density profile for a slit pore of gap-width $L=100Å$ passivated by perfluorodecanethiol ligands and solvated by CO_2 at a bulk pressure of $P_{bulk}=169\ atm$. The density profile of the C atoms of the ligand (ρ_{ligand}) is shown by the broken line (■ ■) while the solvent density profile ρ_p is the solid line (▬). The density profile is determined using the entire cross section of the periodic image of the slit pore.

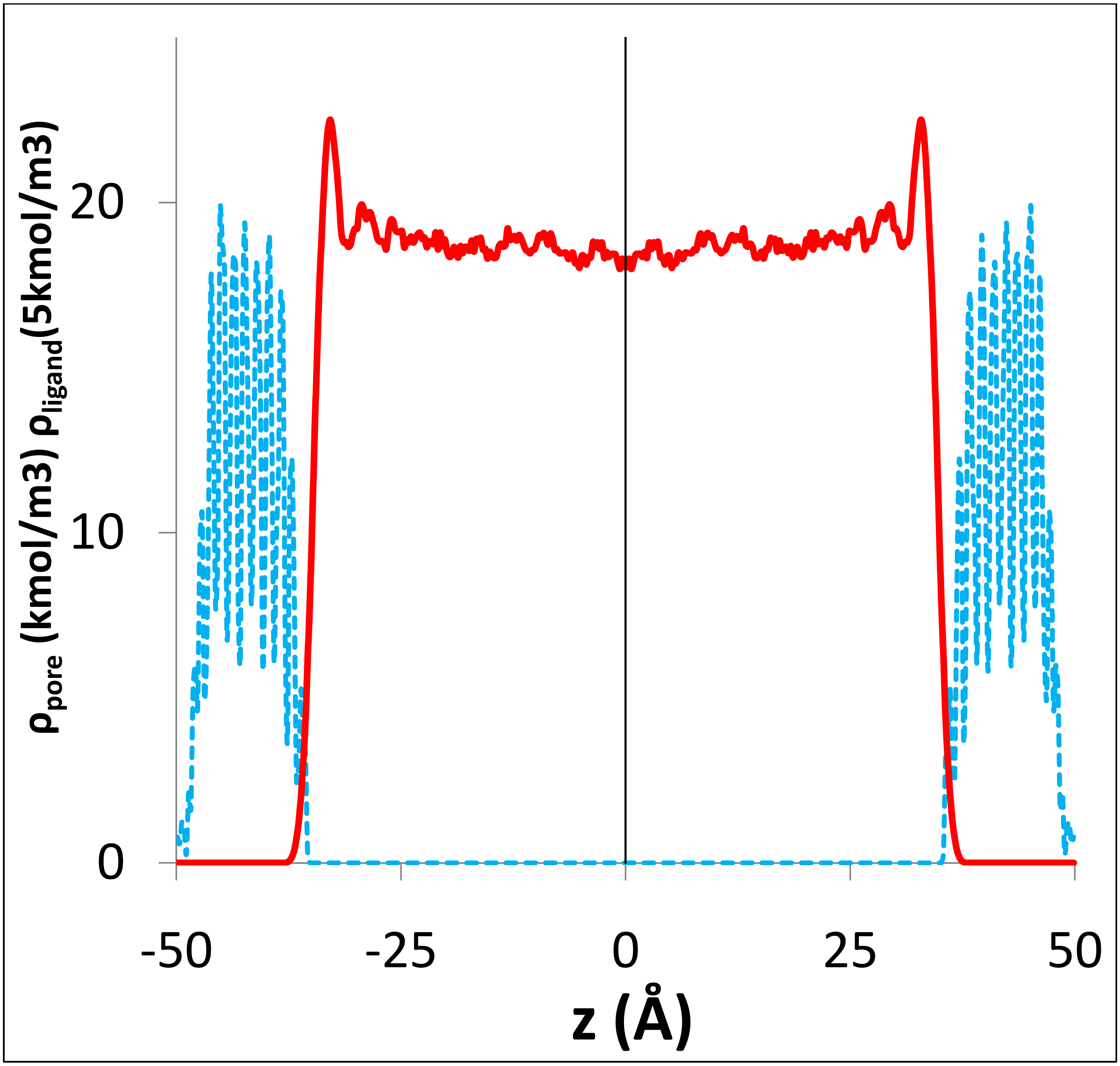

Figure 3.9: Density profile for a slit pore of gap-width *L=100Å* passivated by perfluorooctanethiol ligands and solvated by CO_2 at a bulk pressure of $P_{bulk}=155\ atm$. The density profile of the C atoms of the ligand (ρ_{ligand}) is shown by the broken line (■ ■) while the solvent density profile ρ_p is the solid line (▬). The density profile is determined using the entire cross section of the periodic image of the slit pore.

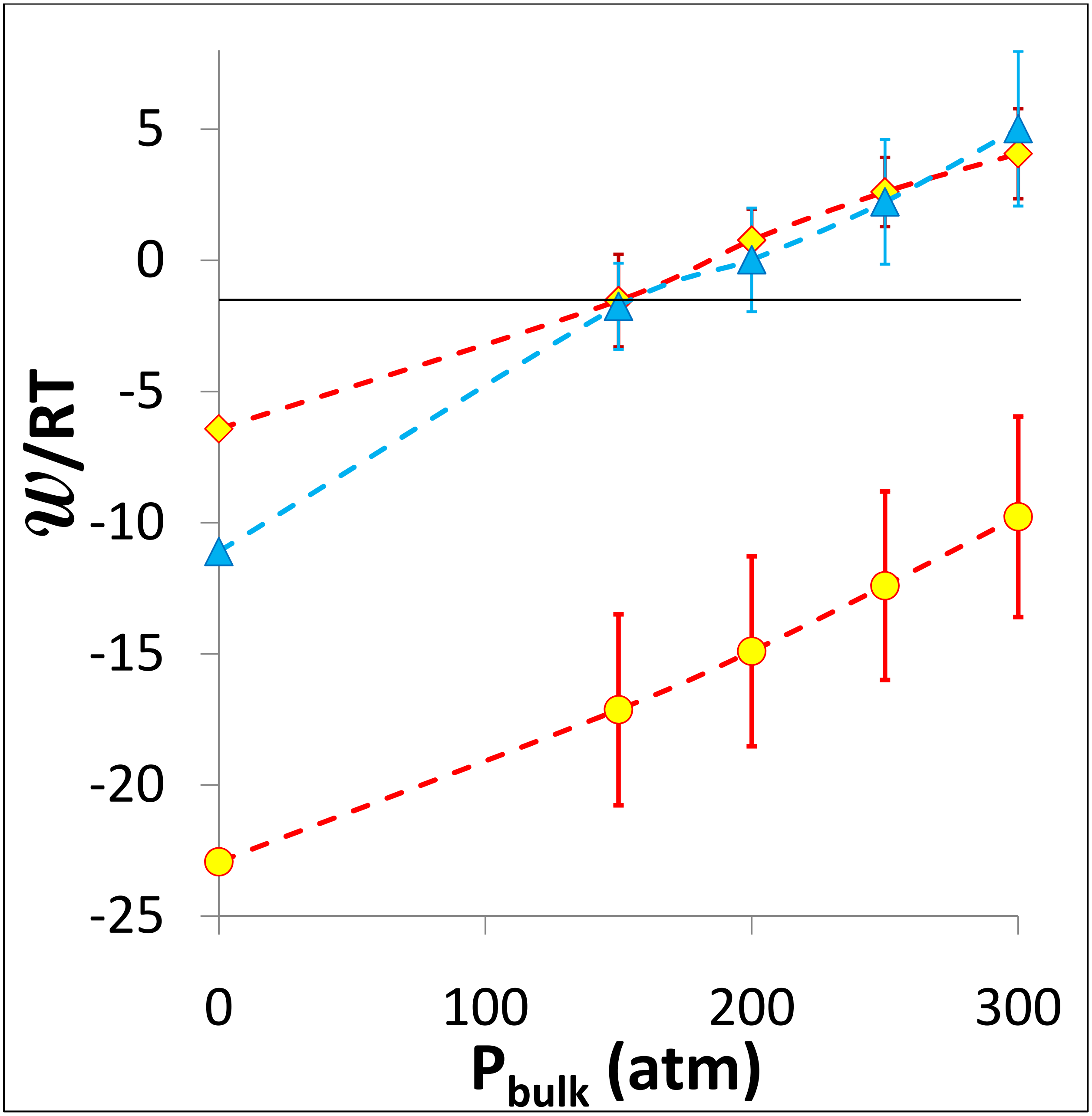

Figure 3.10: Plot of $\mathcal{W}$ vs. P_{bulk} for CO_2 solvated slit pores passivated by n-dodecanethiol *(* ● and *L_{eq}=43Å, $L_{eq\text{-}vac}$=43 Å),* perfluorodecanethiol (◆ and *L_{eq}=43Å, $L_{eq\text{-}vac}$=40 Å),* perfluorooctanethiol *(*▲ and *L_{eq}=35Å, $L_{eq\text{-}vac}$=33Å).* The interactions for a single periodic image are attributed to a single particle pair. The thin solid horizontal line corresponds to -1.5RT so that $\mathcal{W}$ values greater than this imply a thermodynamically stable dispersion. The dotted lines are guides to the eye.

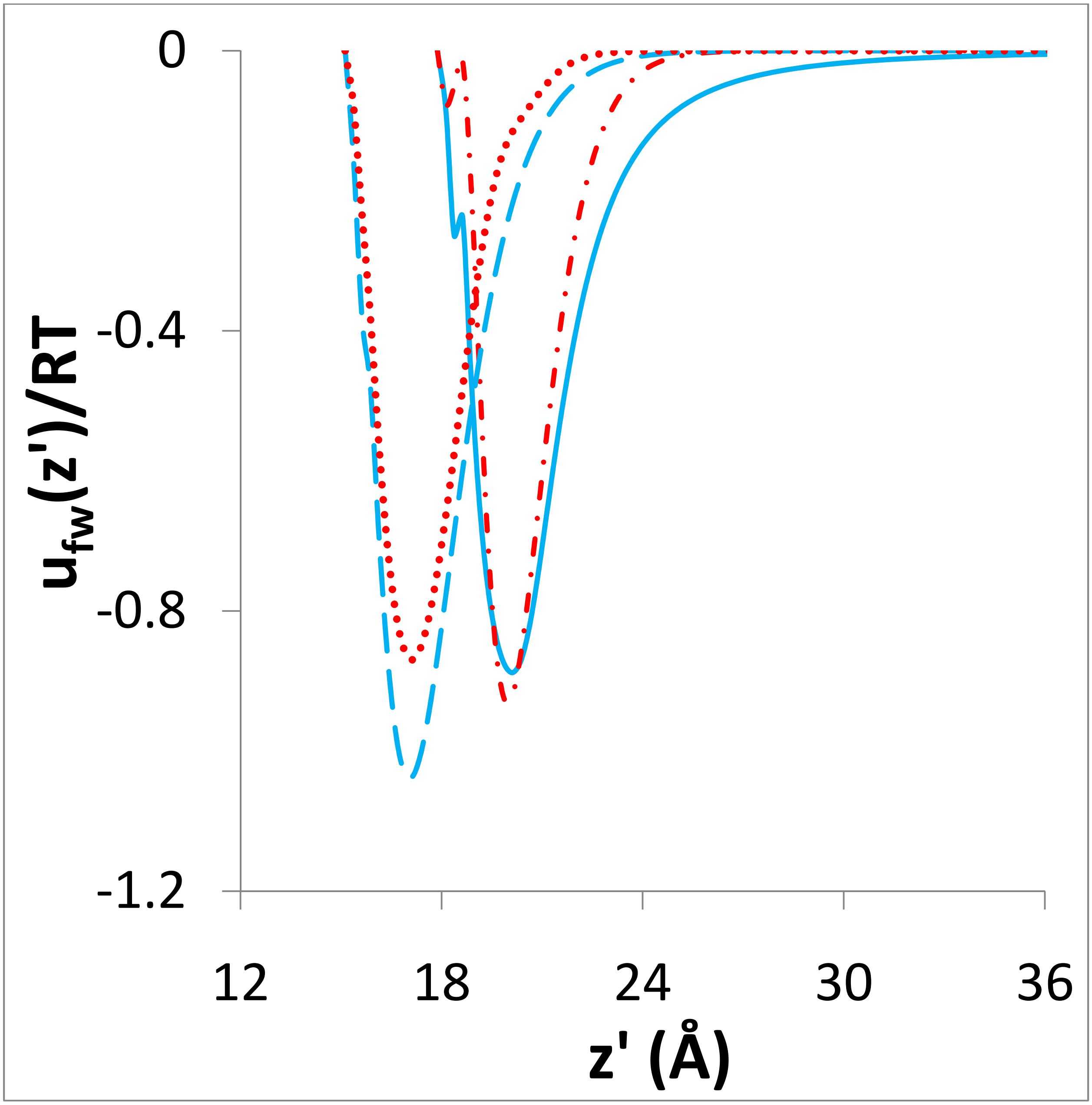

Figure 3.11: Wall-solvent interaction potential calculated using density profiles for wide slit pores (L=100Å). The solid line (———) is for perfluorodecanethiol, the dashed line (— — —) is for perfluorooctanethiol, the dotted-and-dashed line (— · —) is for perfluorodecanethiol with charges on F equal to those on H of dodecanethiol while the dotted line (• • • • • • • •)is the same for perfluorooctanethiol.

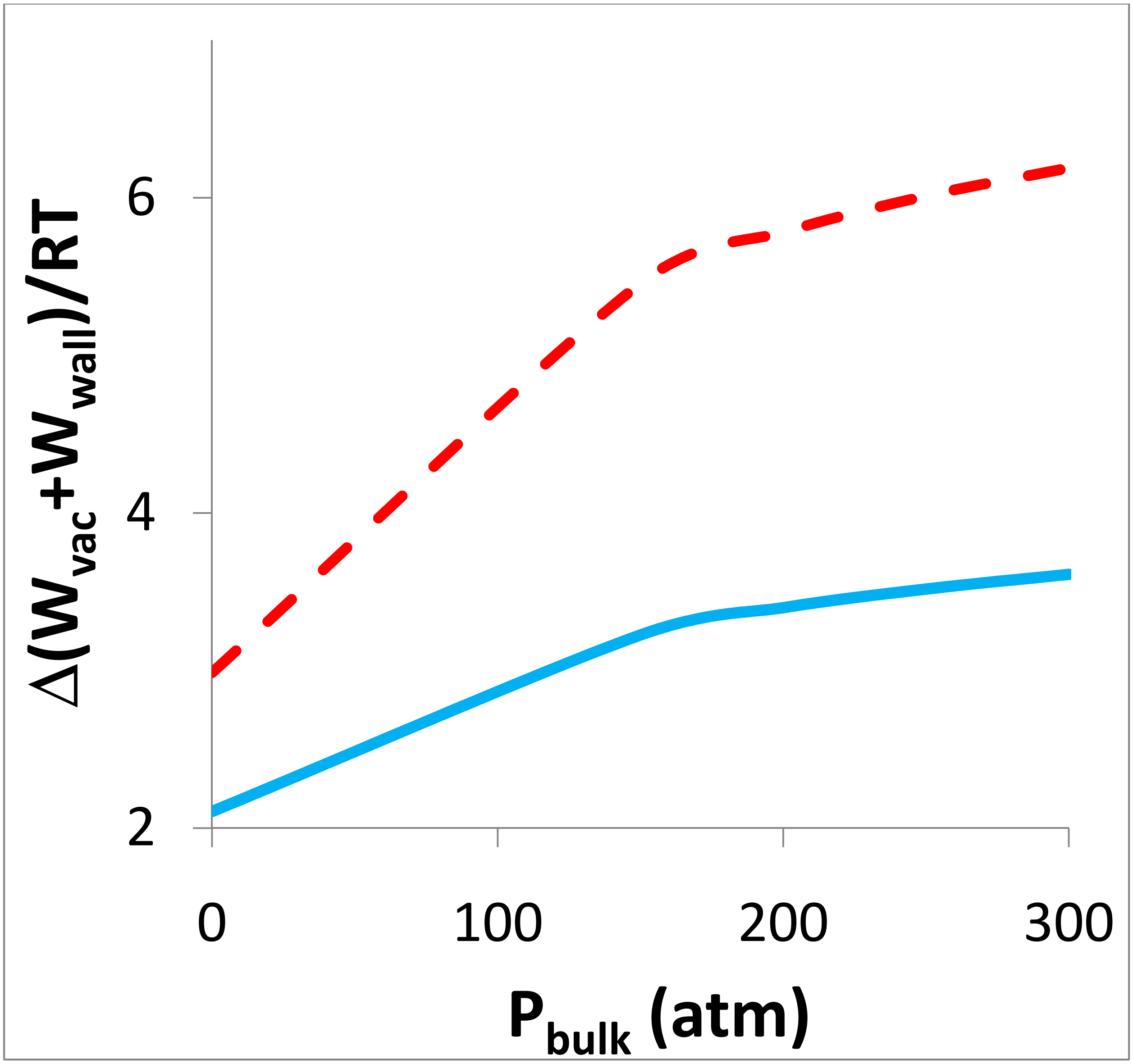

Figure 3.12: Plots illustrating effect of electrostatics. The solid line (▬▬▬▬) is the difference between W_{vac}+W_{wall} of the H-charged and F-charged perfluorooctanethiol ligand (L_{eq}=35Å, $L_{eq\text{-}vac}$=33Å); F-charged value minus H-charged value. The broken line (▬ ▬ ▬) is the same quantity for perfluorodecanethiol ligands (L_{eq}=43Å, $L_{eq\text{-}vac}$=40Å).

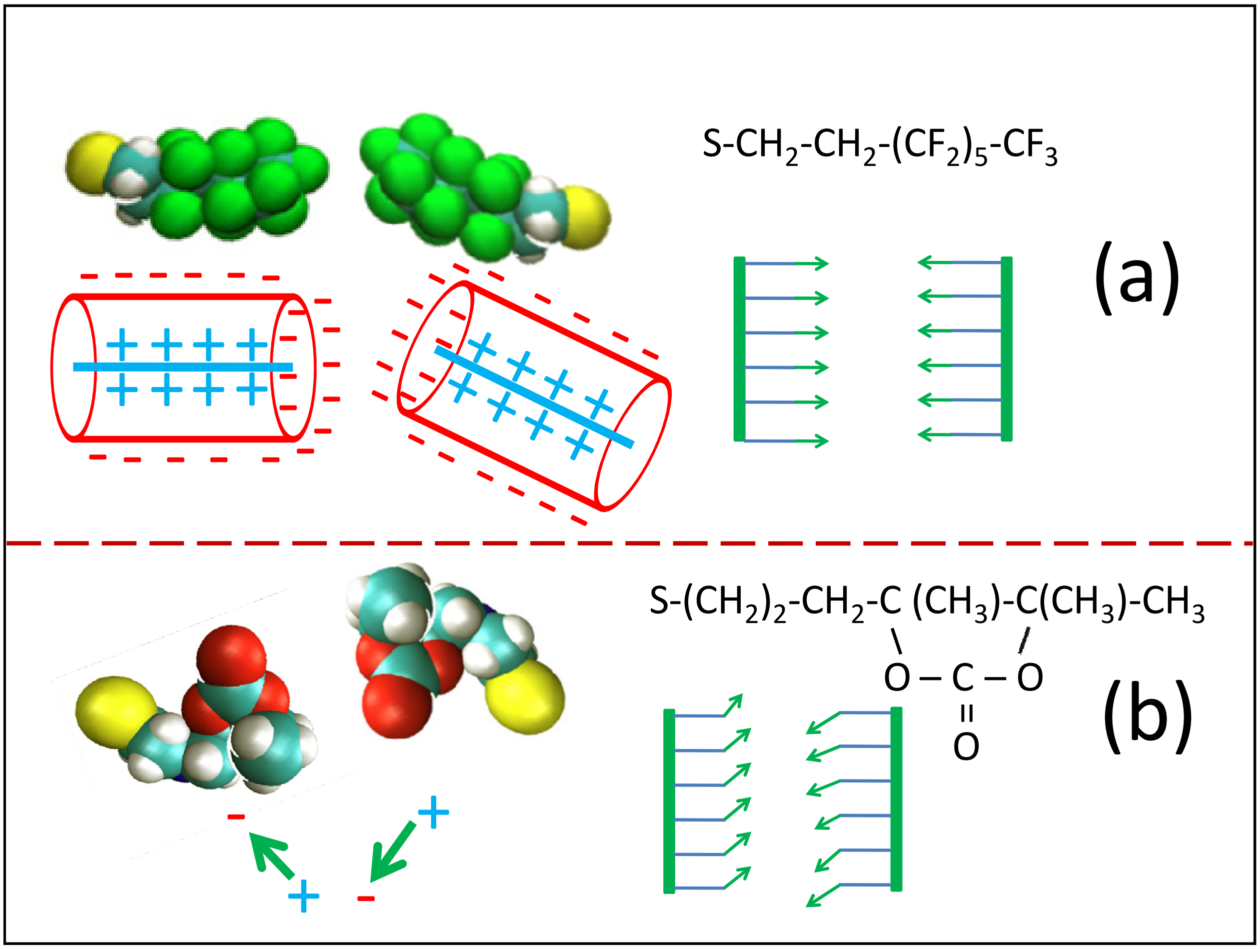

Figure 3.13: Space filling models and cartoons for (a) fluorocarbon ligand (perfluorooctanethiol) and (b) nonfluorous ligand with CO_2-philic carbonate functional group. It is readily apparent that the fluorocarbons cannot orient in such a way that the dipoles align favourably, whereas the carbonate groups can readily do so. Also, the attractive dispersive interactions due to the oxygenates are stronger than those due to fluorines. Hence two surfaces passivated by ligands carrying carbonate groups will attract each other *more* strongly than similarly packed surfaces passivated by fluorocarbons.

Chapter 4: Stubby Ligands for Nanoparticle Dispersions

4.1 Introduction

The facile control of solvation power of supercritical fluids (Shah, Holmes, Johnston, & Korgel, 2002) allows reversible control of colloidal dispersions in them which in turn enables more effective processing of nanoparticle dispersions (Murray, Norris, & Bawendi, 1993). Many nanoparticles of interest (metals, semiconductors) have high surface energies and tend to agglomerate. This must be avoided since the properties of many nanoparticles of interest are sensitively dependent on their size (Alivisatos, 1996) (Brust, Walker, Bethell, Schiffrin, & Whyman, 1994) (Murray, Norris, & Bawendi, 1993). To prevent agglomeration, their surfaces are passivated by covering them with "capping ligands" which are molecules with a "head" group that attaches strongly to the nanoparticle surface and which in turn is attached to a "tail" group composed of moieties that provide, at a minimum, steric repulsion to separate nanoparticle cores sufficiently to allow size dependent properties to manifest (Shah, Hanrath, Johnston, & Korgel, 2004) (Sun & Murray, 1999). If the tails are properly chosen, the resulting "ligand-passivated" nanoparticles can even form stable dispersions in fluid media.

Since supercritical CO_2 ($ScCO_2$) has numerous desirable properties as an industrial solvent, particularly non-flammability and non-toxicity, it is of considerable interest to develop a cheap, non-toxic ligand that is "effective" in supercritical CO_2; i.e., dispersions of such nanoparticles stable in supercritical CO_2 (Sarbu, Styranec, & Beckman, 2000)(Potluri, Xu, Enick, Beckman, & Hamiltion, 2002) (Anand, Bell, Fan, Enick, & Roberts, 2006). The problem is that cheap and benign ligands, like n-dodecanethiol, which have proven effective in organic liquids like toluene (Brust, Walker, Bethell, Schiffrin, & Whyman, 1994) and hexane (Shah, Holmes, Doty, Johnston, & Korgel, 2000) and even in supercritical fluids like ethane (Clarke, Waters, Johnson, Satherley, & Schiffrin, 2001)(Shah, Holmes, Johnston, & Korgel, 2002), have proven decidedly ineffective in supercritical CO_2 under comparable conditions (Shah, Holmes, Doty, Johnston, & Korgel, 2000). The ligands that have proven effective in $ScCO_2$ are perfluoroalkanes (Shah, Husain, Johnston, & Korgel, 2002) and perfluoropolyethers (Saunders & Korgel, 2004)) which form stable dispersions in $ScCO_2$ at convenient conditions of temperature (near ambient) and pressure (<500 bar) but these are expensive, practically xenobiotic (Resnati, 1993) and have degradation products which can be persistently toxic (Pelley, 2004).

In the previous two chapters we reported the results of our investigation by molecular simulations into the phenomena behind stability of ligand-passivated nanoparticle dispersions from which we hope to glean insights by which to guide experiments to develop cheap but effective ligands for nanoparticle dispersions in $ScCO_2$ (Sarbu, Styranec, & Beckman, 2000)(Potluri, Xu, Enick, Beckman, & Hamiltion, 2002) (Anand, Bell, Fan, Enick, & Roberts, 2006). Furthermore, the insights gained from this problem can be readily applied to understanding surfactants that form CO_2-water emulsions (da Rocha, Johnston, & Rossky, 2002)(Stone, da Rocha, Rossky, & Johnston, 2003) – pertinent to enhanced oil recovery(Rossen, 1996), biology (Johnston, et al., 1996)(Harrison, Goveas, Johnston, & O'Rear, 1994) "green" chemistry (DeSimon, 2002) (Sagisaka, et al., 2008) among other applications (Johnston & da Rocha, 2009).

We have reported in detail a method by which to investigate the pertinent physics via the use of readily available molecular simulation infrastructure. We have explained that hydrocarbon ligands (like n-dodecanethiol) are so effective in supercritical ethane but not on supercritical CO_2 principally because CO_2 is more autophilic than ethane. The autophilicity arises from quadrupolar interactions which are disrupted and not adequately compensated for by the ligand surface when the CO_2 is forced into the region between two hydrocarbon-ligand passivated nanoparticles, causing low resistance by CO_2 to expulsion from the gap between approaching nanoparticles.

In the third chapter, we explained why the fluorocarbon ligands are effective in $ScCO_2$. Fluorocarbons have a significant C-F dipole enabling them to effectively interact with the quadrupole of CO_2. At the same time, the geometry of the fluorocarbons is such that the dipole offered is always adverse to *each-other* and electrostatic interaction is repulsive. Also the fluorocarbons molecules are bulky and pack more sparsely at the nanoparticle surface, leading to weaker dispersion interactions between opposing surfaces that are passivated by fluorocarbon ligands.

We now turn our attention to “stubby” hydrocarbons i.e. hydrocarbons whose geometric coverage area per head group is relatively large and which have been thought to be good candidates as non-fluorous substitutes for fluorocarbons in emulsion contexts (da Rocha, Johnston, & Rossky, 2002) (Stone, da Rocha, Rossky, & Johnston, 2003) (Anand, Bell, Fan, Enick, & Roberts, 2006). To do so, we have taken the case of isostearic acid whose effectiveness as a ligand for silver nanoparticles in $ScCO_2$ has been gauged experimentally (Anand, Bell, Fan, Enick, & Roberts, 2006) and showed some improved effectiveness compared to straight chain alkanes. To explore the effect of “stubbiness”, we also consider a ligand, isotricosanoic acid, which is similar to isostearic acid except that one tail is longer than the corresponding tail in isostearic acid. This results in a sparser (less stubby) ligand-solvent interface and as the “stubbiness” criterion would predict, we will see that the ligand is less effective. However, more densely “over-packed” isostearic acid ligands turn out to be far less effective than either of the others. Hence we conclude that there is an optimum ligand density where stabilization is maximum and the packing density of isostearic-acid on silver seems to be in the vicinity of this optimum. This may also explain why certain very “stubby” ligands (Fan, McLeod, Enick, & Roberts, 2006) fail to be effective, as we will discuss. Hence it does not appear that *purely* hydrocarbon moieties can stabilize nanoparticle dispersions in $ScCO_2$.

This paper is organized as follows: The relevant experimental observations are summarized in Section 4.2, the simulation strategy and setup in Section 4.3 and the results are reported and discussed in Section 4.4.

4.2 Experimental Observations

The relevant experimental observations are as follows:

1. It is found that dodecanethiol-capped silver nanocrystals do not disperse in $ScCO_2$ even at very high pressures (> 300 atm). However they disperse if n-hexane is added as a co-solvent in substantial amounts (>50%v/v) (Shah, Holmes, Doty, Johnston, & Korgel, 2000). Further, CO_2 is actually found to be an *anti*-solvent for dodecanethiol passivated gold nanoparticles (Gupta, Shah, Zhang, Saunders, Korgen, & Johnston, 2005) as well as organic-polymeric nanoparticles dispersed in toluene (Chang, Lee, & Lin, 2007), (Dixon, Johnston, & Bodmeier, 2004).
2. Silver nanoparticles were synthesized in $ScCO_2$ (at 22^oC and 276 bar) in the presence of isostearic acid ligand (a branched hydrocarbon). Of the particles synthesized, a fraction (23%) comprising the smaller particles (average diameter 26Å with most probable diameter of 17Å) formed a stable dispersion. The dispersed fraction and average diameter of dispersed particles could be increased by adding cyclohexane as co-solvent. The dispersed particles could be redispersed after precipitation (Anand, Bell, Fan, Enick, & Roberts, 2006).
3. Stubby hydrocarbon thiols (e.g. 4-t-butylbenzenethiol and t-nonylmercaptan (Fan, McLeod, Enick, & Roberts, 2006)) proved ineffective in stabilizing silver nanoparticle emulsions in $ScCO_2$ at 40^0C and 282 atm *in-spite* of very high ligand solubilities in $ScCO_2$.

4.3 Simulation Strategy and Computational Details

We will reproduce briefly the method as presented in the previous chapters. Our goal is to gain an insight into the physical phenomena that occur in the solvent region between two ligand-passivated spheres. This region is marked in Figure 4.1a. To considerably save on computations at acceptable cost to physical insight, we use a *slit-pore* with “bumpy” walls where the radius of curvature of the bumps is the same as that of the hypothetical nanoparticle surface (seeFigure 4.1b). This size we have taken to be *60Å* diameter to facilitate comparison with our earlier results. The setup is shown for isostearicacid ligands in Figure 4.1c. The system consists of 536 silver atoms that are approximated by LJ particles. They are arranged in an FCC lattice to form two plates each of which is three atomic layers thick. The ligand roots (acid O-atoms) are distributed on the inner surface of the opposing bumpy plates as shown in Figure 4.1d. The dimensions of the periodic system along the along the face of the plates i.e. along the *x*- and *y*- directions are 28.8Å by 29.92Å respectively. The system is periodic in these directions but is not periodic in the *z*-direction. Gapwidth *L* is taken as the z-direction separation between the nearest silver atoms of the opposite plates. The ligands’ molecular structures are shown in Figure 4.1e (for isostearic acid) and Figure 4.1f (for isotricosanoic acid). The simulation package used is DL_POLY 2.15 (Smith & Forester, 2003) and visualization is done using VMD (Humphrey, Dalke, & Schulten, 1996). The force field used is OPLS-AA (Jorgensen, 2002) except for carbon-dioxide (modeled using the EPM2 model (Harris & Yung, 1995)) and Ag whose LJ parameters are calculated from those that approximate long range attractive interaction between Xe (Berry, Rice, & Ross, 2000) and Ag(111) obtained from ab-initio calculations (Vidali, Ihm, Kim, & Cole, 1991) (Gatica, Li, Trasca, Cole, & Diehl, 2008). Essentially the same molecular models are used to investigate surfactant behavior at water-CO_2 interfaces (da Rocha, Johnston, & Rossky, 2002) (Stone, da Rocha, Rossky, & Johnston, 2003).

The ligand packing density on the nanoparticle surface is obtained indirectly. We could not find any literature values for the packing density, so we calculated the *potential* (not free) *energy* change when an isostearic acid ligand molecule was removed from a planar surface passivated with that ligand with different surface densities. The packing density for which this change was zero is the one we chose for the simulations. Since the acid group binds to silver much less tightly than a thiol group does (Cohen-Atiya & Mandler, 2003), this yields a reasonable estimate of the packing density. The packing density is therefore 31.2Å^2/ligand which in a hexagonal close packing implies a lattice spacing of 6.0Å (Figure 4.1d).

Effectiveness is quantified using the *free energy of flocculation* $\mathcal{W}$ as a metric. $\mathcal{W}$ is calculated using the procedure described in detail in chapter 1. We will quickly reproduce the salient points here:

$$\mathcal{W}(P_{bulk}) = W_{PMF}(\xi_{bulk}, L_{eq}) \quad \text{... (4.1)}$$

where ξ_{bulk} is the bulk activity (externally imposed parameter), W_{PMF} is the potential of mean force of solvated interactions in the slit-pore, L_{eq} is the gap-width at equilibrium and P_{bulk} is the nominal bulk pressure corresponding to ξ_{bulk}. W_{PMF} is given by:

$$W_{PMF}(\xi_{bulk}, L) = \int_{L_{trunc}}^{L} \left[P_{pore}(\xi_{bulk}, L') - P_{bulk}^{eff}(\xi_{bulk})\right] A_{pore}\, dL' \quad \text{... (4.2)}$$

where L_{trunc} is the gap-width at which $P_{pore}(\xi_{bulk}, L)$. P_{pore} is the normal pressure in the pore at the given activity and gap-width L and it does not vary with L. A_{pore} is the cross-sectional area in the pore. $P_{bulk}^{eff}(\xi_{bulk})$ is given by:

$$P_{bulk}^{eff}(\xi_{bulk}) = \text{average}\left\{P_{pore}(\xi_{bulk}, L) : L \geq L_{trunc}\right\} \quad \text{... (4.3)}$$

From a series of canonical ensemble simulations (Frenkel & Smit, 2002) for fixed L and varying pore density ($\rho_{pore}=N_{pore}/A_{pore}/L$ where N_{pore} is the number of solvent molecules in a single periodic image of the pore), the isothermal equation of state for gap-width L can be fitted to the following van der Waals form. This form is obtained from an analytical treatment of planar slit pores. It involves an assumption of a flat density profile in the pore (Schoen & Diestler, 1998):

$$P_{pore}\left(\rho_{pore}, L\right) = a_0 + \frac{\rho_{pore} RT}{1 - a_1 \rho_{pore}} + a_2 \rho_{pore} + a_3 \rho_{pore}^2 \qquad \text{… (4.4)}$$

Here, R is the universal gas constant and a_0, a_1, a_2 and a_3 are the parameters to be fitted independently for each L. An apparent advantage of this approach is that the fit pressure appears to suppress the effect of random errors at individual state points on consequent results. Using a number of configurational snapshots from the canonical ensemble simulations, excess chemical potential in the pore (μ_{pore}^{ex}) is calculated employing Widom insertions (Widom, 1963) (Frenkel & Smit, 2002). These can be fitted to the following form (Schoen & Diestler, 1998):

$$\beta\mu_{pore}^{ex}\left(\rho_{pore}, L\right) = a_{\mu 0} - \ln\left(1 - \rho_{pore} a_{\mu 1}\right) + \frac{\rho_{pore} a_{\mu 1}}{1 - \rho_{pore} a_{\mu 1}} + a_{\mu 2} \rho_{pore} \qquad \text{… (4.5a)}$$

Here $\beta = \left(RT\right)^{-1}$ and $a_{\mu 0}$, $a_{\mu 1}$, $a_{\mu 2}$ are parameters to be fitted independently for each L. The excess chemical potential is related to the activity by the simple relation:

$$\xi_{pore}\left(\rho_{pore}, L\right) = \rho_{pore} \exp\left(\beta\mu_{pore}^{ex}\right) \qquad \text{… (4.5b)}$$

By solving the following equation we can get the value of pore density at a given L and ξ_{bulk}:

$$\xi_{pore}\left(\rho_{pore}, L\right) = \xi_{bulk} \qquad \text{… (4.6)}$$

We find that for a fixed ξ_{bulk} the pore density values fit the following simple form:

$$\rho_{pore}^{fit}\left(\xi_{bulk}, L\right) = \rho_{bulk}\left(\xi_{bulk}\right)\left(1 - \frac{2l_o}{L}\right) \qquad \text{… (4.7)}$$

where ρ_{bulk} is the bulk density corresponding to ξ_{bulk} and *l*l_o is a constant. We use these values of $\rho_{pore}^{fit}(\xi_{bulk}, L)$ with equation 4.4 to get P_{pore} values for equations 4.2 and 4.3. P_{bulk} is obtained from ρ_{bulk} and a equation of state that is calculated separately employing the molecular model of the solvent. The bulk data is then fitted to the following two-parameter form (Schoen & Diestler, 1998):

$$P_{bulk} = \frac{RT\rho_{builk}}{1-\rho_{bulk}b} - a_{bulk}\rho_{bulk}^2 \qquad \text{… (4.8a)}$$

$$b = \frac{2}{3}\pi\sigma_f^3 \text{ and } a_{bulk} = \frac{16\pi}{9}\sigma_f^3\varepsilon_f \qquad \text{… (4.8b)}$$

Where σ_f and ε_f are fluid-specific constants that must be obtained by fitting equation 4.8 to the equation of state. The physical interpretation of the constants is that ε_f is the attractive energy parameter of the fluid particles while σ_f is the diameter of their core. The details of the simulations are described in the previous chapter. We have obtained values of W_{PMF} and $\mathcal{W}$ corresponding to P_{bulk}*=150, 200, 250* and *300* atm.

4.4 Results and Discussion

The ρ_{pore} *vs. 1/L* plots for both types of passivation (Figure 4.2 and Figure 4.3) in CO_2 solvated pores at $P_{bulk}>150atm$ are linear. Using the methods described in Section 4.3, P_{pore} *vs. L* curves for different values of P_{bulk} are calculated for CO_2 solvated pore passivated by isostearic acid (31Å^2/ligand, Figure 4.4) and isotricosanoic acid (31Å^2/ligand, Figure 4.5) so that, using equation 4.2, we get W_{PMF} *vs. L* plots for various values of P_{bulk} (see Figure 4.6 and Figure 4.7) respectively. Density profiles in a large gap (L=100Å) slit pore for both solvent and ligand appear in Figure 4.8 and Figure 4.9 for isostearic acid and isotricosanoic acid passivated pores respectively. Setting $L_{eq}=33Å$ ($L_{eq\text{-}vac}=30Å$) for isostearic acid passivated pore and $L_{eq}=42Å$ ($L_{eq\text{-}vac}=40Å$) for perfluorooctanethiol passivated pore, we get from equation 4.1, the $\mathcal{W}$ *vs.* P_{bulk} plots seen in Figure 4.10. In the absence of solvent, equilibrium occurs at $L_{eq\text{-}vac}$ and for $L<L_{eq\text{-}vac}$, the overlap of ligand regions causes large repulsive interactions. Upon fitting the equation of state to the form of equation 4.8 we get parameters for CO_2 ($\varepsilon_f = 0.807\text{kcal/mol}$, $\sigma_f = 2.9\overset{\circ}{\text{A}}$).

We will first validate our results against experimental observations. Then we will use a simple interpretive model to interpret the results followed by a discussion on hydrocarbon ligands.

4.4.1 Consistency with Experimental Observations

It is quite apparent from Figure 4.10 that the systems are much better stabilized by the two-tailed ligands than by the n-dodecanethiol ligands, which is as expected from literature. However, neither ligand is effective enough to boost $\mathcal{W}$ of the 60Å diameter particles to dispersion stability i.e. $\mathcal{W}$ higher than $-1.5RT$. One expects that the attractive interaction potential between spheres increases super-linearly with the sphere diameter (Fernandez-Nieves, Fernandez-Barbero, Vincent, & de las Nieves, 2001). Hence we can, using *linear* scaling and current values, estimate the *lower-bound* for $\mathcal{W}$ for a 15Å diameter pair of spheres passivated by isostearic acid. The results is shown in Figure 4.10. This barely clears the -1.5RT line indicating that the smaller spheres should indeed be stabilized in a dispersion – consistent with the observations reported (see section 4.2).

4.4.2 Contributions to $\mathcal{W}$

The linearity of ρ_{pore} *vs.1/L* plots in Figure 4.2 and Figure 4.3 implies that the density profile in the slit pore can be approximated by a step function whose value is ρ_{bulk} at $z>l_o$ and $z<L-l_o$ and zero elsewhere. Hence l_o is a measure of the thickness of the passivating layer. The solvent density profile, which is fairly uniform across the pore, can be adequately approximated by a step function. Hence, it makes sense to try to develop a simple model by which to gain insight into the contributions to $\mathcal{W}$ for the two systems. We consider 3 contributions to $\mathcal{W}$: W_{vac} (due to direct interaction between ligands on opposite faces), W_{self} (contribution due to solvent cohesive interaction with its own bulk) and W_{wall} (contribution due to solvent interaction with the walls). We already know W_{vac} from our simulations in vacuum. W_{wall} is the difference in wall-fluid interaction free energy when the gap-width is very large and when the gap-width is some finite value of *L* and we need a route to estimate it. Now, if $u_{fw}(z')$ is the interaction free energy of a single solvent molecule at a distance *z'* from a ligand-passivated wall, then:

$$W_{wall}(L) = A_{pore}\rho_{bulk}\int_{l_o}^{L-l_l}\left[u_{fw}(z') + u_{fw}(L-z')\right]dz' - 2A_{pore}\rho_{bulk}\int_{l_o}^{\infty}u_{fw}(z')dz' \qquad \text{… (4.9)}$$

The procedure to obtain u_{fw} from solvent density profile at wide-gap pores is described in detail in the second chapter. These are displayed in Figure 4.11.

4.4.3 Isostearic Thiol

It was found that even though "stubby" thiols like 4-t-butylbenzenethiol and t-nonylmercaptan (Fan, McLeod, Enick, & Roberts, 2006)) are very soluble in ScCO$_2$, they prove ineffective in stabilizing silver nanoparticle emulsions in ScCO$_2$ at 40^{0}C and 282 atm. Since a thiol (-SH) group binds to metal much more strongly than does an acid (–COOH) group (Cohen-Atiya & Mandler, 2003), the isostearic acid ligand with the acid group replaced by thiol (called isostearic thiol) should pack much more densely. In

Figure 4.11 we have shown the wall-solvent interaction potential for a passivation layer composed of isostearic-thiol packed with a surface density, equal to fluorocarbons', of 20Å^2/ligand, much denser than the 31Å^2/ligand of isostearic acid. The curve was obtained from the simulated density profile of CO_2 in a slit pore with L=100Å. This enables us to estimate W_{wall}. W_{vac} was calculated by a series of simulations with the thiol, but without solvent, at different L. In the chart inset in Figure 4.11 we have shown $W_{vac}+W_{wall}$ vs. L for the various ligands at $P_{bulk}=300$atm. Comparing these curves with Figure 4.10, we can see that they crudely track ligand effectiveness. Hence the fact that the $W_{vac}+W_{wall}$ vs. L curve for isostearic-thiol ligand is similar to the curve corresponding to dodecanethiol ligands clearly shows that the increased affinity of the densely packed ligands for each other is not offset by the increased osmotic repulsion by the solvent. This is consistent with the ineffectiveness of the various CO_2-soluble thiol ligands investigated by Fan et al (2006) (Fan, McLeod, Enick, & Roberts, 2006).

4.4.4 "Stubbiness" does not correlate with effectiveness

Hydrocarbons whose passivation layers present very low interfacial void regions have been thought to be good candidates as non-fluorous substitutes for fluorocarbons (da Rocha, Johnston, & Rossky, 2002) (Stone, da Rocha, Rossky, & Johnston, 2003) (Anand, Bell, Fan, Enick, & Roberts, 2006). This reasoning came from studies on surfactants at a water-CO_2 interface where the ligands are not rigidly bound, and was meant to explain the greater effectiveness of the *fluorocarbons* over the hydrocarbon ligands in the emulsion context. From our simulations on fluorocarbon ligands (see chapter 3) we have demonstrated that the effectiveness of fluorocarbon ligands as passivating ligands is due to a number of factors including electrostatics and geometry. It is clear that the n-dodecanethiol ligands as well as the two-tailed stubbly ligands are so densely packed that the interfacial free volume available to CO_2 in both cases is essentially zero. Also, from the calculations with the less "stubby" isotricoanoic acid ligands and the very "stubby" isostearic-thiol ligands, it is clear that there exists an *optimum* packing density of ligands when direct interaction between the ligands is offset by osmotic repulsion set up in the pore. Hence “stubbiness” does not correlate directly with effectiveness.

4.4.5 Ligand Design

It appears that ligands composed solely of aliphatic moieties cannot effectively disperse any but the smallest nanoparticles in $ScCO_2$ at the temperatures and pressures of interest. However, trimethylsiloxane surfactants have been reported to be effective in stabilizing dispersions of water droplets in CO_2 (da Rocha, Dickson, Cho, Rossky, & Johnston, 2003). This is probably due to the siloxy ($-OSiR_3$ where R= $-CH_3$) group that these ligands are tipped with. Oxygen is the most electronegative atom after fluorine and imparts a considerable dipole moment to the O-Si bond. The dipole interaction with the CO_2 quadrupole serves to increase the interfacial repulsion in confinement as CO_2 resists being ejected.

4.5 Conclusion

We investigated the reasons behind the partial effectiveness of “stubby” ligands in stabilizing dispersions of nanoparticles in ScCO$_2$ using isostearic acid analogues as the model. We discovered that for hydrocarbon moieties there is an optimum packing density where the ligand is most effective, balancing dispersion interactions between particles with surface-solvent interactions. It appears that the packing density of isostearic acid is near that optimum. Increasing the packing density by using stubby thiolated ligands or decreasing it at the ligand-solvent interface by lengthening a tail both result in lower stabilizations. Consequently, it does not seem likely that a ligand composed solely of aliphatic moieties would be effective in CO$_2$. Incorporation of oxygen in the ligand tips e.g. using alkoxy/siloxy tipped ligands is a more promising direction.

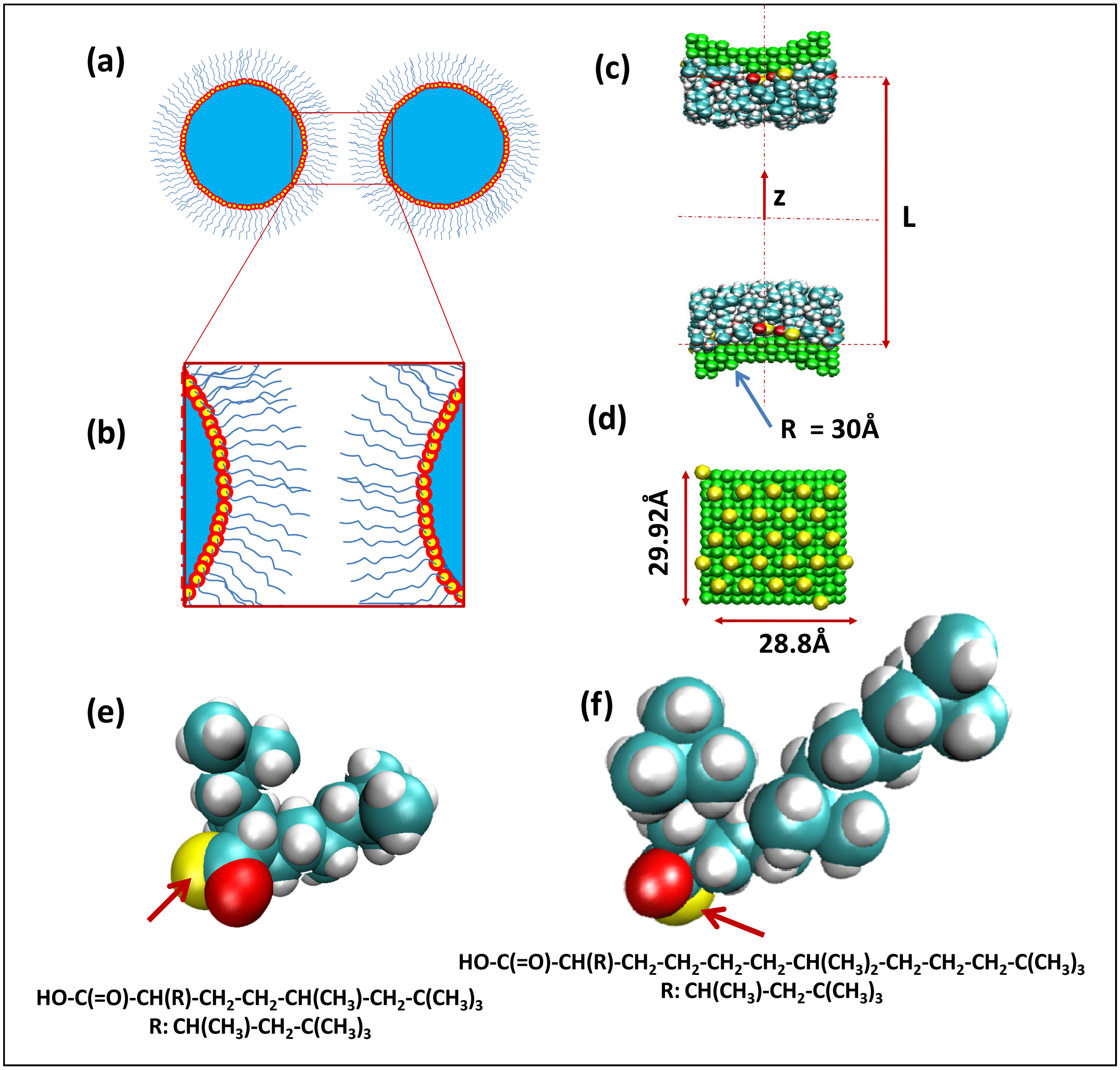

Figure 4.1: The simulation setup. (a) Schematic of a pair of ligand passivated nanoparticles in a solvent the interactions between which are modified by the passivating ligands. To simulate a pair of sufficiently diluted nanoparticles of diameter ~60Å would require a particle number of the order of 100,000. However, (b) comparable insight may be obtained at much lower computational cost (~10,000 particles) by examination of a slit-pore with bumpy walls, a periodic image of which is shown schematically. (c) The same system set-up for MD simulations is visualized using VMD (Humphrey, Dalke, & Schulten, 1996). The ligands are shown are isostearic acid with the terminal-O group shown in yellow. (d) The distribution of roots (shown by yellow O atoms) on a plate is shown. See text for more details. (e) Space-filling model of isostearic acid (acid H not shown) and its chemical formula. Acid root indicated by arrow. (f) Same as (e) for tricosanoicacid.

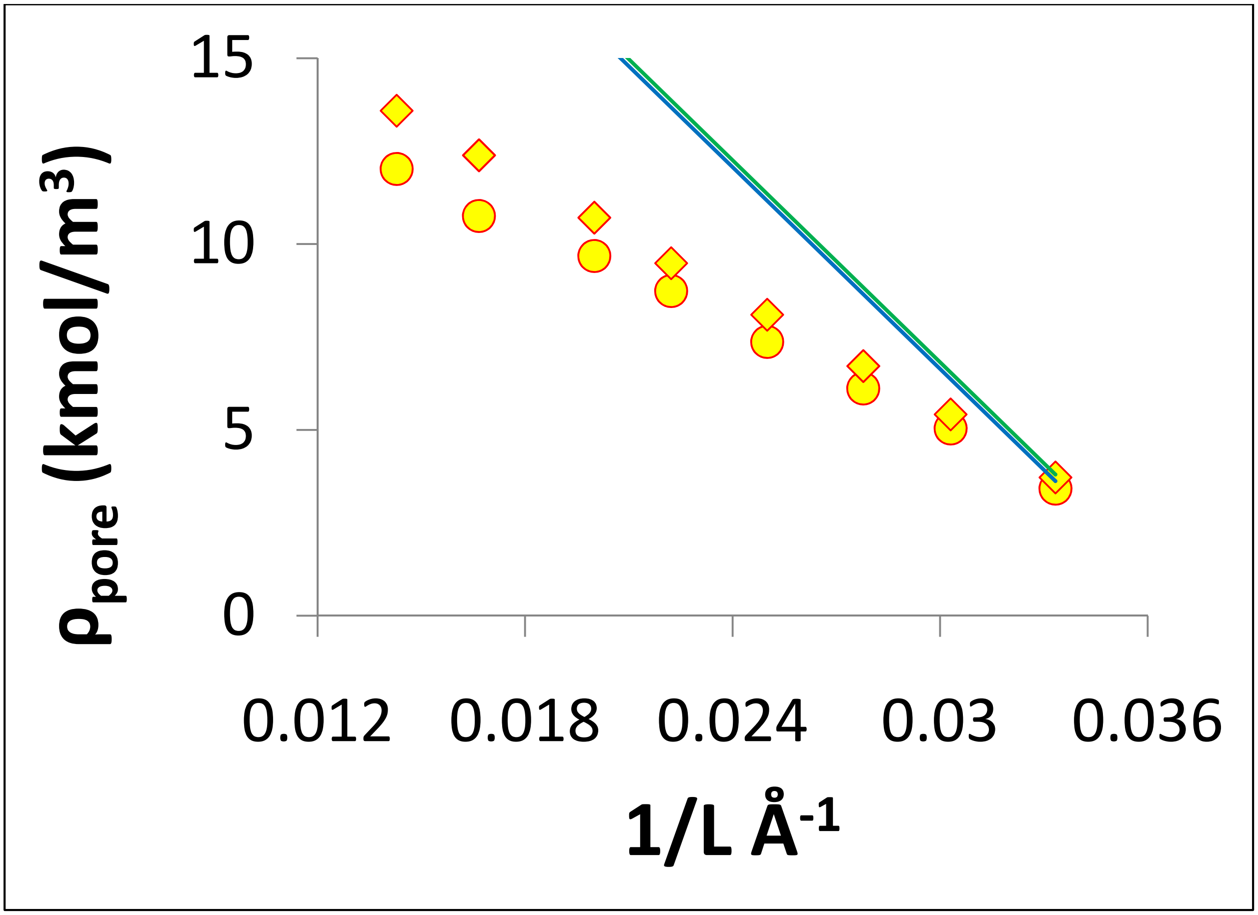

Figure 4.2: Plot of ρ_{pore} vs. 1/L for isostearicacid passivated slit pore with CO_2 as solvent. The symbols are the result of solutions of equation 4.6 while the solid lines are the straight line fits through them (see equation 4.7). Two bulk pressures are represented with *P_{bulk}=150 atm (* ● *)* and *P_{bulk}=300 atm (*◆*).* The error bars for the fit are less than size of the symbols.

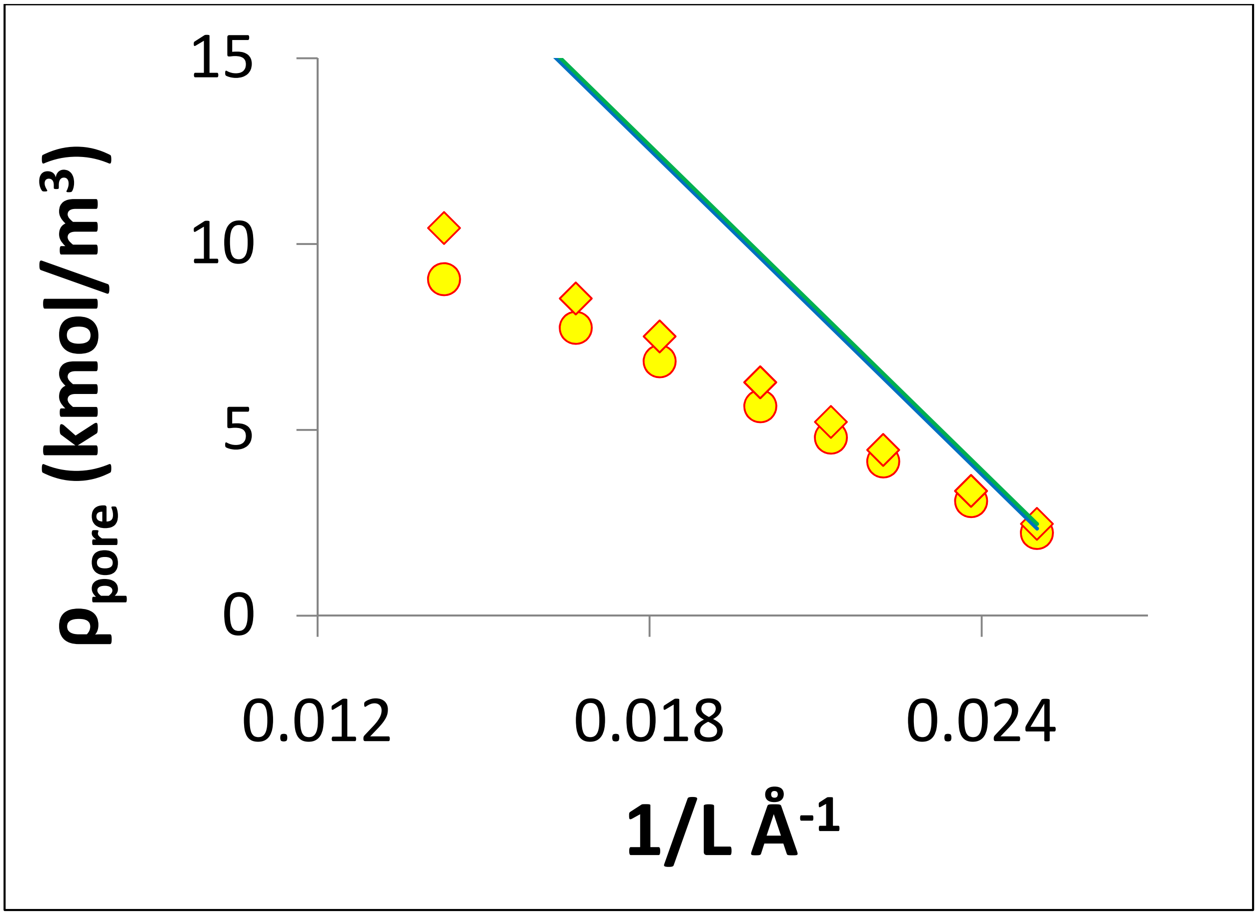

Figure 4.3: Plot of ρ_{pore} vs. 1/L for isotricosanoicacid passivated slit pore with CO_2 as solvent. The symbols are the result of solutions of equation 4.6 while the solid lines are the straight line fits through them (see equation 4.7). Two bulk pressures are represented with P_{bulk}*=150 atm (* ● *)* and P_{bulk}*=300 atm (*◆*).* The error bars for the fit are less than size of the symbols.

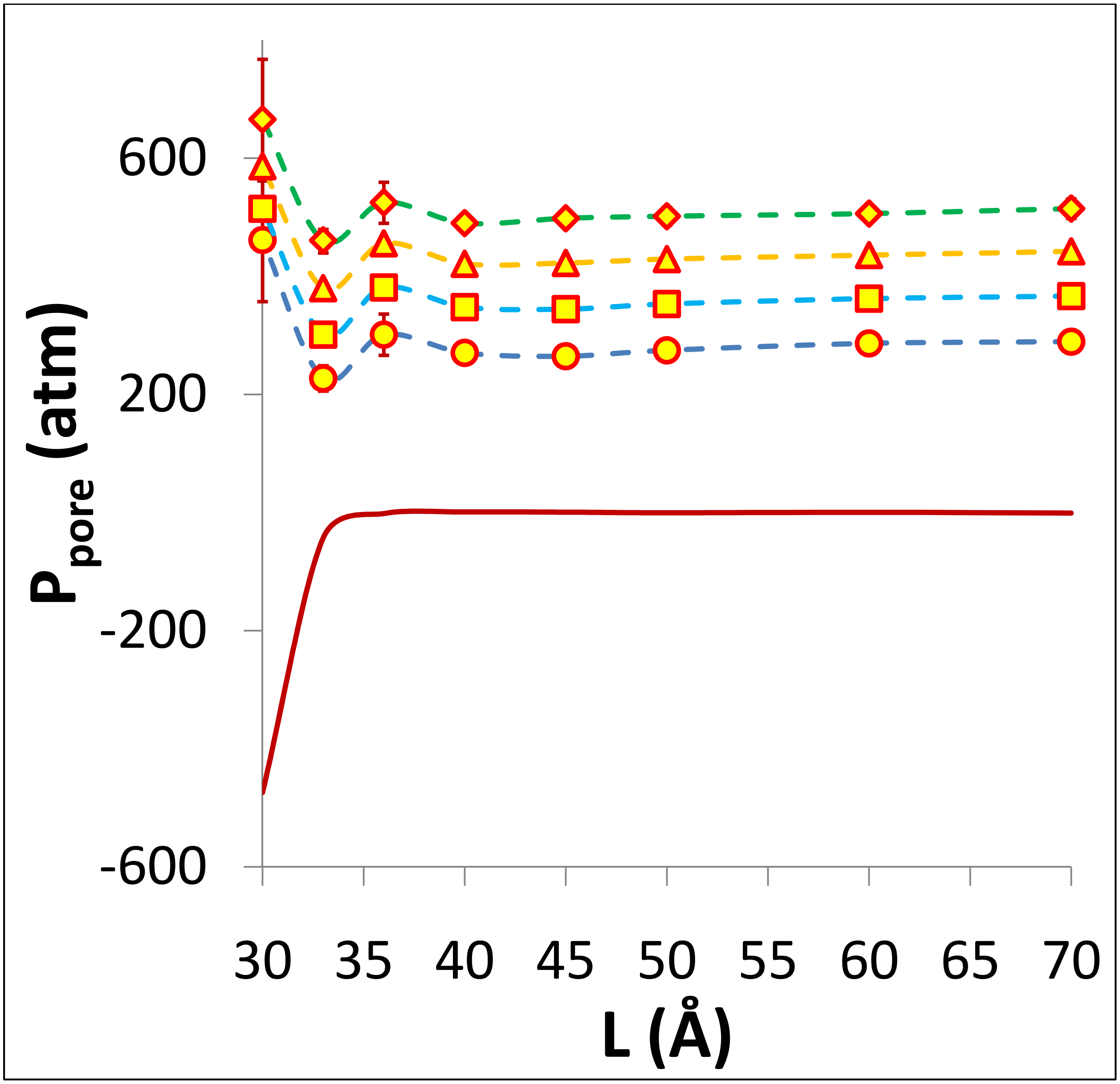

Figure 4.4: Plot of P_{pore} *vs. L* calculated using the procedure described in section 4.3 for isostearic acid passivated pores solvated by CO_2 for various values of bulk pressures. The symbols are the result of said calculation for various values of *L* while the broken lines are meant to guide the eye. The four bulk pressures represented are P_{bulk}*=150 atm* (○), *Pbulk=200atm* (□), *Pbulk=250atm* (△) and P_{bulk}*=300 atm* (◇). The solid line (▬)is the corresponding curve for interactions in vacuum. For clarity, only error bars for P_{bulk}*=150 atm* and P_{bulk}*=300atm* are shown. The error bars for the other pressures are similar. Interactions for *L<30Å* are strongly repulsive (high P_{pore}) and the corresponding values are not shown.

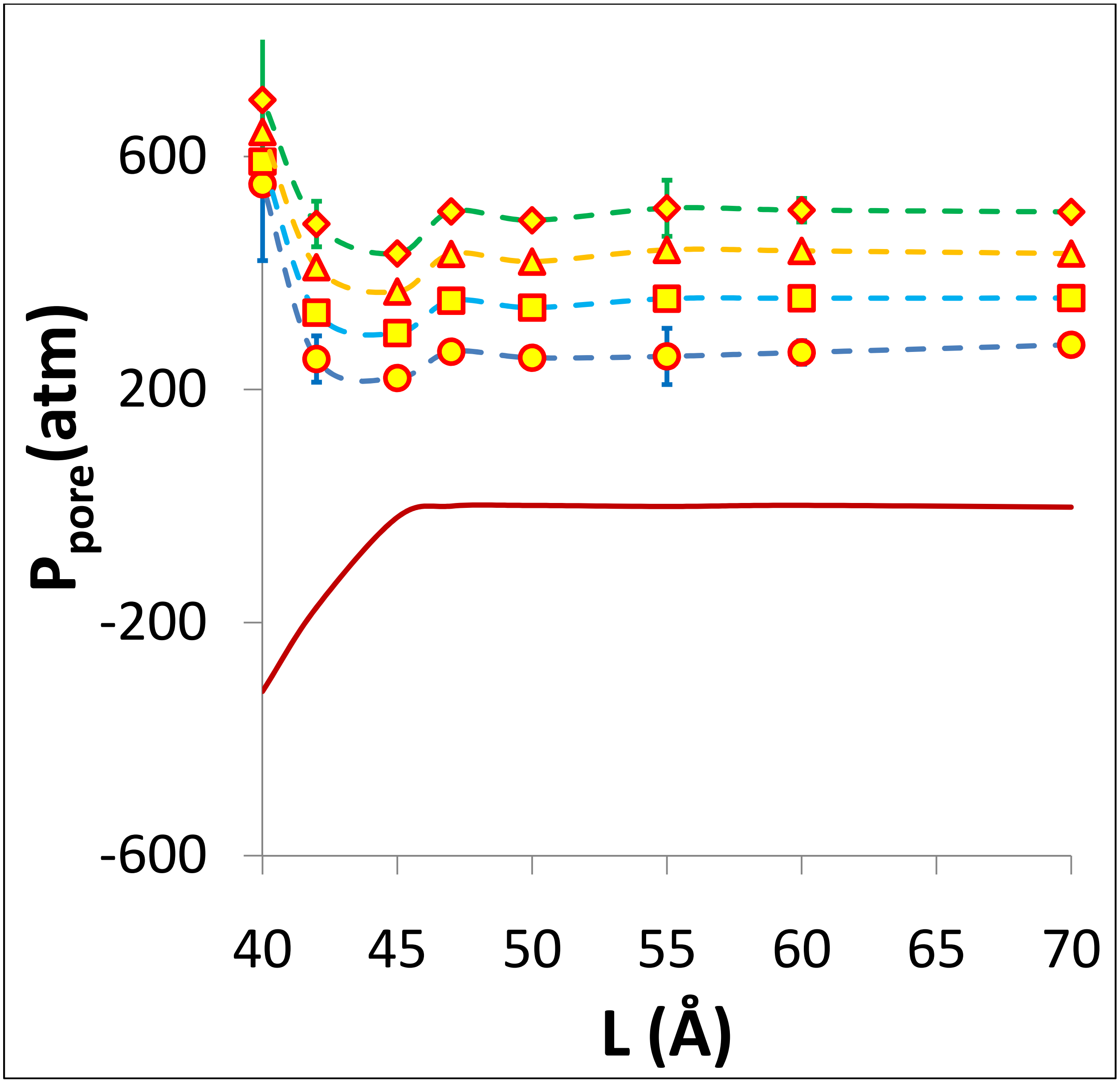

Figure 4.5: Plot of P_{pore} *vs. L* calculated using the procedure described in section 4.3 for isotricosanoic acid passivated pores solvated by CO_2 for various values of bulk pressures. The symbols are the result of said calculation for various values of L while the broken lines are meant to guide the eye. The four bulk pressures represented are *P_{bulk}=150 atm (○), Pbulk=200atm (□), Pbulk=250atm (△)* and *P_{bulk}=300 atm (◇).* The solid line (▬) is the corresponding curve for interactions in vacuum. For clarity, only error bars for *P_{bulk}=150 atm* and *P_{bulk}=300atm* are shown. The error bars for the other pressures are similar. Interactions for *L<40Å* are strongly repulsive (high P_{pore}) and the corresponding values are not shown.

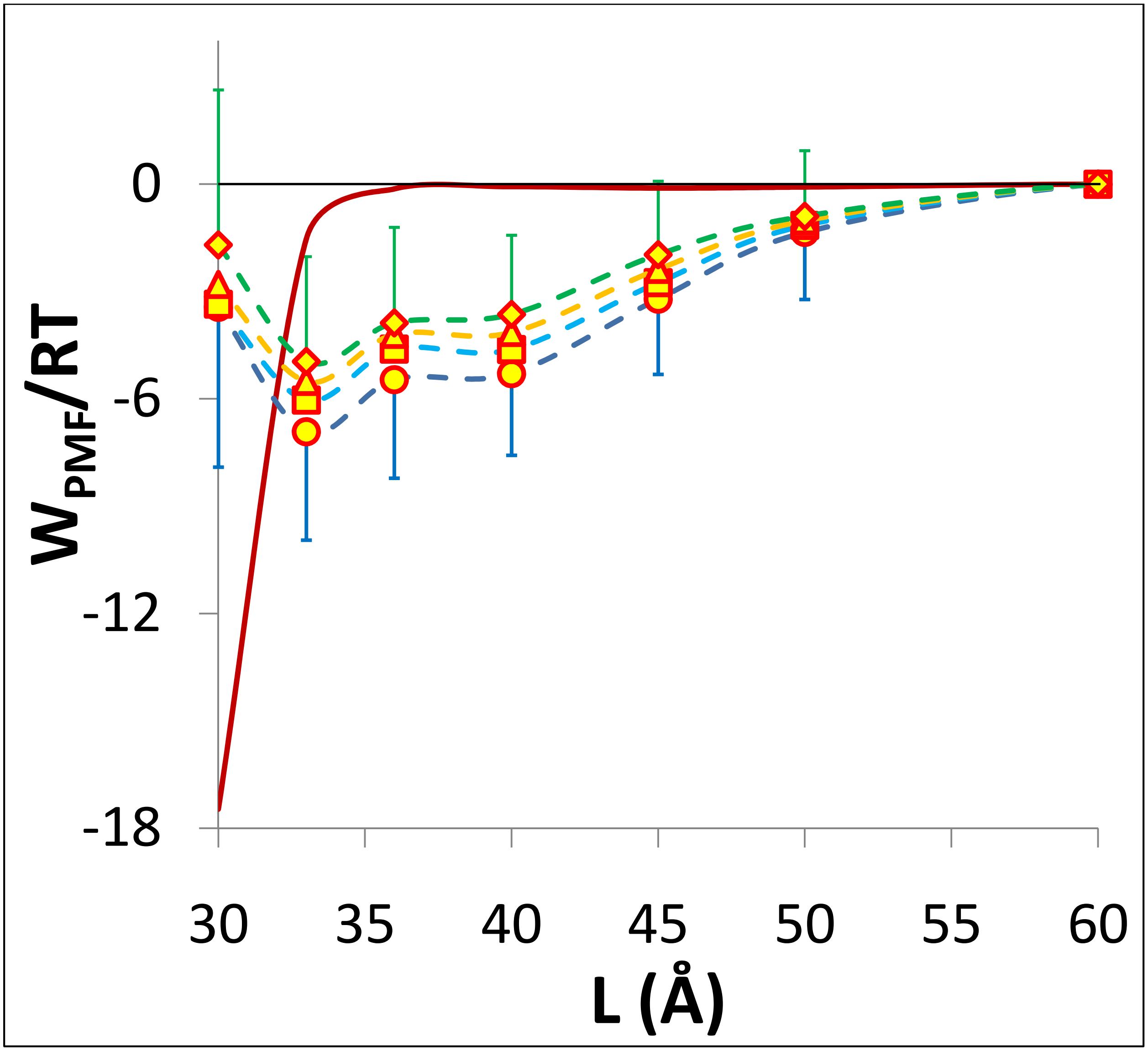

Figure 4.6: Potential of mean force for isostearic acid passivated slit pores solvated by CO_2 at various pressures is calculated using equation 4.2 as shown in section 4.3. For the calculation, P_{bulk}^{eff} is calculated using $L_{trunc}=60Å$ (see equation 4.3). The free energy corresponding to a single periodic image is attributed to a pair of particles to calculate the free energy per mole. The symbols are the result of said calculation for various values of *L* while the broken lines are meant to guide the eye. The four bulk pressures represented are $P_{bulk}=150$ *atm* (○), *Pbulk=200atm* (□), *Pbulk=250atm* (△) and $P_{bulk}=300$ *atm* (◇). The solid line (▬▬)is the corresponding curve for interactions in vacuum. For clarity, only lower error bars for $P_{bulk}=150$ *atm* and upper error bars for $P_{bulk}=300atm$ are shown.

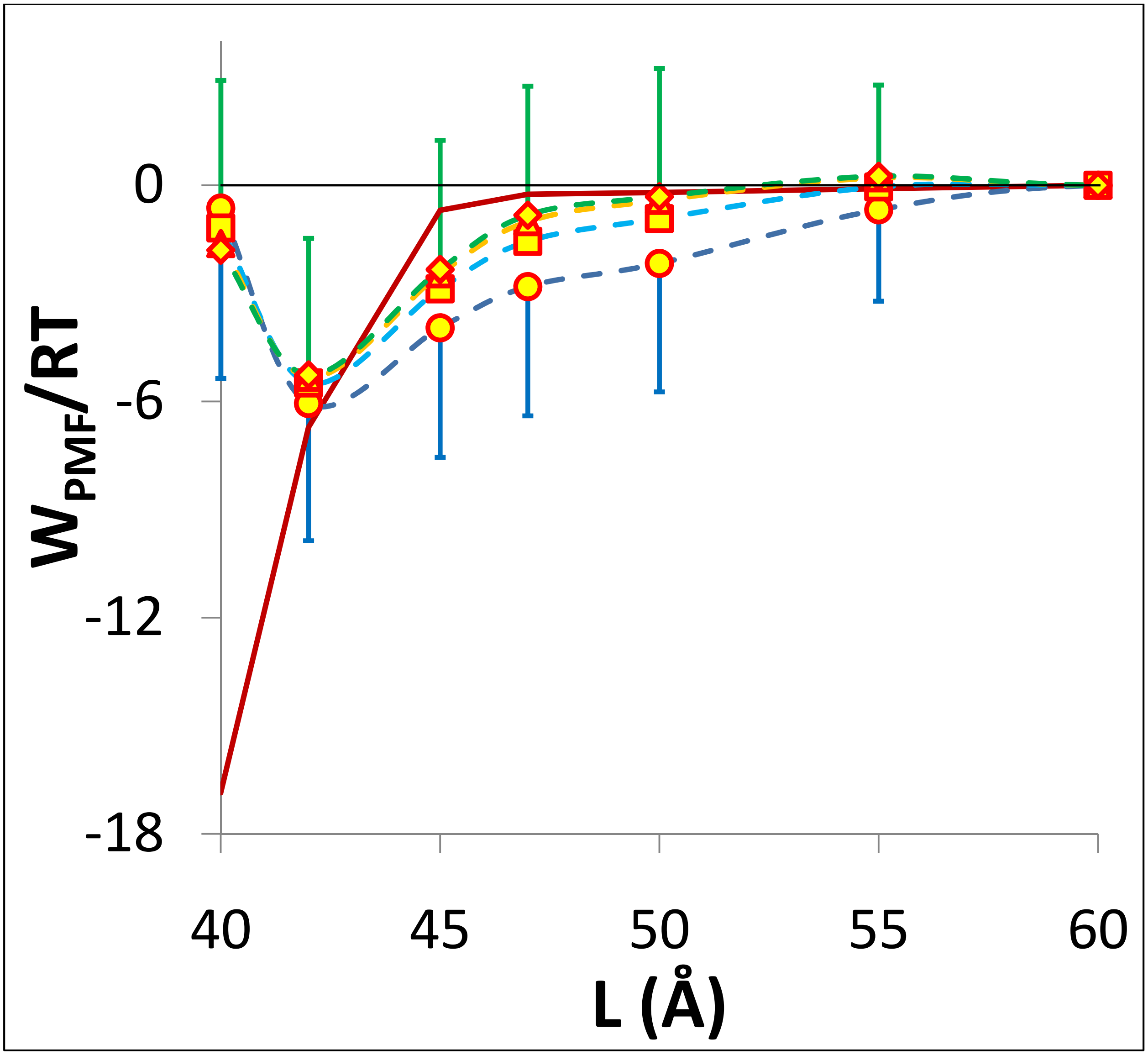

Figure 4.7: Solvated free energy of the slit-pore for isotricosanoic acid passivated slit pores solvated by CO_2 at various pressures is calculated using equation 4.6 as shown in section 4.3. For the calculation P_{bulk}^{eff} is calculated using $L_{trunc}=60Å$ (see equation 4.2). The free energy corresponding to a single periodic image is attributed to a pair of particles to calculate the free energy per mole. The symbols are the result of said calculation for various values of *L* while the broken lines are meant to guide the eye. The four bulk pressures represented are $P_{bulk}=150$ *atm* (○), *Pbulk=200atm* (□), *Pbulk=250atm* (△) and $P_{bulk}=300$ *atm* (◇). The solid line (▬)is the corresponding curve for interactions in vacuum. For clarity, only lower error bars for $P_{bulk}=150$ *atm* and upper error bars for $P_{bulk}=300$*atm* are shown.

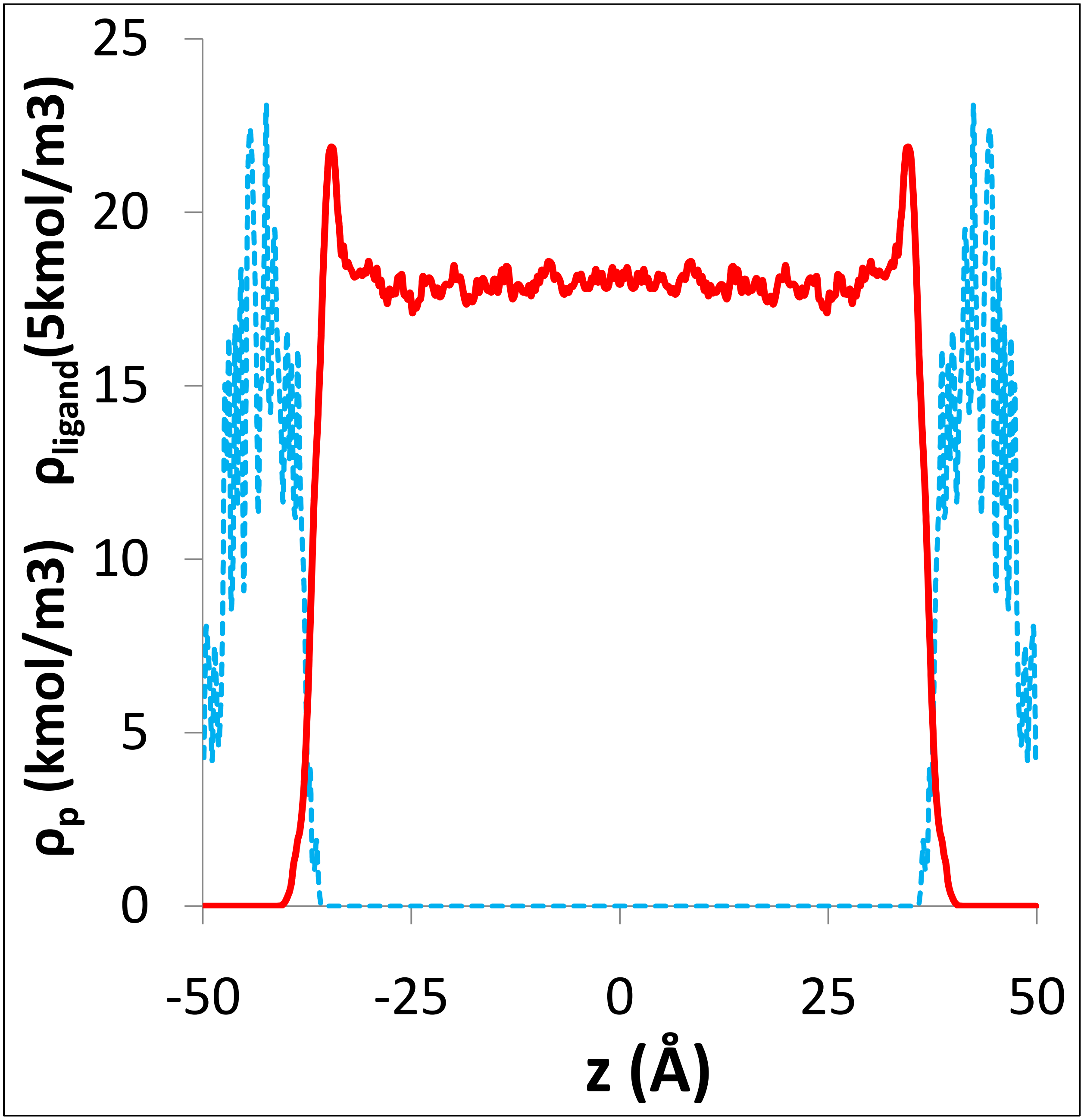

Figure 4.8: Density profile for a slit pore of gapwidth *L=100Å* passivated by isostearic acid ligands and solvated by CO_2 at a bulk pressure of P_{bulk}*=135 atm*. The density profile of the C atoms of the ligand (ρ_{ligand}) is shown by the broken line (▪ ▪) while the solvent density profile ρ_p is the solid line (▬). The density profile is determined using the entire cross section of the periodic image of the slit pore.

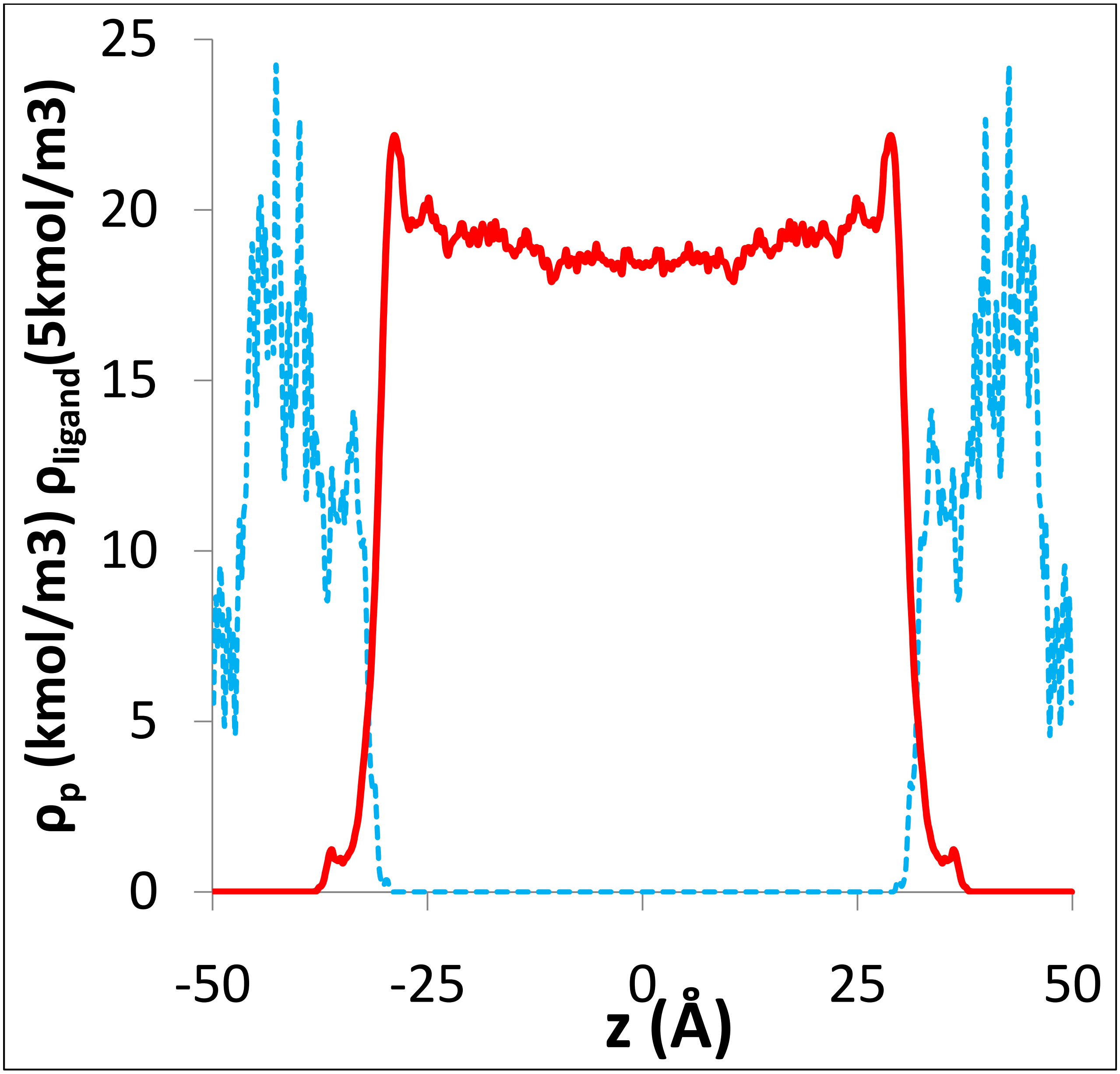

Figure 4.9: Density profile for a slit pore of gapwidth *L=100Å* passivated by isotricosanoic acid ligands and solvated by CO_2 at a bulk pressure of $P_{bulk}=162$ *atm*. The density profile of the C atoms of the ligand (ρ_{ligand}) is shown by the broken line (▪ ▪) while the solvent density profile ρ_p is the solid line (▬). The density profile is determined using the entire cross section of the periodic image of the slit pore.

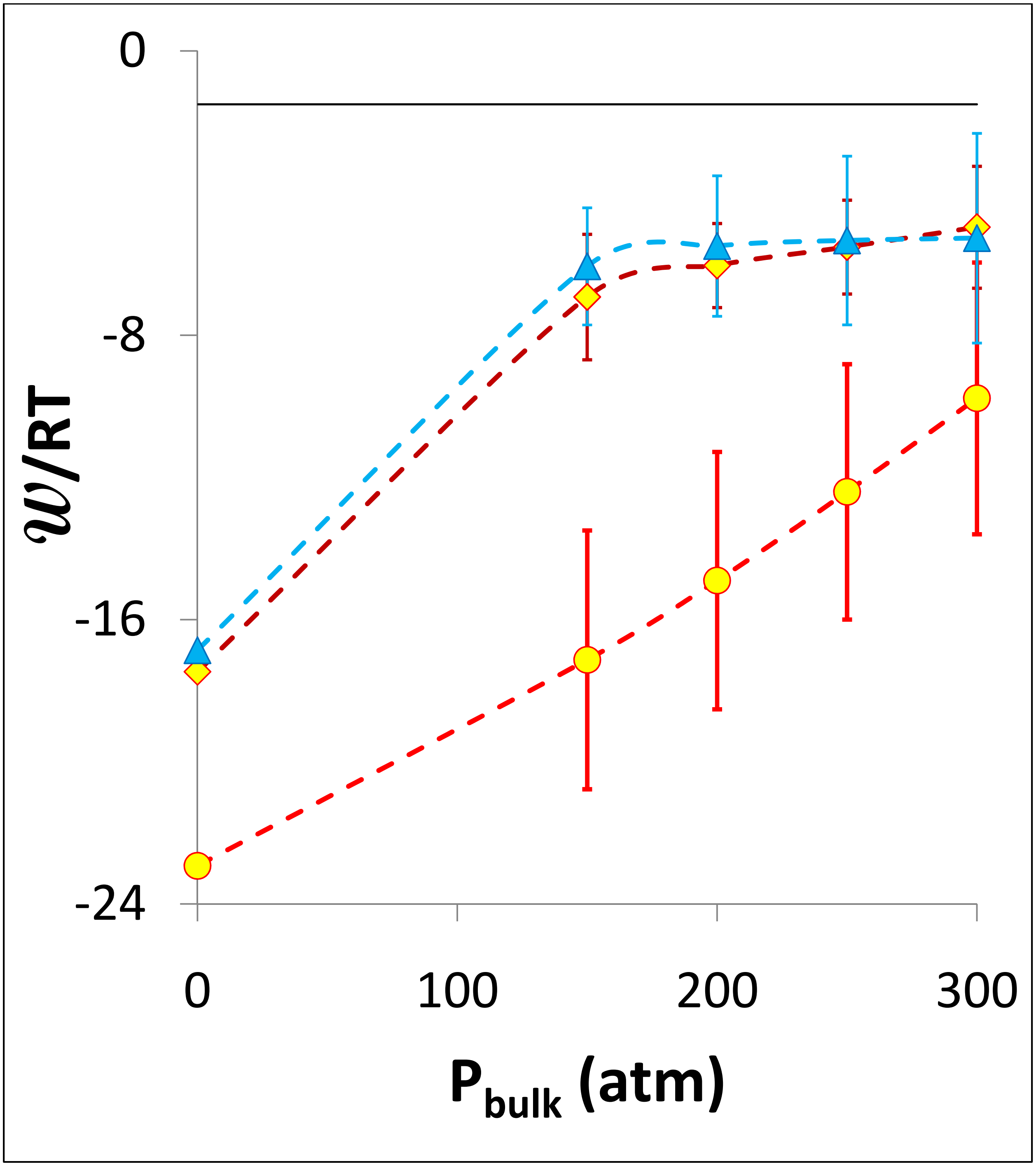

Figure 4.10: Plot of $\mathcal{W}$ vs. P_{bulk} (see equation 4.1) for CO_2 solvated slit pores passivated by n-dodecanethiol *(* ● and *L_{eq}=43Å),* isostearic acid(◆ and *L_{eq}=33Å),* isotricosanoic acid *(* ▲ and *L_{eq}=42Å).* The interactions for a single periodic image are attributed to a single particle pair. The thin solid horizontal line corresponds to -1.5RT so that $\mathcal{W}$ values greater than this imply a thermodynamically stable dispersion. The dotted lines are guides to the eye.

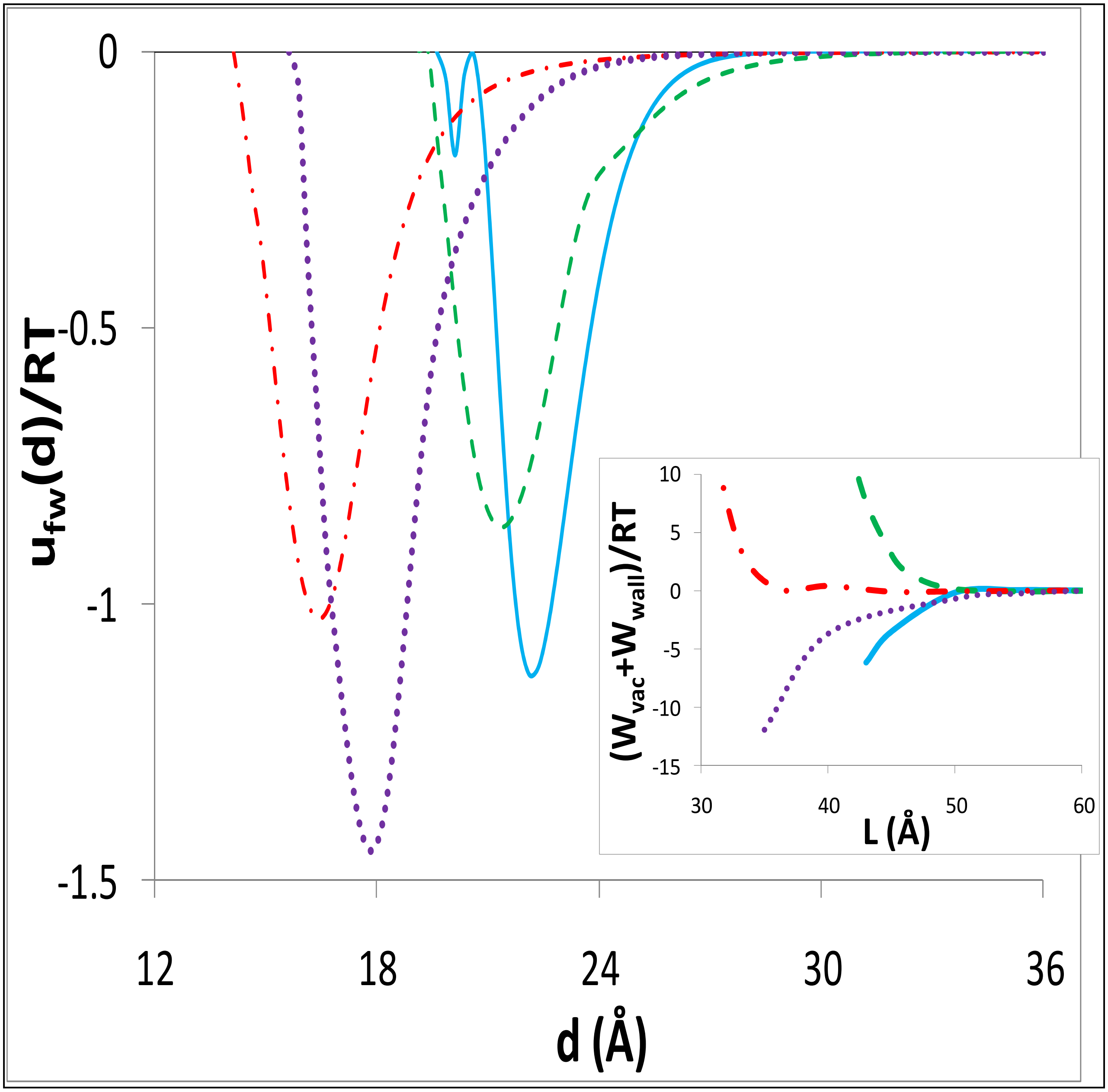

Figure 4.11: Wall-solvent interaction potential calculated using density profiles for wide slit pores (L=100Å). The inset chart shows $W_{vac}+W_{wall}$ for $P_{bulk}=300atm$. In both charts, the solid line (━━━━━━) is for n-dodecanethiol (16Å^2/ligand) taken from earlier data, the dashed line (▬ ▬ ▬) is for isotricosanoic acid (31Å^2/ligand), the dotted-and-dashed line (▬ ▪ ▬) is for isostearic acid (31Å^2/ligand) passivated pores while the dotted line (● ● ● ● ● ● ● ●) is for densely packed isostearic acid (20Å^2/ligand) passivated pores.

Chapter 5: Why are fluorocarbons hydrophobic?

5.1 Introduction

Perfluorinated alkanes which have all the hydrogen (H) atoms of an alkane replaced with fluorine (F) atoms are known to have much lower water solubilities than the corresponding hydrocarbons (Gough, Pearlman, & Kollman, 1993) (Krafft & Riess, 2007) while at the same time showing high lipophobicity (Krafft & Riess, 2007) and an extraordinary affinity for carbon dioxide (DeSimone, Maury, Menceloglu, McClain, Romack, & Combes, 1994) (Eastoe, Gold, & Steytler, 2006). Enzyme inhibitors with fluorinated moieties, show stronger binding than their non-fluorinated analogues (Biffinger, Kim, & DiMagno, 2004) even if the group on the inhibitor is not among those that bind to the active site (Gao, Qiao, & Whitesides, 1995) – consistent with the expectation from higher hydrophobicity. One explanation for the greater hydrophobicity is that a larger hydrophobic surface area is offered to water by the fluorocarbons compared to the hydrocarbons (Gao, Qiao, & Whitesides, 1995). The puzzling aspect of this is that since the C-F bond has a much greater dipole moment than does any other bond associated with carbon, a stronger binding with dipolar water might be expected. Further, although the polarizability of F in the C-F bond is relatively low considering its position in the periodic table, it is not lower than that of the C-H bond (Weast, Lide, Astle, & Beyer, 1990), so that the dispersion interactions of C-F with water are more attractive that those of C-H with water. Hence, the fluorocarbon surface could be argued to be more hydro*philic* than that of the corresponding hydrocarbon. A plausible resolution could be that the fluorocarbon with a molecular cross section of 28.3Å^2 (Kirsch, 2004) occupies sufficiently more volume and surface area in water than the corresponding hydrocarbon with molecular cross section is 18.9Å^2 (Fenter, Eisenberger, Li, Camillone III, Bernasek, & Scoles, 1991). Hence, the work done to form a cavity large enough to accommodate a fluorocarbon offsets the anticipated free energy benefit from enhanced energetic interactions with water. Further, if one considers the hydrophobic surfaces made via fluorocarbon coatings, these arguments related to cavity free energy do not pertain, and one might anticipate that such a surface would be more hydrophilic than a hydrocarbon, in contrast to experimental results (Graupe, Takenaga, Thomas, Colorado Jr, & Lee, 1999). It is not readily apparent whether there is an *additional* "polar hydrophobic" effect (Biffinger, Kim, & DiMagno, 2004), i.e., whether the entropic penalty from restriction of solvent structure due to polar interactions offsets the energetic benefit of the same. Given the great interest in quantitatively understanding hydrophobicity (Chandler, 2005), we have undertaken a calculation of the difference in water-solvation free energy between a hydrocarbon (n-octane) and its perfluorinated analogue (perfluorooctane) using all atom molecular dynamic simulations. First, we have transformed the hydrocarbon into the fluorocarbon in stages: (a) stiffenening the backbone (b) fattening the H atom Lennard-Jones diameter to match that of the F atom (c) lengthening the C-H bonds (d) strengthening the LJ energy parameter of the H atom to that of the F atom and finally (e) changing the electrostatic charge of the H atom to that of the F atom. The free energy and interaction energy changes calculated for each transformation yield considerable insight into the physics behind the hydrophobicity of fluorocarbons. Further, in order to isolate the effect of the *surface* and given the practical utility of hydrophobic surfaces (Li, Reinhoudt, & Crego-Calama, 2007), we have also conducted contact-angle simulations of water on self-assembled monolayers (SAM) of hydrocarbon and fluorocarbon thiols.

Our results for solvation free energy as well as contact angle are consistent with experimental observations. We have found that the main reason that the fluorocarbon solute is more hydrophobic than hydrocarbon solute is due to its "fatness" i.e. due to the relatively greater area/volume it occupies in water leading to a greater free-energy penalty for hydration. The bulk of this difference is due to the unfavourable solvent entropic changes associated with the greater volume and area of the fluorocarbon – the change associated with bond-lengthening, in our protocol, being the most unfavourable. Interestingly, the increased hydrophobicity of a fluorocarbon SAM compared to a hydrocarbon SAM is *also* because of the "fatness" of the fluorocarbons. In this case it causes them to pack less densely (lattice spacing 5.9Å) than the hydrocarbons (lattice spacing 4.97Å) which is enough to offset their affinity for water. Our simulations show that if the fluorocarbons packed with the *same* density as the hydrocarbons that fluorocarbon SAM would be the more hydrophilic.

A striking aspect of the results is the indifference of the water structure, whether it is solvating a solute in its bulk or is a droplet on a flat surface, to the nature of the solute/surface. Even substantial changes in the electrostatic nature of the solute/surface produce only minimal changes in characteristic water structure and relatively small changes in the free energy of interaction with water. The latter, though not the former, is quite responsive to the Lennard-Jones interactions. For both the solute as well as the surface, this behaviour can be traced directly to the strong tendency of water to minimize disruption of its hydrogen-bonded network (Cheng & Rossky, 1998) (Lee, McCammon, & Rossky, 1984).

At least for the solute, we do not see an additional "polar-hydrophobicity". Greater polarity of the bonds in the solute results in greater hydrophilicity with the favourable energetic interactions partially offsetting the higher entropic penalty upon solvation. We can also use these insights to explain the high CO_2-philicity and surface activity of fluorinated hydrocarbons which may be useful in guiding design of surfactants for water in CO_2 emulsions which are important for a number of applications (Johnston & da Rocha, 2009) ranging from enhanced oil recovery (Rossen, 1996) to biology (Johnston, et al., 1996) (Harrison, Goveas, Johnston, & O'Rear, 1994) to "green" chemistry (DeSimone J. M., 2002) (Sagisaka, et al., 2008).

Additionally (and peripherally) we have been able to propose a microscopic description for *line-tension* (Amirfazli & Neumann, 2004) effects in contact angle measurements.

5.2 Simulation Strategy and Computational Details

Since the methods and models we have employed are fairly standard, we will only describe them briefly. We are have done two different types of calculation. The first is calculation of the solvation free energy difference between a short chain fluorocarbon and its corresponding hydrocarbon in ambient water. The other is a calculation of the contact angle between a water droplet and a number of different surfaces. For each case, we give a general description of the quantity we seek to calculate, the simulation strategy we employ and finally the details of the molecular models and simulation parameters.

5.2.1 Calculation of Difference in Solvation Free Energies

Our endeavour is to determine the reason behind the hydrophobicity of fluorocarbons compared to that of the hydrocarbons. Hence, the parameter of interest is the difference in the free energies of solvation of the two representative molecules from each category viz. octane for hydrocarbons and perfluorooctane for fluorocarbons. By "free energy of solvation" we mean the free energy change that accompanies the passage of a single molecule from vapour (ideal gas) state into a body of pure liquid ,which in our case is water. Since it is much more convenient to carry out simulations in bulk-fluid media rather than across interfaces, we calculate the difference in solvation free energies indirectly as illustrated in Figure 5.1. The quantity we seek to calculate is the free energy change accompanying the transformation of a hydrocarbon molecule to a fluorocarbon molecule when the value in vacuum is *subtracted from* the same quantity calculated when the molecules are solvated by water at 298.16K. Since the pressure dependence of solubility in water is weak (Hildebrand solubility parameter of water at 298.16K is 47.9 $(J/cm^3)^{0.5}$ at 1 atm and 50.6 $(J/cm^3)^{0.5}$ at 3000 atm (http://webbook.nist.gov/chemistry/fluid/) (Allada, 1984)) we carry out our simulations at pressures of ~3000atm rather than ~1atm to slightly exaggerate the effect of excluded volume interactions.

5.2.1.1 Method of Thermodynamic Integration

The free energy change accompanying the transformation in a given medium is calculated using a standard method called thermodynamic integration (Frenkel & Smit, 2002). We will describe this method briefly:

Consider the problem of finding the free energy change accompanying transformation of a moiety from state A to state B. First we identify the parameters of the moiety that are pertinent to the transformation i.e. those that undergo change. These are often a set of bond lengths and/or electrostatic charges and/or Lennard Jones interactions etc. Then we couple these to a parameter typically denoted by λ which is between 0 and 1. For example, if a bond length is being transformed, the coupling could be as follows: $l_{bond}=l_{bond\text{-}A}(1-\lambda)+l_{bond\text{-}B}\lambda$. This is an example of linear coupling, which is most common and which we have used. Hence if $H(\lambda)$ is the Hamiltonian of a system corresponding to a given λ, then the Hamiltonian of states A and B are given by $H(\lambda=0)$ and $H(\lambda=1)$ respectively. Since the canonical ensemble partition function is given by $Q_{NVT}(\lambda)=\int d\mathbf{p}d\mathbf{q}\exp\left(-\frac{H(\mathbf{p},\mathbf{q},\lambda)}{k_BT}\right)$ and it is related to the Helmholtz free energy by $F=-k_BT\log Q_{NVT}$, it is readily apparent that $\frac{\partial F}{\partial\lambda}=\left\langle\frac{\partial H}{\partial\lambda}\right\rangle_\lambda$ i.e. $\Delta F=\int_0^1\left\langle\frac{\partial H}{\partial\lambda}\right\rangle_\lambda d\lambda$. Here **p** refer to the set of pertinent momentum vectors, **q** to the set of pertinent position vectors and $\langle x\rangle$ is the *ensemble averaged* value of the quantity *x* i.e. $\langle x\rangle=\frac{1}{Q_{NVT}}\int d\mathbf{p}d\mathbf{q}x\exp\left(-\frac{H(\mathbf{p},\mathbf{q})}{k_BT}\right)$.

Now, in order to get the required free energy change *ΔF*, we need to run canonical ensemble simulations (constant volume, temperature and particle number) for states corresponding to a number of different values of λ between 0 and 1 and calculate $\left\langle \frac{\partial H}{\partial \lambda} \right\rangle_{\lambda}$ for each. If the system is fairly well behaved, i.e., $\left\langle \frac{\partial H}{\partial \lambda} \right\rangle_{\lambda}$ does not oscillate rapidly with λ, we only need to calculate for values of λ at Gaussian quadrature points between 0 and 1 and hence obtain ΔF by Gaussian Quadrature.

5.2.1.2 *Stages in Transformation and End-States*

Since we want to resolve the various contributions to the free energy difference between the hydrocarbon and fluorocarbon, we carry out the transformation in stages. Each transformation stage is carried out in vacuum as well as in bulk water – the difference in the corresponding free energy change giving us the number we need. For each transformation stage, we use a 10 point Gaussian Quadrature to evaluate the corresponding ΔF .

Starting with the hydrocarbon (State 0), the stages in the transformation are as follows:

1. **Stiffen:** Here the angular and dihedral potential parameters are coupled to λ. We change them from those of the hydrocarbon molecule to those of the fluorocarbon. The result is that the effect of stiffening the backbone on solvation is isolated and the resulting molecule is called State 1.
2. **Fatten:** Here the value of the Lennard-Jones diameter (σ) of the hydrocarbon H atom is coupled to λ and transformed to that of the F atom. Note that we now start with the *already stiffened* molecule i.e. from State 1. This shows the effect on solvation due to the larger size/molecular-cross-section of the F atom. The resulting molecule is State 2.
3. **Lengthen:** The C-H bond length and stiffness are coupled to λ and transformed to those corresponding to the C-F bond. We start with the stiffened and fattened molecule (State 2). This shows the effect on solvation of lengthening the C-H bond i.e. increasing the molecular cross sectional area. This molecule is State 3.

4. **Strengthen:** The value of the Lennar-Jones energy parameter (ε) is coupled to λ and transformed to that of the F atom. We start with the stiffened, fattened and lengthened molecule (State 3). This shows the effect of higher Lennard-Jones energetic interactions on solvation. Resulting molecule is State 4.
5. **Charge:** The values of the electrostatic charges on the various charge sites on the stiffened, fattened, lengthened and strengthened molecule (State 4) are coupled to λ and transformed to those corresponding to the fluorocarbons. At the end of this step, the transformation to fluorocarbon (State 5) is complete. This shows the effect of electrostatic interactions on solvation.

We also do the transformation with the order of the Atom-Fattening and Bond-Lengthening steps exchanged. In Table 5.1 we tabulate the various parameters coupled to λ for the different stages and their initial and final values. Note that for all stages the system *volume* is constant and the system pressure varies between 2500-3000 atm.

5.2.1.3 System Setup and Molecular Models

The system setup is very simple – a single solute (either hydrocarbon or fluorocarbon) molecule is placed in a cubic periodic cell of side 30Å. If solvated interactions are to be calculated, the cell is filled with 938 SPC/E (Berendsen, Grigera, & Straatsma, 1987) water molecules. This corresponds to a pressure of ~3000 atm at 298.16K. The hydrocarbon's molecular parameters are taken from OPLS (Jorgensen, 2002) with the exception that the atomic weight of the H atom is taken to be the same as that of the F atom. Since kinetics are not being calculated, this will make no difference to the results. The fluorocarbon molecular parameters are also taken from OPLS with the exception of their charges which we calculated in as described in chapter 3. These are calculated using GAMESS (ESP with the native routine using 6-31G(p,d)) (Schmidt, et al., 1993) and yield a charge of -0.17e on each F of CF_3 and -0.12e on each F of CF_2. The charge on C of each CF_3/CF_2 group is adjusted so that each group is neutral.

5.2.1.4 *Simulation Details*

The simulations are executed using GROMACS 4.0 (van der Spoel, Lindahl, Hess, Groenhof, Mark, & Berendsen, 2005). Visualisation is done using VMD (Humphrey, Dalke, & Schulten, 1996). Simulation timestep is 0.001 ps. The canonical ensemble is implemented using Nose Hoover thermostat with 0.1 ps time constant. Lennard-Jones interactions are cut-off at 10.0Å. Electrostatic contributions are calculated using Particle Mesh Ewald (PME) (Essmann, Perera, Berkowitz, Darden, Lee, & Pedersen, 1995) with a direct interaction cutoff of 10.0Å, 4th order interpolation, grid spacing of 1.2Å and a tolerance of 10^{-5}. All systems are equilibrated for 1 ns. For each transformation stage, the intermediate systems (i.e. those for which $0<\lambda<1$) a production run of 2ns is executed to obtain $\left\langle \frac{\partial H}{\partial \lambda} \right\rangle_{\lambda}$. The end-points for each stage (i.e. those corresponding to $\lambda=0$ or $\lambda=1$) have a production run of 5 ns. The bond constraints for SPC/E water are implemented using the LINCS algorithm (Hess, P-lincs: A parallel linear constraint solver for molecular simulation, 2007). The codes for implementing the PME and LINCS and for obtaining $\frac{\partial H}{\partial \lambda}$ at every step of a given simulation are all built into GROMACS 4.0. Convergence and error analysis are done by the method of Hess (2002) (Hess, 2002) also using a built in script.

From the snapshots taken from the endpoint calculations, molecular surface area of the solute is calculated using the SURFCV code downloadable from the Honig group (Nicholls, Sharp, & Honig, Software: SURFace Algorithms, 1991) (Nicholls, Sharp, & Honig, 1991). The probe radius used is r_{probe}=1.4Å. Atomic radius (r_{atom}) of C atoms is taken as 1.5Å, of H atoms is 1.25Å and of F atoms is 1.475Å. After the atom-fattening step all H atoms are considered to have F atom radii. The volume denied to the centre of the solvent atoms (i.e. solvent excluded volume (Richmond, 1984)) is calculated using a grid of 0.5Å resolution with all grid cells whose centers are less than $r_{probe}+r_{atom}$ from any solute atom included in the denied volume. Both the surface area and excluded volume calculations assume the solvent and solute atoms to be hard-spheres and hence do not reflect the effect of changing "softness" of the particles e.g. in the strenghtening transition. For this, the relevant quantity is $r_{peak}O$ which is the radial distance from the terminal/central carbon atom, of the peak in the curve of the pair distribution function ($g_{C-O}(r)$, bin-width of 0.5Å) between terminal/central carbon atoms of the solute and the oxygen atoms of water. The peak is obtained by fitting a polynomial to the region in the neighbourhood of the peak and noting the point where it reaches its maximum. The orientational distribution of water molecules around the terminal carbon atoms of the solute is calculated by taking the distribution of the cosine of the C-O-H angle (C is the terminal carbon atom and O→H is one of the hydroxy bonds of water, bin-width is 0.01) for water molecules within a hemispherical shell of radius $r_{peak}O+1.5Å$ capping the terminal carbon atoms of the solute and, therefore, for which the angle $\theta_{C-C'-O}$ (C' is the second carbon atom from the terminal C atom in the solute and O is a water oxygen) is less than 90^{o}. The end-to-end distance i.e. distance between the terminal carbon atoms of the molecules is also calculated.

5.2.2 Calculation of Contact Angles

To investigate/illustrate the isolated effect of the hydrocarbon/fluorocarbon surface with water, we carry out contact angle simulations since the contact angle is a macroscopic, hence easily measured, quantity which is directly related to the interfacial free energy change of wetting by Young's relation: $\gamma_{SL} - \gamma_{SV} = \gamma_{LV} \cos\theta$. Here γ_{LV} is the liquid-vapour interfacial free energy and θ is the contact angle (see Figure 5.2a) while γ_{SL} and γ_{SV} are the solid-liquid and solid-vapour interaction free energies respectively. The larger the contact angle, the less favourable is the wetting of the solid by the liquid. In order to compare with the experiments of Graupe et al (1999) (Graupe, Takenaga, Thomas, Colorado Jr, & Lee, 1999) which are relevant to our argument, we have decided to simulate a droplet of water in contact with a self-assembled monolayer rather than in contact with a crystalline polymer surface (Fan & Cagin, 1995) (Hrivi & Pakkanen, 2006). This means we are examining the isolated effect of the hydrocarbon/fluorocarbon *tips* with water but since the tips are chemically similar to the lateral surfaces of the isolated molecules, this will not detract from the point we seek to make.

5.2.2.1 Simulation Setup and Molecular Models

Instead of using n-octane and n-perfluorooctane, we will be using n-decanethiol (CH_3-$(CH_2)_9$-SH) and perfluorodecanethiol (CF_3-$(CF_2)_7$-CH_2-CH_2-SH). The substrate will be a monolayer of hexagonally closed packed LJ particles (ε=0.226828 kcal/mol, σ=2.708Å) with lattice spacing of 2.88Å. The purpose of the substrate is simply to provide a hard wall to anchor and constrain the ligands molecules and the actual interaction with water is not important since water molecules are several molecular diameters away from the substrate. The substrate parameters we use are the results of ab-initio calculations for silver atoms (Vidali, Ihm, Kim, & Cole, 1991) (Gatica, Li, Trasca, Cole, & Diehl, 2008) interacting with xenon (Berry, Rice, & Ross, 2000). The parameters for the thiol are taken from OPLS – except that the charge of F on terminal CF_3 is -0.17e instead of -0.12e. The thiol root atoms (S) and the substrate atoms (Ag) are rigidly fixed in place. The S atoms are distributed in a hexagonal monolayer ~3.0Å above the substrate atoms with lattice spacing that varies with the case. The water droplet is composed of 2744 SPC/E water molecules. The simulation cell is 80Å in the x and y directions (i.e. along the plane of the substrate) while it is 200Å in the z direction (perpendicular to the plane of the substrate). This enables use of 3D Particle Mesh Ewald for calculation of electrostatics. The simulations are run in the canonical ensemble and use the same parameters for thermostat, PME, constraints and Lennard-Jones cutoffs as the free-energy simulations in section 5.2.1.4. A timestep of 0.001ps is employed. Each simulation is equilibrated for 1ns followed by a production run of 2ns. Configurations are written out every 0.5ps. Figure 5.2a shows a typical setup.

5.2.2.2 Determination of Contact Angle

The determination of contact angle substantially follows the standard procedure (Werder, Walther, Jaffe, Halicioglu, & Koumoutsakos, 2003) (Hrivi & Pakkanen, 2006) (Giovambattista, Debenedetti, &

Rossky, 2007). The result of each simulation is that 4000 snapshots of the system are generated. The *z* direction is perpendicular to the plane of the self-assembled-monolayer and the radial (*r*) direction is in the plane of the monolayer. All *r* values are calculated from the axis passing through the centre of mass of the water molecules. Cells are made of 0.1Å resolution in *z* and 0.5Å in *r* and using a simple binning procedure, the averaged density of water molecules (more correctly, the O atoms of water molecules) is obtained as a function of z and *r*. Then, for a fixed value of *z*, the density profile in *r* is fitted to the following form:

$$\rho(z,r)=\frac{1}{2}\rho_{bulk}(z)\left[1-\tanh\left(\frac{r-r_{border}(z)}{\alpha}\right)\right] \quad \text{… (5.1)}$$

Here for a given *z*, $\rho_{bulk}(z)$, $r_{border}(z)$ and α are constants to be fitted. $r_{border}(z)$ is the radial position of the vapour-liquid interface at a given *z* – and the corresponding plot appears for a typical system in Figure 5.2b. $\rho_{bulk}(z)$ gives the value at which the density saturates in the interior of the droplet for a given *z* and α determines the sharpness of the interface. Similarly, for a constant *r=0.5Å*, we can fit the plot of density vs. *z* to an equation of the type of equation 5.1 to yield the lower boundary of the droplet i.e. z_o and its upper crest at z_1.

We now fit the vapour-liquid interface profile to the following equations:

$$r_{border}=\sqrt{R^2-(z-z_c)^2} \quad \text{… (5.2a)}$$

and

$$r_{border}=\sqrt{R^2-(z-z_c)^2}+\sum_{i=0}^{7}a_i(z-z_c)^i \quad \text{… (5.2b)}$$

Here equation 5.2a is a fit of the profile to a circle while equation 5.2b is a fit of the profile to a deformed circle; the latter we denote here as the *polyfit*. *R* (the radius of the circle), z_c (the *z* position of the centre of the circle) and the various a_i are constants to be fitted.

A plot of $\rho_{bulk}(z)$ vs. *z* (Figure 5.2c) shows that the density of water near the solid-liquid interface is oscillatory or layered. An examination of the shape of the vapour-liquid interface shows a rapid increase in curvature in the same region which coincides with the layering associated with the surface interactions seen in Figure 5.2c; this is as expected for such a system (Werder, Walther, Jaffe, Halicioglu, & Koumoutsakos, 2003) (Hrivi & Pakkanen, 2006).

5.2.2.2.1 Definition of Contact Angle

Since the contact-angle is a macroscopic phenomenon, the experimentally evaluated angles do not reflect the curvature seen ~10.0Å from the interface. I.e., the actual angle made by the liquid with the interface and which is sometimes reported as the contact angle (Giovambattista, Debenedetti, & Rossky, 2007), cannot be the angle obtained from experiment. Another approach is to ignore the part of the vapour-liquid interface associated with the layered region i.e. that between z_o *and* z_o+d (where *d* is the thickness of the layered region) and use the angle at the interface made by the curve obtained by fitting a circle (see equation 5.2b) through all points outside the layering region (Werder, Walther, Jaffe, Halicioglu, & Koumoutsakos, 2003) (Hrivi & Pakkanen, 2006). One can argue that since the continuum approximation that underlies the definition of the contact angle breaks down at the boundary of the layered region, the "interface" should be defined there, i.e., at z_o+d. Hence we have now four definitions of the contact angle:

1. $\theta_{z_o}^{circle} = 180^{\circ} - \tan^{-1}\left(\frac{dz}{dr}\right)_{z=z_o,\text{equation 2a}}$ i.e., the angle obtained from the slope of the curve obtained by fitting the vapour-liquid interface to equation 5.2a (circle) intersecting with the solid-liquid interface i.e. at $z=z_o$.

2. $\theta_{z_o}^{polyfit} = 180^{\circ} - \tan^{-1}\left(\frac{dz}{dr}\right)_{z=z_o,\text{equation 2b}}$ i.e., the angle obtained from the slope of the curve obtained by fitting the vapour-liquid interface to equation 5.2b (polyfit) intersecting with the solid-liquid interface i.e. at $z=z_o$.

3. $\theta_{z_o+d}^{circle} = 180^{\circ} - \tan^{-1}\left(\frac{dz}{dr}\right)_{z=z_o+d,\text{equation 2a}}$ i.e., the angle obtained from the slope of the curve obtained by fitting the vapour-liquid interface to equation 5.2a (circle) intersecting with the border of the layered region i.e. at $z=z_o+d$.

4. $\theta_{z_o+d}^{polyfit} = 180^{\circ} - \tan^{-1}\left(\frac{dz}{dr}\right)_{z=z_o+d,\text{equation 2b}}$ i.e., the angle obtained from the slope of the curve obtained by fitting the vapour-liquid interface to equation 5.2b (polyfit) intersecting with the border of the layered region i.e. at $z=z_o+d$.

5.2.2.2.2 Boundary of Layered Region and Orientation of Water Molecules

The boundary of the layered region is obtained as follows. The positions (z_{peak1}, z_{peak2}) of the first two peaks of the $\rho_{bulk}(z)$ vs. z curve (Figure 5.2c) are identified and the gap between them is a measure of the periodicity of the layering. Hence the end of the layering region is taken to be:

$$z_o + d = z_{peak2} + \frac{z_{peak2} - z_{peak1}}{2} \qquad \text{… (5.3)}$$

In other papers (Hrivi & Pakkanen, 2006) (Werder, Walther, Jaffe, Halicioglu, & Koumoutsakos, 2003), the value of d has been fixed by inspection at about 8Å.

We have also calculated the distribution of the cosines of the angles made with the vertical by the O→H vectors of water molecules in the layers below $z=z_o$ (i.e., $\cos\theta_{v(zo)}$)and the 1Å thick layer centered at $z=z_{peak1}$ (i.e., $\cos\theta_{v(zpeak1)}$).

5.2.2.3 Cases

We simulate the following cases for contact angle calculations:

1. **Decanethiol (HC$_{4.97Å}$)**: The surface is composed of n-decanethiol molecules arranged in a hexagonal close packed lattice with lattice spacing of 4.97Å corresponding to the experimental value of alkanethiols on gold (Graupe, Takenaga, Thomas, Colorado Jr, & Lee, 1999) (Ulman, 1989) (Rovida & Pratesi, 1981) (Sellers, Ulman, Shnidman, & Eilers, 1993).

2. **Perfluorodecanethiol ($FC_{5.90Å}$)**: The surface is composed of n-perfluorodecanethiol molecules arranged in a hexagonal close packed lattice with lattice spacing of 5.90Å corresponding to the experimental value of fluoroalkanethiols on gold (Graupe, Takenaga, Thomas, Colorado Jr, & Lee, 1999).
3. **Hydrocarbon Charged Perfluorodecanethiol ($FCHC_{5.90Å}$)**: The surface is composed of n-perfluorodecanethiol molecules arranged in a hexagonal close packed lattice with lattice spacing of 5.90Å but with charge on F atoms equal to the charge on hydrocarbon H atoms (i.e. 0.06e) and charges on hydrocarbon C atom adjusted to make each "CF_2" and "CF_3" group neutral.
4. **Densely Packed Perfluorodecanethiol ($FC_{4.97Å}$)**: The surface is composed of n-perfluorodecanethiol molecules arranged in a hexagonal close packed lattice with lattice spacing of 4.97Å corresponding to the *hydrocarbon* packing density
5. **Densely Packed Hydrocarbon Charged Perfluorodecanethiol ($FCHC_{4.97Å}$)**: The surface is composed of n-perfluorodecanethiol molecules arranged in a hexagonal close packed lattice with lattice spacing of 4.97Å corresponding to the hydrocarbon packing density but with charge on F atoms equal to the charge on hydrocarbon H atoms (i.e. 0.06e) and charges on hydrocarbon C atom adjusted to make each CF_2 and CF_3 group neutral.
6. **Densely Packed Reverse Charged Perfluorodecanethiol ($FCRC_{4.97Å}$)**: The surface is composed of n-perfluorodecanethiol molecules arranged in a hexagonal close packed lattice with lattice spacing of 4.97Å corresponding to the hydrocarbon packing density but with charge on F atoms and C atoms having the same magnitude as that on the corresponding atoms of the fluorocarbon but with the *signs reversed.*

5.3 Results and Discussion

We present our results in tabular as well as graphical form. Table 5.2 shows the results of the free-energy calculations described in section 5.2.1. The data is shown graphically in Figure 5.3. The various quantities associated with the various states (see section 5.2.1.2) appear in Figure 5.4 and Table 5.3. Contact angle results appear in Table 5.4 and Figure 5.5.

We will begin with a validation of our simulation results by comparing with relevant experimental observations. Then we will interpret each set of calculations separately before pointing out the unifiying aspect. We will also comment briefly on a number of other observations that can be explained with our insights.

5.3.1 Validation of Results

We will briefly demonstrate the consistency of our calculations with experimental observations. This allows us a greater measure of confidence in the simulations with which to draw our conclusions.

5.3.1.1 Validation of free energy calculations

From the Table 5.2 we can see that the difference in solvation free energy between perfluorooctane and n-octane in water at 298.16K at ~3000atm is 6.71±0.18 kcal/mol. Now there is no direct empirical validation of this number since perfluorooctane's solubility has not been measured at these conditions. However, the solubilities of normal and perfluorinated methane, ethane and propane are measured at 1 atm. We will use these results to extrapolate the empirical difference in solvation free energy between octane and perfluorooctane at 3000 atm. We can do so because the solubility parameters of water at 298.16K and 1 atm and 3000 atm are close at 47.9 $(J/cm^3)^{0.5}$ and 50.6 $(J/cm^3)^{0.5}$ respectively (http://webbook.nist.gov/chemistry/fluid/) (Allada, 1984) and therefore the *difference* in solubility/hydration-energy will be comparable at 1 atm and 3000 atm. Also, since all our transformations are at constant volume, we do no pressure-volume work.

Experimental data are reported in the form of Henry Law constants (denoted by K) where pressure (P) in the gas phase of the solute is related to its mole fraction (x_s) in liquid (at very high dilution) by $P=Kx_s$. At very low pressures, the gas phase may be assumed ideal so that $P=\rho_g RT$ (where ρ_g is the gas phase molar density, R the universal gas constant and T the temperature). Since $x_s \rightarrow 0$, the molar density in the liquid (water) phase may be calculated simply as $\rho_l=x_s\,\rho_w$ (where ρ_l is the molar density of the solute and ρ_w that of water). Hence, $\rho_g RT = K\frac{\rho_l}{\rho_w} \Rightarrow \frac{\rho_l}{\rho_g} = \frac{\rho_w RT}{K}$. Now at equilibrium, $\frac{\rho_l}{\rho_g} = \exp\left(\frac{\mu_g^{ex} - \mu_l^{ex}}{RT}\right)$ where μ_l^{ex} and μ_g^{ex} are the excess chemical potentials of the solute in solution and in gas respectively so that for a single molecule (see Figure 5.1) $F_{(solv)} = \mu_l^{ex} - \mu_g^{ex}$. Hence, $F_{(solv)} = RT\log\left(\frac{K}{\rho_w RT}\right)$ and hence, $\Delta F_{HC\rightarrow FC(solv)} = RT\log\left(\frac{K_{FC}}{K_{HC}}\right)$ where the subscript HC and FC refer to the hydrocarbon and fluorocarbon respectively.

From data for methane (Scharlin & Battino, 1995), ethane (Mohammadi, Chapoy, Tohidi, & Richon, 2004), propane (Chapoy, Mokraoui, Valtz, Richon, Mohammadi, & Tohidi, 2004) and for perfluoromethane, perfluoroethane and perfluoropropane (Wen & Muccitelli, 1979) we have, $\Delta F_{HC\rightarrow FC(solv)}^{CH_4} = 1.13$ kcal/mol, $\Delta F_{HC\rightarrow FC(solv)}^{C_2H_6} = 2.01$ kcal/mol and $\Delta F_{HC\rightarrow FC(solv)}^{C_3H_8} = 2.85$ kcal/mol. Fitting to a power law curve, we get $\Delta F_{HC\rightarrow FC(solv)}^{C_nH_{2n+2}} = 1.13n^{0.83} \Rightarrow \Delta F_{HC\rightarrow FC(solv)}^{C_8H_{18}} = 6.48$ kcal/mol (for n=8) which is in very good agreement with the result from the simulations.

Alternatively, from the difference in ethane and propane values, we can get the contribution of the methylene group as $\Delta F_{HC\rightarrow FC(solv)}^{CH_2} = 0.84$ kcal/mol. Adding five of these to propane gives

$\Delta F_{HC\rightarrow FC(solv)}^{C_8H_{18}} = \Delta F_{HC\rightarrow FC(solv)}^{C_3H_8} + 5\Delta F_{HC\rightarrow FC(solv)}^{CH_2} = 7.05$ kcal/mol, still in good agreement with simulation.

5.3.1.2 Validation of Contact Angle Calculations

The empirical data for contact angles comes entirely from the work by Graupe et al (1999) (Graupe, Takenaga, Thomas, Colorado Jr, & Lee, 1999) done on self-assembled monolayers of hexadecanethiol (fluorinated to varying degrees) on Au(111). The length of the thiol ensures that the underlying substrate does not influence the contact angle. The result for the CF_3 tipped hexadecane-thiol gives an empirical datapoint for our case 4 (labeled **FC$_{4.97Å}$,** see section 5.2.2.3). Their result for unfluorinated hexadecane thiol corresponds to case 1 (labeled **HC$_{4.97Å}$**) and their highly fluorinated result corresponds to case 2 (labeled **FC$_{5.90Å}$**).

For each case, in Table 5.4, the result of all four ways of calculating contact angle (described in section 5.2.2.2.1) are reported. It is clear that the definition $\theta_{z_o+d}^{circle}$ matches experimental data very closely while $\theta_{z_o+d}^{polyfit}$ match satisfactorily. However, the angles $\theta_{z_o}^{polyfit}$ are very different. The angle $\theta_{z_o}^{circle}$ - which is recommended by some other works (Werder, Walther, Jaffe, Halicioglu, & Koumoutsakos, 2003) (Hrivi & Pakkanen, 2006) - gives values much higher than experiment.

To account for droplet size dependence, the concept of a *line-tension* (Duncan, Li, Gaydos, & Neumann, 1995)was introduced so that

$$\cos\theta_{z_o}^{circle} = \cos\theta_{z_o,\infty}^{circle} - \frac{\tau}{\gamma_{LV}}\frac{1}{r_B} \qquad \text{… (5.4)}$$

Where $\theta_{z_o,\infty}^{circle}$ is the angle actually measured for a macroscopic droplet, τ is the line tension, γ_{LV} is the vapour-liquid surface tension and r_B is the droplet base diameter. Hence for $r_B \rightarrow \infty$,

$\cos\theta_{z_o}^{circle} \to \cos\theta_{z_o,\infty}^{circle}$. We note from our results that $\theta_{z_o,\infty}^{circle} \sim \theta_{z_o+d}^{circle}$. This insight we will now incorporate into the formulation of line-tension.

To express $\theta_{z_o}^{circle}$ in terms of $\theta_{z_o+d}^{circle}$, we note that the radius of the circle *R* is the same for both cases. What differs is the distance of the base circle from the centerline. If *h* is the distance from the centre of the droplet to the solid-liquid interface (see cartoon in Figure 5.2a) then *h-d* is the distance from the centre of the droplet to the boundary of the layered-water region. Hence $\cos\theta_{z_o}^{circle} = -\frac{h}{R}$ and $\cos\theta_{z_o+d}^{circle} = -\frac{h-d}{R}$ so that $\cos\theta_{z_o}^{circle} = \cos\theta_{z_o+d}^{circle} - \frac{d}{R}$. Hence using $r_B = R\sin\theta_{z_o+d}^{circle}$, we have,

$$\cos\theta_{z_o}^{circle} = \cos\theta_{z_o+d}^{circle} - \frac{d\sin\theta_{z_o+d}^{circle}}{r_B} \qquad \text{… (5.5)}$$

Which is the same form as equation 5.4 if the droplet radius is large enough, the contact angles $\theta_{z_o+d}^{circle} = \theta_{z_o,\infty}^{circle}$. Accepting this relationship implies that the macroscopic contact angle is accessible without having to calculate line tensions. This is a great convenience, since line tensions are computationally intensive to calculate (via simulations of contact angle with several different droplet volumes) and are rather poorly defined (Vafaei & Podowski, 2005) (Amirfazli & Neumann, 2004).

Hence the line tension can be expressed in terms of the thickness of the layered region as:

$$\tau = \gamma_{LV} d\sin\theta_{z_o+d}^{circle} \qquad \text{… (5.6)}$$

Using γ_{LV} =0.073 N/m for water at 298.16K (BYU DIPPR Thermophysical Properties Laboratory) we have calculated line tension values and reported them in Table 5.4. The order of magnitude is 10^{-11}N. This is consistent with the results for simulations of water on polyethylene surfaces (Hrivi & Pakkanen, 2006) which system is the closest analogue to our system for which we found data. An empirical study of water on an alkanethiol self-assembled monolayer found line tensions to be of the order of 10^{-8}-10^{-7}N (Preuss & Butt, 1998) but the results can be questioned since the *receding* contact-angle was used for all calculations although it has been argued that only the advancing contact angle is meaningful for a theoretical analysis (Amirfazli & Neumann, 2004).

5.3.2 Discussion

5.3.2.1 Hydrocarbon to Fluorocarbon

We have organized our discussion of the free-energy difference according to the various intermediate transformations. For each stage, we have calculated the solvation free-energy change (ΔF) and the solvation energy change (ΔU) and hence we can get the contribution due to change in entropy (-T ΔS) from ΔF= ΔU-T ΔS. We obtain acceptable uncertainties as a result of our long simulations (see above) comprised of 20ns per stage. The thermodynamic quantities are in Figure 5.3 and their cumulative values are in Figure 5.4a. For each end-state we calculate the structural parameters: (a) Molecular Surface Area (MSA, Figure 5.4b), (b) Solvent Excluded Volume (Vex, Figure 5.4c), (c) Solute End-to-End distance ("dee", Figure 5.4d), (d) Orientational distribution of O→H for water molecules closest to terminal carbon atoms (Figure 5.4e), (e) Most probable radial position of nearest solvent O atom from terminal and the middle-chain C atoms (r_{peak}O, Figure 5.4f).

5.3.2.1.1 Solvent orientation about solute

The plot of $P(\cos\theta_{C\text{-}O\text{-}H})$ vs. $\cos\theta_{C\text{-}O\text{-}H}$ is flat (uniform) if the solvent has no preferred orientation. Hence the distinct maxima in the plot (see Figure 5.4e) indicate definite orientational influences from the solute though the broadness of the peaks implies considerable fluctuation. The acute-angle peak occurs at the bin corresponding to $\cos\theta_{C\text{-}O\text{-}H}\sim 0.995$ (binwidth 0.01) so that the $\theta_{C\text{-}O\text{-}H}$ for acute angled peak is between 0 and 8.2^o i.e. the O→H vector of a solvating water molecule is pointed almost radially outward from the solute. This is as would be expected with a clathrate structure (Blokzijl & Engberts, 1993). This geometry allows water to substantially maintain its hydrogen bond structure and is consistent with other investigations (Zichi & Rossky, 1985) (Cheng & Rossky, 1998). One could then expect the obtuse angle peak to be between 109.5^o and 117.7^o since the rigid angle H-O-H in SPC/E water is 109.5^o and consistently, the second peak is at $\theta_{C\text{-}O\text{-}H} \sim 116^o$. The striking attribute of the behavior of the orientation of water about the solute is that it is practically *unaffected* by the variation of the solute.

5.3.2.1.2 Transformation Stages

We will now present an analysis of the various transformation stages that are involved in the conversion of a hydrocarbon molecule to a fluorocarbon molecule.

State 0 → State 1 (Stiffening):

As we can see from Table 5.2 and Figure 5.3, the free energy change associated with this is small and positive. The solute is stiffer and hence straighter as can be seen from the increased end-to-end distance (Figure 5.4d). It also offers slightly higher surface area (Figure 5.4b) to solvent and excludes solvent from a slightly higher volume (Figure 5.4c). However around the terminal and central carbon atoms, $r_{peak}O$ actually decreases (Figure 5.4f) implying that the excluded volume increase is due to reduced overlap of excluded volumes of adjacent chain segments when the molecule straightens out. This also implies that the transition is energetically unfavourable because the less flexible molecule cannot conform to a shape that allows better interaction between the system particles. The transition is correspondingly more entropically favourable and this offsets the effect of the higher excluded volume.

State 1 → State 2 (Fattening):

There is a considerable unfavourable free energy change associated with this transition and it is mostly entropic . This is principally due to the increase in the excluded volume and the higher stiffness (hence higher end-to-end distance) of the solute – both of which are due to a higher value of the Lennard-Jones σ parameter of the H atoms of the solute. The transition is energetically favourable, most likely due to an increased number of water molecules within the increased interaction-range of the solute.

State2 → State 3 (Lengthening):

Here too the free energy change is unfavourable but the unfavourable interactions are both entropic (increase due to increased excluded volume making up for the *decrease* in stiffness) and energetic (longer C-H bond reduces dispersion interaction between solvent and C atoms of solute). The longer C-H bond also reduces the steric hindrance to rotation of the dihedrals allowing a more flexible backbone – as evidenced by a lower end-to-end distance.

State 3 → State 4 (Strengthening):

The increase in the LJ energy (ε) parameter of the H atoms of solute leads to increased attractive interactions with solvent. It also has the effect of “hardening” the atoms resulting is a net *increase* in solvent excluded volume (indicated by increased $r_{peak}O$) and stiffness (indicated by higher end-to-end distance). This together with the entropy loss that invariably accompanies energetic stabilization results in an unfavourable entropic contribution to an overall very favourable free energy change.

State 4 → State 5 (Charging):

The change in charge on the outer atoms (H/F) of the solute from weakly positive to strongly negative (with corresponding change in C atom charges) is also a favourable transition with respect to free-energy albeit less so than the “strengthening” transition. However, this is because a very favourable energetic change is offset by a very unfavourable entropic change. Furthermore, comparing electrostatic energy $\Delta U_{ss(coul)}$ and Lennard-Jones energy $\Delta U_{ss(lj)}$ (see Table 5.2) contributions, we see that this favourable energetic change arises from the coulombic interactions rather than from the 6-12 interactions, which are actually unfavourable; the latter reflects the compression of the solvent atoms against the soft-cores of the solute atoms. From $r_{peak}O$ we can see that the excluded volume actually decreases slightly so that the unfavourable entropy is not due to volume denial. It is instead restriction of solvent by electrostatics and also due to the Born charging of the solute in a dielectric medium. The decrease in $r_{peak}O$ in spite of the repulsive interaction between the negatively charged surface and negatively charged O can be explained by noting that one of the H atoms (positively charged) of the associated water molecule is actually *nearer* the solute than the O atom is and also the H atom of an adjacent solvent molecule is hydrogen-bonded with the O atom. Hence the resulting dipole moment is such that it interacts *favourably* with the solute surface.

Note that if we were to combine the effect of fattening and strengthening into one stage (associated with change in LJ parameters) the free energy change would be 4.906-2.131 = 2.775 kcal/mol (see Table 5.2) which is about half the change associated with bond-lengthening (5.013 kcal/mol).

5.3.2.2 Contact Angle

When comparing the cases $FC_{4.97Å}$, $FCHC_{4.97Å}$ and $FCRC_{4.94Å}$ or the cases $FC_{5.9Å}$ and $FCHC_{5.9Å}$ (see Table 5.4 and Figure 5.5) we see the rather weak dependence on electrostatics. This is consistent with the observation of Graupe et al (1999) (Graupe, Takenaga, Thomas, Colorado Jr, & Lee, 1999) that contact angles of protic solvents are substantially independent of the polarity of the surface while those of polar aprotic solvents were very sensitive to it.

Also, the contact angles correlate very well with the *Lennard-Jones* interactions of water with the surface. This implies that the only reason a fluorocarbon self-assembled monolayer is more hydrophobic than the hydrocarbon self-assembled monolayer is that the fluorocarbon ligands pack more sparsely (lattice spacing of 5.9Å) on the surface than the hydrocarbons (lattice spacing of 4.97Å) and the more attractive van der Waals interactions due to F atom over H atom cannot offset the reduction in interactions due to lower density of interaction sites.

If the fluorocarbon were to pack with the same density as the hydrocarbons, the resulting contact angle would be lower than in case of the hydrocarbon – as we see with the contact angle increase from $FC_{4.97Å} < HC_{4.97Å} < FC_{5.9Å}$.

From the orientational distributions (Figure 5.5c,d) it is clear that the structure of water is substantially independent of the nature of the surface for hydrophobic surfaces. However, there are interesting variations. From Figure 5.5c we see that the orientation of water molecules closest to the solid-liquid interface ($z<z_o$) is a *reverse* clathrate type with one O→H vector pointed straight into the surface (there is a peak at $\cos\theta_{v(zo)}$~-1) while the other vector is nearly tangent to it. This is consistent with what would be expected from a planar hydrophobic surface (Lee, McCammon, & Rossky, 1984). Also expected is the reversal in orientation for the layer centered on the first density maximum z_{peak1} (see Figure 5.5d) where orientation is clathrate-like. For the layer centered on z_{peak2} (not shown) the orientation is once again reverse-clathrate but the peaks are less pronounced. For $z>z_o+d$, the orientational distribution is essentially flat.

What is rather counter-intuitive about Figure 5.5c is that as the charge on the outermost atoms of the surface is changed from negative (for fluorocarbons) to positive (hydrocarbons and reverse charged fluorocarbons), the peak for the inward pointing orientation actually becomes *more* pronounced. However, this is consistent with the explanation of water orientation at hydrophobic interfaces presented by Lee et al (1984) (Lee, McCammon, & Rossky, 1984). The reverse-clathrate structure is a result of the tendency of water molecules to maximize hydrogen-bonded interactions. One interpretation is that the partial negative charge on the solid surface allows favourable electrostatic interactions with the inward pointed O→H dipole – reducing the drive to maintain the hydrogen-bonded network and allowing water greater configurational freedom which results in less pronounced peaks in the orientational distribution. The more positive is the partial charge on the surface, the more repulsive is the coulombic interaction with the water molecules' H atoms and the greater is the drive to maintain the energetically favourable hydrogen-bonded network resulting in lowered configurational freedom and more pronounced peaks in orientational distributions.

5.3.2.3 Miscellaneous

We will now comment on other problems to which insights gained here might be applicable.

5.3.2.3.1 Carbon Dioxide

Fluorocarbons are more CO_2 philic then hydrocarbons because the free energy penalty that has to be paid in the "fattening" and "lengthening" stages is probably (we have done no calculations to back this up) more than offset by the free-energy reduction in the latter two stages. This is consistent with the fact that the cohesive energy density of liquid water (47.9 $(J/cm^3)^{0.5}$ at 298.16K and 1 atm and 50.6 $(J/cm^3)^{0.5}$ at 3000atm) is much higher than that of carbon-dioxide (16.3 $(J/cm^3)^{0.5}$ at 298.16K and 500atm and 20.8$(J/cm^3)^{0.5}$ at 3000 atm) (http://webbook.nist.gov/chemistry/fluid/) making work of cavity formation in CO_2 much lower than in water. From the work of Graupe et al (1999) we see that polar aprotic solvents respond more strongly to electrostatics than do protic solvents. Hence the "charging" step in carbon-dioxide (with its strong quadrupole) should give a correspondingly greater free-energy benefit.

5.3.2.3.2 Super-hydrophobic Surfaces

From the analysis of the contact angles, it is clear that hydrophobicity is governed almost exclusively by the density of Lennard-Jones centers on the surfaces. This is substantially due to the strong inclination of water molecules to maintain their hydrogen-bonded network. Hence nano-roughened surfaces are superhydrophobic (Nosonovsky & Bhushan, 2009) because the roughness reduces density of LJ centers at the solid-liquid interface while the desire to maintain hydrogen bonding prevents water from taking advantage of the increased accessible surface area. This also suggests that self-assembled monolayers of two-tailed ligands with one short and bulky tail and the other tail ~4 C atoms longer may produce a superhydrophobic surface since the short, bulky tail would force sparse surface coverage while the longer tail would impart roughness to the surface.

5.3.2.3.3 Surfactant Design

A problem in the design of surfactants (Rosen, 1972) is the compromise between *efficiency* (also characterized by critical micelle concentration or CMC i.e. amount of surfactant required to saturate the interface and hence appreciably lower surface tension) and *effectiveness* (degree of reduction of surface tension at CMC). Hydrocarbon surfactants with long-chain alkyl tails are more hydrophobic and hence have higher efficiency than their isomers with branched tails. However, due to the higher cohesiveness of the adsorbed layer, their *effectiveness* is lower. Surfactants with perfluorinated alkyl tails however are much more effective *and* efficient (Mukerjee & Handa, 1981) than the corresponding hydrocarbon surfactants because they are more hydrophobic *and* they have a lower cohesiveness. An interesting result from the solvation calculations is that a solute may have *polar* moieties and still be hydrophobic if its solvent-excluded volume is large enough. Hence surfactants for water-in-CO_2 can have the hydrophilic-CO_2philic balance in their tails adjusted by increasing polar moieties for CO_2-philicity while increasing solvent excluded volume for hydrophobicity (Dickson, et al., 2005).

5.4 Conclusion

We have conducted simulations to determine the molecular sources of the difference in hydration free energy between hydrocarbons and fluorocarbons using n-octane and n-perfluorooctane to respresent each category. To isolate the effect of surface, we also carried out contact-angle simulations of water droplets over a self-assembled monolayer composed of hydrocarbon or fluorocarbon ligands. Our results for solvation free energy as well as contact angle are consistent with experimental observations. We have found that the greater hydrophobicity of fluorocarbons over hydrocarbons across geometries is not related to its energetic affinity for water but rather to its size. A fluorinated solute and a fluorinated SAM are both more hydrophobic than a hydrocarbon solute and a hydrocarbon SAM simply because they are “fatter” i.e. have greater molecular cross-sectional area. We have also found that due to the strong tendency of water to minimize disruptions to its hydrogen bonded network, the structure of water is essentially refractory to the electrostatic nature of hydrophobic solutes/surfaces and free-energy of hydration of these surfaces is much more responsive to changes in Lennard-Jones interactions than to electrostatic interactions. However, we did not see any evidence of polar-hydrophobicity in fluorocarbons. From these results, we have been able to explain the high CO_2-philicity and surface activity (in water) of fluorinated hydrocarbons. Additionally, we have also been able to tentatively correlate the line tension of fluid droplets with the microscopic phenomena at the interface.

Transformation Stage	Coupled Parameters	Initial value	Final value
Stiffening	Harmonic angle potentials	OPLS values for alkanes	OPLS values for perfluoroalkanes
	Dihedral potentials		
Fattening	H atom LJ diameter σ	2.5Å	2.95Å
Lengthening	C-H bond equilibrium length	1.09Å	1.332Å
	C-H bond stiffness	680.0 kcal/mol/Å^2	734.0 kcal/mol/Å^2
Strengthening	H atom LJ energy parameter ε	0.03 kcal/mol	0.053 kcal/mol
Charging	Charge on H of CH_3	0.06e	-0.17e
	Charge on C of CH_3	-0.18e	0.51e
	Charge on H of CH_2	0.06e	-0.12e
	Charge on C of CH_2	-0.12e	0.24e

Table 5.1: Tabulation of the various stages in the transformation of n-octane molecule to n-perfluorooctane at 298.16K in either vacuum or in liquid water at ~3000 atm. This is in support of the text in section 5.2.1.2. We do not report the large number of stiffening values; we have used the standard OPLS values.

Stage	**ΔF**	**ΔU**	**-TΔS**	**$\Delta U_{ss(coul)}$**	**$\Delta U_{ss(lj)}$**
	(kcal/mol)	*(kcal/mol)*	*(kcal/mol)*	*(kcal/mol)*	*(kcal/mol)*
Stiffening	0.02 (0.13)	0.40 (0.36)	-0.38 (0.39)	0.02	-0.07
Fattening	*4.21 (0.06)*	*-1.27 (0.24)*	*5.48 (0.25)*	0.06	-0.48
Lengthening	*5.74 (0.09)*	*2.85 (0.25)*	*2.88 (0.27)*	0.25	1.88
Strengthening	-2.13 (0.02)	-3.49 (0.60)	1.36 (0.61)	0.03	-3.55
Charging	-1.13 (0.03)	-4.21 (0.61)	3.08 (0.61)	-3.87	0.04
Final	6.71(0.18)	-5.71(1.00)	12.42(1.01)	-3.52	-2.18
With order of Fattening and Lengthening stages interchanged					
Lengthening	*5.01 (0.07)*	*1.15 (0.17)*	*3.86 (0.18)*		
Fattening	*4.91 (0.04)*	*0.43 (0.18)*	*4.47 (0.18)*		
Final	6.68(0.16)	-5.71(0.97)	12.39(0.98)		

Table 5.2: Tabulated values of various parameters related to the change in water-solvation properties (298.16K and ~3000atm) associated with the various transformation stages described in section 5.2.1.2 and depicted graphically in Figure 5.3. ΔF is the change in the solvation free energy. ΔU, –TΔS, $\Delta U_{ss(coul)}$, $\Delta U_{ss(lj)}$ are the corresponding contributions due to changes in internal energy, entropy, solvent-solute coulombic interactions and solvent-solute dispersion interactions respectively. The errors associated with each quantity are shown in (). The entries in the rows headed by "***Final***" represent the sum of all the intermediate changes i.e. the difference between the solvation properties of the hydrocarbon and the fluorocarbon.

State	**ΔF_{cum}**	**ΔU_{cum}**	**dee**	**MSA**	**Vex**	**r_{peak}O (terminal)**	**r_{peak}O (central)**
	kcal/mol	*kcal/mol*	*Å*	*$Å^2$*	*$Å^3$*	*Å*	*Å*
0	0.000	0.000	8.465	378.7	1074.3	3.73	4.45
1	0.019	0.400	8.768	380.7	1079.0	3.69	4.38
2	4.229	-0.870	9.143	422.9	1332.2	3.97	4.59
3	9.968	1.985	9.054	449.1	1429.2	4.14	5.04
4	7.838	-1.502	9.085	452.1	1437.0	4.17	5.13
5	6.707	-5.710	9.185	451.8	1436.7	4.15	5.01

Table 5.3: Tabulation corresponding to the various quantities depicted in **Figure 5.4**. ***ΔF_{cum}*** is the difference in free energy between State *i* and State 0. ***ΔU_{cum}*** is the corresponding difference in energy. ***dee*** is the distance between the two terminal carbon atoms of the solute in a given state, **MSA** is the molecular surface area and **Vex** is the solute excluded volume (see section 5.2.1.4). **r_{peak}O(terminal)** is the radial distance corresponding to the position of the first peak in a pair distribution function between terminal carbon atom of solute and oxygen of water. **r_{peak}O(central)** is the same quantity for the middle-chain carbon atoms of the solute.

Case	**$U_{sl(coul)}$**	**$U_{sl(LJ)}$**	**d**	$\theta_{z_o}^{circle}$	$\theta_{z_o}^{polyfit}$	$\theta_{z_o+d}^{circle}$	$\theta_{z_o+d}^{polyfit}$	**Expt.**	**τ**
	(kcal/mol)	*(kcal/mol)*	*(Å)*						*(N)x10^{11}*
$HC_{4.97Å}$	33.49	-372.81	4.714	130^{o}	142^{o}	118^{o}	118^{o}	116^{o}	3.04
$FC_{5.90Å}$	-83.95	-273.71	5.587	140^{o}	150^{o}	124^{o}	120^{o}	126^{o}	3.39
$FCHC_{5.90Å}$	24.29	-269.32	5.498	139^{o}	146^{o}	123^{o}	120^{o}		3.35
$FC_{4.97Å}$	-135.69	-469.24	5.667	124^{o}	157^{o}	111^{o}	112^{o}	110^{o} *	3.87
$FCHC_{4.97Å}$	43.57	-462.51	5.392	122^{o}	154^{o}	110^{o}	113^{o}		3.70
$FCRC_{4.97Å}$	118.19	-454.77	6.131	123^{o}	156^{o}	109^{o}	110^{o}		4.22

*** -** Value is for CF_3 terminated hexadecanethiol.

Table 5.4: Tabulation of quantities related to contact angle calculations. $U_{sl(coul)}$ and $U_{sl(LJ)}$ are the coulombic and Lennard Jones (respectively) contributions to the interaction energies of water with the surface. *d* is the thickness of the layered region of solvent at the solid-liquid interface. The various θs are defined as described in section 5.2.2.2.1 for the cases described in section 5.2.2.3. The experimental values are taken from Graupe et al (1999) **(Graupe, Takenaga, Thomas, Colorado Jr, & Lee, 1999)** and are for hexadecanethiol/perfluorohexadecanethiol. τ is the line tension calculated using equation 5.6.

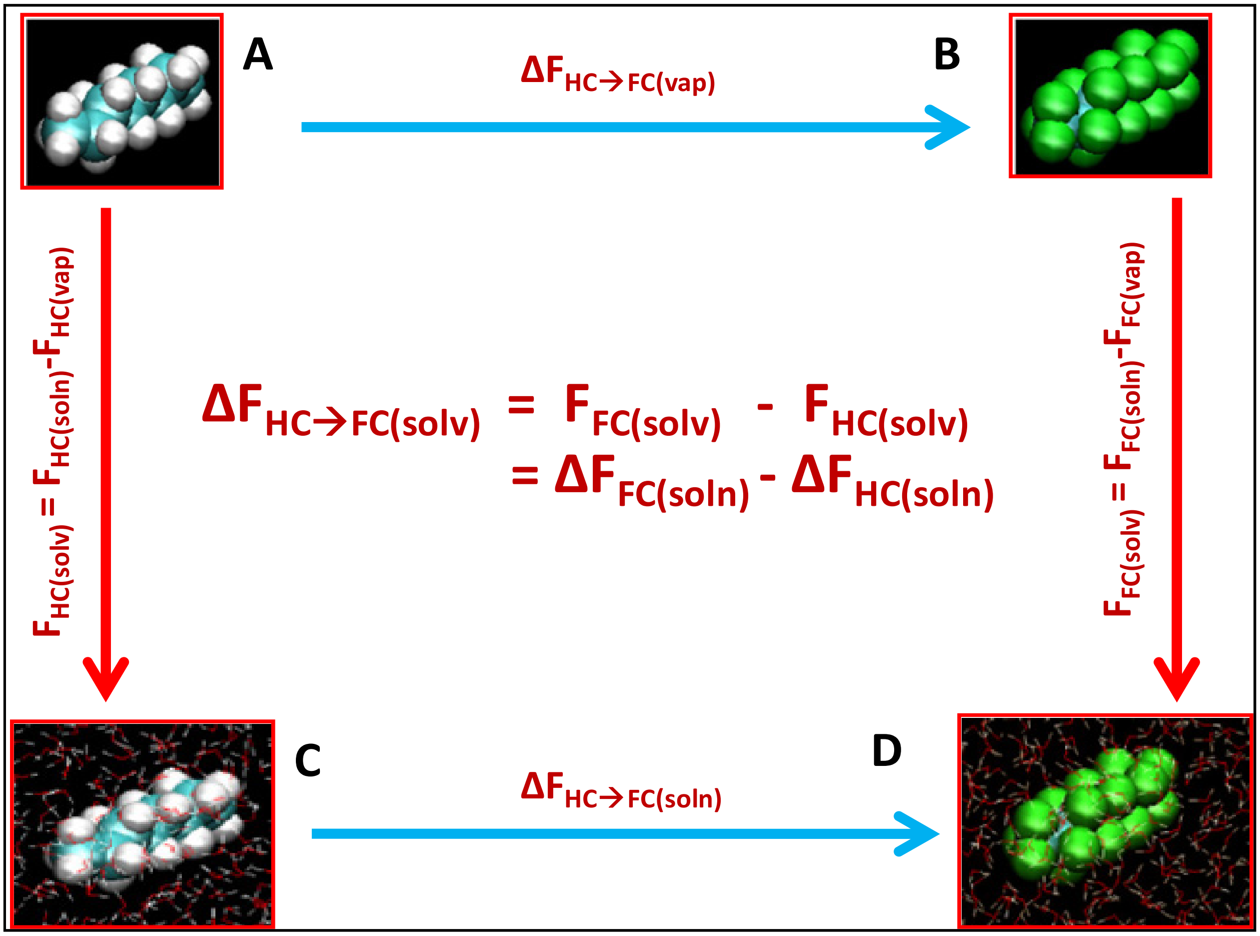

Figure 5.1: Cartoon illustrating the thermodynamic cycle behind the simulation strategy to determine the difference in solvation free energy between n-octane (CH_3-CH_2-CH_2-CH_2-CH_2-CH_2-CH_2-CH_3, hydrocarbon or HC) and n-perfluorooctane (CF_3-CF_2-CF_2-CF_2-CF_2-CF_2-CF_2-CF_3, fluorocarbon or FC). This quantity is $\Delta F_{HC \rightarrow FC(solv)}$. The states A and B are the hydrocarbon and fluorocarbon respectively in vacuum i.e. vapour phase designated by subscript *vap*. The states C and D are the hydrocarbon and fluorocarbon respectively in solution by liquid water at 3000 atm pressure i.e. in solution phase which is designated by the subscript *soln*. The temperature is 298.16K. The vertical transitions (A→C and B→D) show the transition from vapour phase to solution phase and the difference in free energies of these two transitions is the quantity of interest. The same number can be obtained with greater facility by taking the difference between the horizontal transitions (C→D and A→B) since these can be calculated using simulations in a fluid bulk.

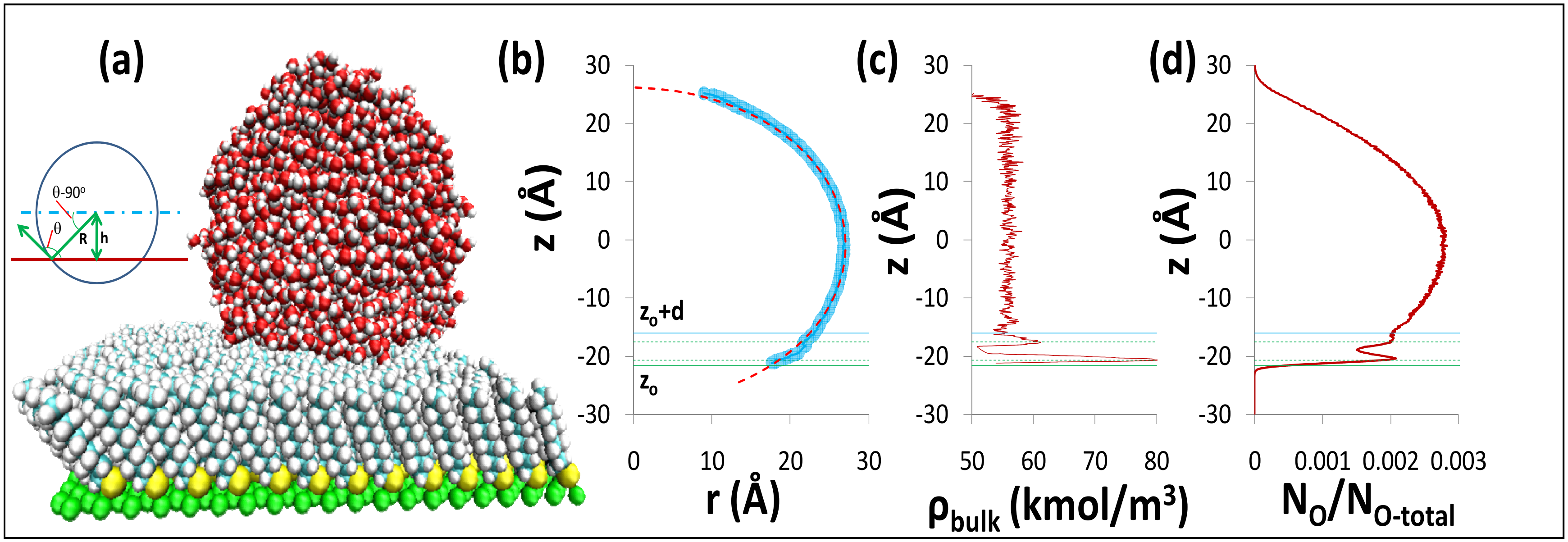

Figure 5.2: A set of figures to illustrate the calculation of contact angles. (a) A VMD visualization of a typical system setup. Here, using space-filling models, a water droplet is shown in contact with perfluorodecanethiol self-assembled-monolayer (lattice spacing of 5.9Å) after 3ns of simulation time. Also shown is a sketch illustrating the meaning of contact-angle (θ). (b) The profile of the liquid-vapour interface of the water droplet (about its centre of mass averaged over 4000 snapshots each 0.5ps apart) is shown as ● with the *z* position of a horizontal cross-section of the droplet plotted against the radius (*r*) of that cross section. The broken line (▬ ▬ ▬ ▬ ▬ ▬) is the result of the points fitted to a circle (see equation 5.2a). The lowermost solid horizontal line (▬▬▬▬▬▬) represents the height z_o at which represents the lowermost boundary of the water droplet (as explained in section 5.2.2.2). The uppermost solid horizontal line (▬▬▬▬▬▬) is the height (z_o+d, see equation 5.3) at which the water in the droplet can be said to have attained its bulk density. Hence we have four different ways of defining the contact angle (see section 5.2.2.2). The broken horizontal lines in between represent the positions of the first and second peak in the density profile of water. (c) The profile of the density of water near the center of the droplet as a function of *z* position. It is structured at, and near the solid-liquid interface but quickly attains its limiting value with increasing z. The horizontal lines are the same as for figure b. (d) The fraction of the number of O atoms in the droplet encountered in a *z*-direction slice 0.1Å wide. The horizontal lines are the same as for figure b.

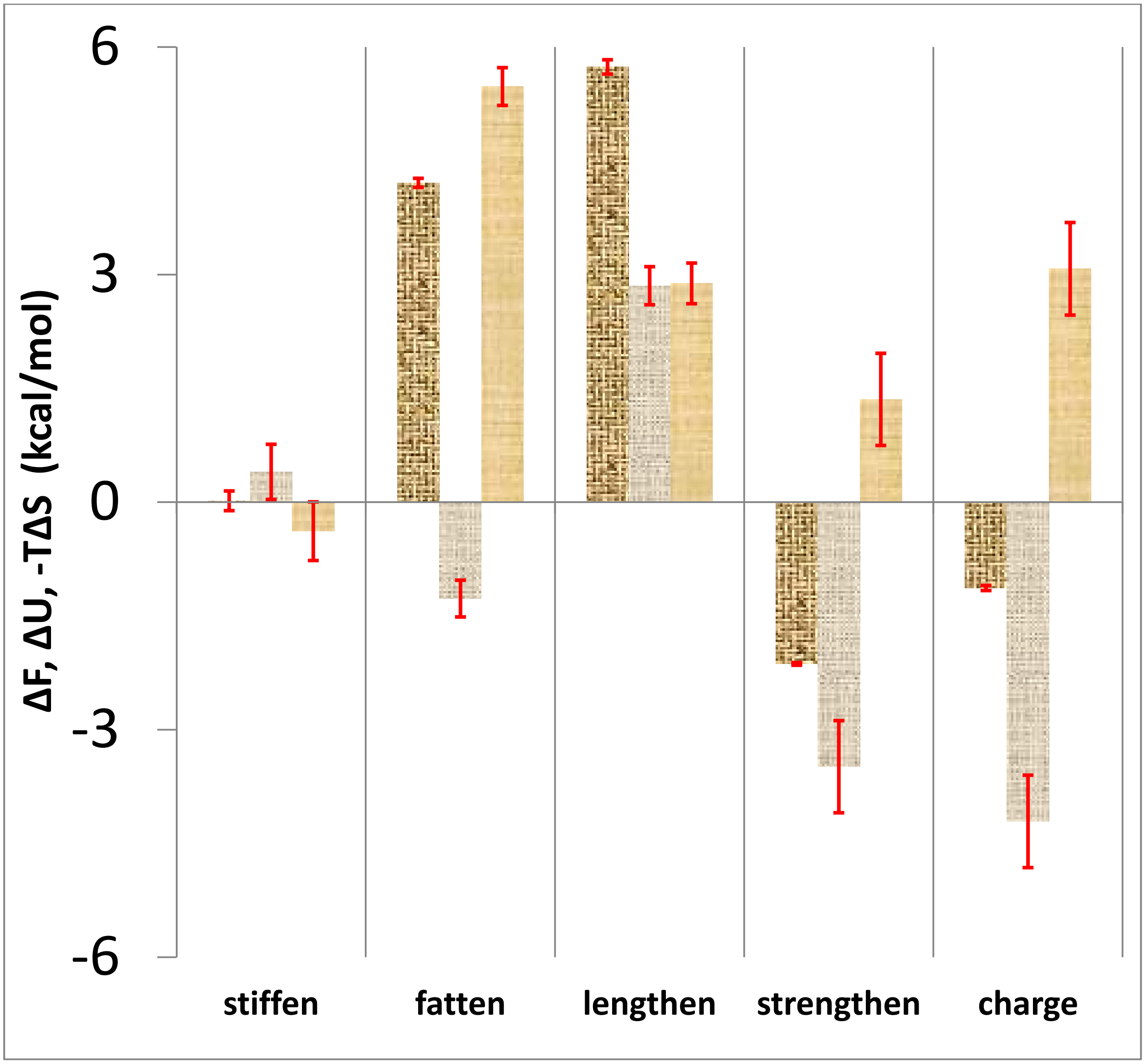

Figure 5.3: Thermodynamic quantities associated with the change in water-solvated (298.16K and ~3000atm) interactions corresponding to the transitions/stages described in section 5.2.1.2. ΔF (first column of each set ▦) is the change in the solvation free energy. ΔU (second column of each set ▤) and –TΔS (third column of each set □) are the corresponding contributions due to changes in internal energy and entropy respectively. The numbers corresponding to the above chart appear in **Table 5.2**.

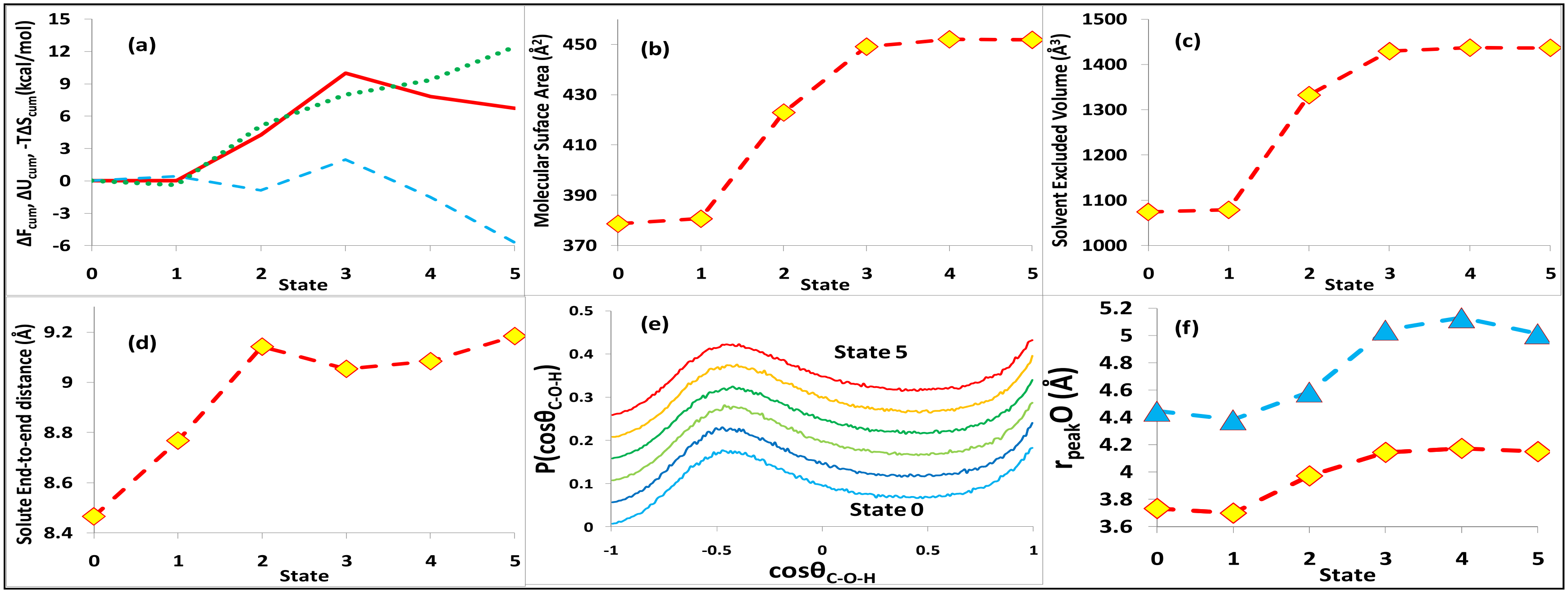

Figure 5.4: Plots of various quantities of interest (corresponding to

Table 5.3). (a) Cumulative values of the change in free energy (ΔF_{cum}, ———) and the energetic (ΔU_{cum}, — — —) and entropic ($-T\Delta S_{cum}$, ••••••••••••) contributions to it for the various states described in section 5.2.1.2. ΔF_{cum} for a State *i* is to be understood as the difference in solvation free energy between State *i* and State 0. (b) Molecular surface area for the solute in various states (see section 5.2.1.4) (c) Solvent excluded volume for the various states (see section 5.2.1.4) (d) End-to-end distance i.e. separation between the terminal carbon atoms of the solute for the various states (e) Probability density of $\cos(\theta_{C\text{-}O\text{-}H})$ around the terminal carbon atoms for the different states (see section 5.2.1.4 for nomenclature). The distribution for State *i* is normalized and shifted vertically by 0.05 for clarity so that State 0 (bottom curve) is the unshifted normalized curve while the curve for State 5 (topmost curve) is normalized and shifted by 0.25. Only the solvent molecules where $\theta_{C\text{-}C'\text{-}O}<90^o$ and where $r_{C\text{-}O} < r_{peak}O+1.5$Å are included in the calculations since the probability density for larger distances are uniform. There are two peaks – one at $\cos(\theta_{C\text{-}O\text{-}H})$~1 (acute angle peak) and the other at $\cos(\theta_{C\text{-}O\text{-}H})$~-0.44 (obtuse angle peak). (f) the radial distance of the first peak in the pair distribution function between water-oxygen and terminal carbon atoms of solute (◆) and middle-chain carbon atoms of solute (▲) .

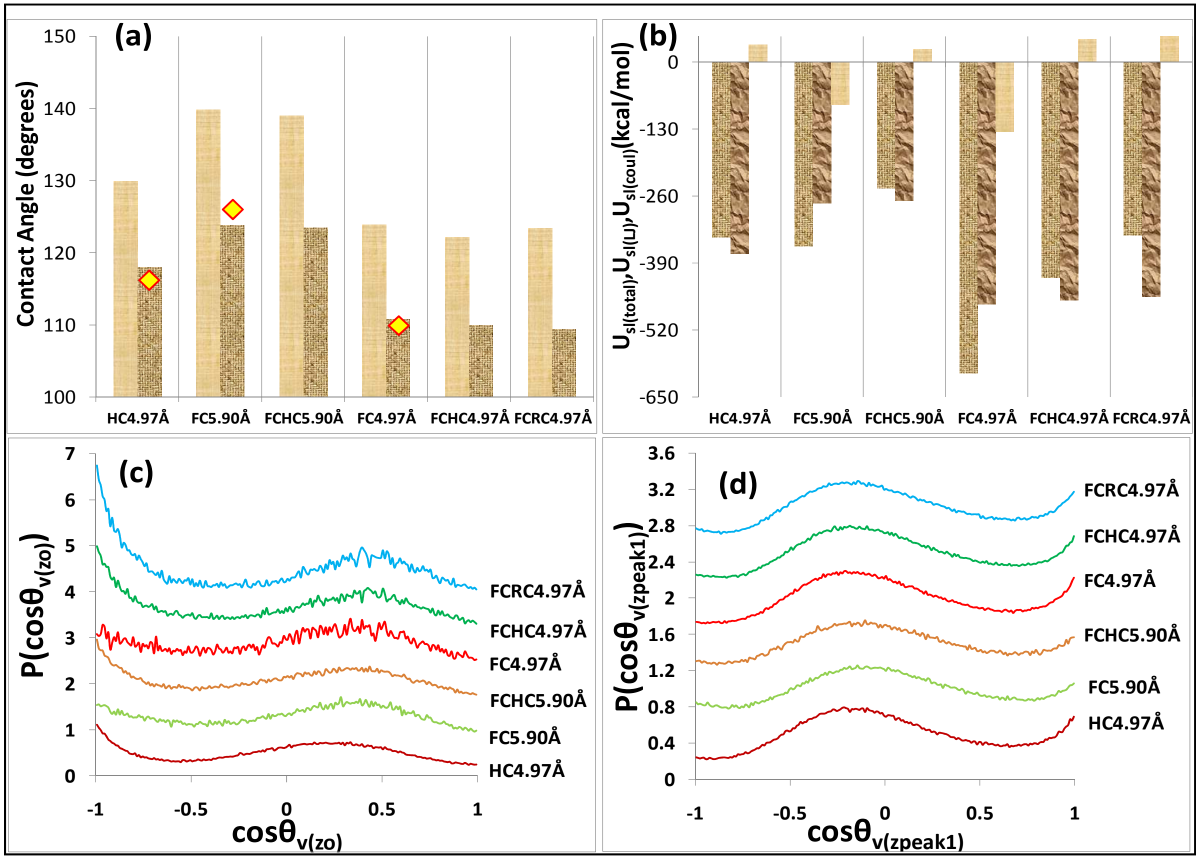

Figure 5.5: Graphs of data contained in **Table 5.4**. (a) Contact angle for the various cases described in section 5.2.2.3 using the definitions 3 ($\theta_{z_o}^{circle}$,left column) and definition 4 ($\theta_{z_o+d}^{circle}$,right column) as described in section 5.2.2.2.1. The diamonds are centered on the experimentally reported contact angles **(Graupe, Takenaga, Thomas, Colorado Jr, & Lee, 1999)**. (b) Water-surface interaction energies – $U_{sl)total)}$ (first column) is the total interaction energy, $U_{sl(disp)}$ (middle column) is that due to Lennard-Jones interactions and $U_{sl(coul)}$ (third column) is the energy due to coulombic interactions with the surface. It is apparent that the contact angles correlate very well with the Lennard-Jones interactions and very badly with the coulombic interaction. (c) Plots of the orientational distribution of water O→H vectors' angle with the vertical for water molecules at a *z* coordinate < z_o i.e. very close to the solid-liquid interface. (d) Plots of orientational distribution of water O→H vectors' angle with the vertical for water molecules at a *z* coordinate within 1Å of *zpeak1* i.e. at the first density maxima from the solid-liquid interface.

Chapter 6: Conclusions

We have developed a simulation protocol that yields molecular level insight into the physical phenomena related to the effectiveness of capping ligands in stabilizing nanoparticle dispersions. We have used this method first to study a number of ligand solvent systems and developed useful insights regarding design of surfactants to disperse solutes in supercritical CO_2. First, we have determined that hydrocarbon ligands are more effective in ethane due to due to a lower preference, by ethane, for its bulk over confinement compared to CO_2. Hence, ligands that interact with CO_2 more strongly should be more effective in stabilizing nanoparticle dispersions in supercritical $CO_{2.}$ We determined that the reason for the effectiveness of the fluorinated ligands in $ScCO_2$ was a combination of factors; the C-F dipole moment which interacts with the quadrupole of CO_2, a peculiar structure of fluoroalkanes that ensures that the C-F dipoles of two fluoroalkane molecules are always adverse, a relatively weak dispersive interactions of the fluorocarbons with each other due to sparser packing on the nanoparticle surfaces. All of these make surfaces passivated by pefluoroalkanes simultaneously CO_2-philic and less auto-philic. The insights obtained from this analysis can be used as design guides for non-fluorous ligands effective in $ScCO_2$. We have also suggested that experiments intended to find effective ligands should seek to probe ligand-behaviour *not* in an isotropic bulk system but in heterogenous conditions similar to the ligand-solvent interface of passivated nanoparticles. An investigation of "stubby" hydrocarbon ligands using isostearic acid as the model yielded the discovery that for hydrocarbon moieties there is an optimum packing density where the ligand is most effective, balancing dispersion interactions between particles with surface-solvent interactions and that this optimum is already attained in the partially effective isostearic acid thiol. Consequently, it does not seem likely that a ligand composed solely of aliphatic moieties would be effective in CO_2. Incorporation of oxygen in the ligand tips e.g. using alkoxy/siloxy tipped ligands is a more promising direction.

We have found that the greater hydrophobicity of fluorocarbons over hydrocarbons across geometries is not related to its energetic affinity for water but rather to its size. A fluorinated solute and a fluorinated self assembled monolayer (SAM) are both more hydrophobic than a hydrocarbon solute and a hydrocarbon SAM simply because they are "fatter" i.e. have greater molecular cross-sectional area. We have also found that due to the strong tendency of water to minimize disruptions to its hydrogen bonded network, the structure of water is essentially refractory to the electrostatic nature of hydrophobic solutes/surfaces and free-energy of hydration of these surfaces is much more responsive to changes in Lennard-Jones interactions than to electrostatic interactions. However, we did not see any evidence of polar-hydrophobicity in fluorocarbons. From these results, we have been able to explain the high CO_2-philicity and surface activity (in water) of fluorinated hydrocarbons. Further, we have pointed out that since the response of water and CO_2 to polar/quadrupolar moieties is very different, we may be able to design non-fluorous surfactants to lie in the window where they are at once CO_2-philic and hydrophobic.

Bibliography

Alivisatos, A. P. (1996). Semiconductor Clusters, Nanocrystals and Quantum Dots. *Science , 271*, 933-937.

Allada, S. R. (1984). Solubility parameters of supercritical fluids. *Ind. Eng. Chem. Process. Des. Dev. , 23*, 344-348.

Amirfazli, A., & Neumann, A. W. (2004). Status of Three-Phase Line Tension. *Advances in Colloid and Interface Science , 110*, 121-141.

Anand, M., Bell, P. W., Fan, X., Enick, R. M., & Roberts, C. B. (2006). Synthesis and Steric Stabilization of Silver Nanoparticles in Neat Carbon Dioxide Solvent Using Fluorine-Free Compounds. *J. Phys. Chem. B* , 14693-14701.

Anand, M., You, S.-S., Hurst, K. M., Saunders, S. R., Kitchens, C. L., Ashurst, W. R., et al. (2008). Thermodynamic Analysis of Nanoparticle Size selective fractionation using Gas-expanded liquids. *Ind. Eng. Chem. Res. , 47*, 553-559.

Berendsen, H. J., Grigera, J. R., & Straatsma, T. P. (1987). The Missing Term in Effective Pair Potentials. *J. Phys. Chem. , 91*, 6269-6271.

(2000). Physical Chemistry. In R. S. Berry, S. A. Rice, & J. Ross. Oxford: Oxford University Press.

Biffinger, J. C., Kim, H. W., & DiMagno, S. G. (2004). The Polar Hydrophobicity of Fluorinated Compounds. *ChemBioChem , 5*, 622-627.

Blokzijl, W., & Engberts, J. B. (1993). *Angew Chem Int Ed. , 32*, 1545-1579.

Brust, M., Walker, M., Bethell, D., Schiffrin, D. J., & Whyman, R. (1994). Synthesis of Thiol-Derivatized Gold Nanoparticles in a Two phase Liquid-Liquid System. *J. Chem. Soc. Chem. Comm* , 801-802.

BYU DIPPR Thermophysical Properties Laboratory. (n.d.). *Property Calculator*. Retrieved 10 21, 2009, from DIPPR Physical and Thermodynamic Properties: http://dippr.byu.edu/public/

Cece, A., Jureller, S. H., Kerschner, J. L., & Moschner, K. F. (1996). Molecular Modelling Approach for Contrasting the Interaction of Ethane and Hexafluoroethane with Carbon Dioxide. *J. Phys. Chem. , 100*, 7435-7439.

Chandler, D. (2005). Interfaces and the driving force of hydrophobic assembly. *Nature , 437*, 640-647.

Chang, S.-C., Lee, M.-J., & Lin, H.-M. (2007). Nanoparticles formation for metallocene catalyzed cyclic olefin copolymer via a continuous supercritical anti-solvent process. *J. Supercritical Fluids* , 420-432.

Chapoy, A., Mokraoui, S., Valtz, A., Richon, D., Mohammadi, A. H., & Tohidi, B. (2004). Solubility Measurement and Modelling for the System of Propane-Water from 277.6 to 368.16K. *Fluid Phase Equilibria , 226*, 213-220.

Cheng, Y.-K., & Rossky, P. j. (1998). Surface Topography Dependence of Biomolecular Hydrophobic Hydration. *Nature , 392*, 696-699.

Clarke, N. Z., Waters, C., Johnson, K. A., Satherley, J., & Schiffrin, D. J. (2001). Size-Dependent Solubility of Thiol-Derivatized Gold Nanoparticles in Supercritical Ethane. *Langmuir* , 6048-6050.

Cohen-Atiya, M., & Mandler, D. (2003). Studying thiol adsorption on Au, Ag and Hg surfaces by potentiometric measurements. *J. Electroanalytical Chemistry , 550-551*, 267-276.

Costa Gomes, M. F., & Padua, A. A. (2003). Interactions of CO2 with Liquid Fluorocarbons. *J. Phys. Chem. B , 107*, 14020-14024.

da Rocha, S. R., Dickson, J., Cho, D., Rossky, P. J., & Johnston, K. P. (2003). Stubby Surfactants for Stabilization of Water and CO2 Emulsions: Trisiloxanes. *Langmuir* , 3114-3120.

da Rocha, S. R., Johnston, K. P., & Rossky, P. J. (2002). Surfactant Modified CO2-Water Interface: A Molecular View. *J. Phys. Chem. B* , 13250-13261.

Dardin, A., DeSimone, J. M., & Samulski, E. T. (1998). J. Phys. Chem. B. *Fluorocarbons dissolved in Supercritical Carbon Dioxide. NMR Evidence for Specific Solute-Solvent Interactions , 102*, 1775-1780.

DeSimone, J. M. (2002). Practical Approaches to Green Solvents. *Science , 297*, 799-803.

DeSimone, J. M., Maury, E. E., Menceloglu, Y. Z., McClain, J. B., Romack, T. J., & Combes, J. R. (1994). Dispersion Polymerizations in Supercritical Carbon Dioxide. *Science , 265*, 356.

DeSimone, J., & Wells, S. L. (2001). CO2 Technology Platform: An important tool for environmental problem solving. *Angew. Chem. Int. Ed. , 40*, 518-527.

Dickson, J. P., Smith, P. G., Dhanuka, V. V., Srinivasan, V., Stone, M. T., Rossky, P. J., et al. (2005). Interfacial Properties of Fluorocarbon and Hydrocarbon Phosphate Surfactants at the Water-CO2 Interface. *Ind. Eng. Chem. Res. , 44*, 1370-1380.

Diep, P., Jordan, K. D., Johnson, J. K., & Beckman, E. J. (1998). CO2-Fluorocarbon and CO2-Hydrocarbon Interactions from First Principle Calculations. *J. Phys. Chem. A , 102*, 2231-2236.

Dixon, D. J., Johnston, K. P., & Bodmeier, R. A. (2004). Polymeric Materials Formed by Precipitation with a Compressed Fluid Antisolvent. *AIChE Journal* , 127-139.

Duncan, D., Li, D., Gaydos, J., & Neumann, A. W. (1995). Correlation of Line Tension and Solid-Liquid Interfacial Tension From Measurement of Drop Size Dependence of Contact Angles. *J. Colloid and Interface Science , 169*, 256-261.

Eastoe, J., Gold, S., & Steytler, D. C. (2006). Surfactants for CO2. *Langmuir , 22*, 9832-9842.

Essmann, U., Perera, L., Berkowitz, M. L., Darden, T., Lee, H., & Pedersen, L. G. (1995). A smooth particle mesh ewald potential. *J. Chem. Phys. , 103*, 8577-8592.

Evans, R., Marconi, U. M., & Tarazona, P. (1986). Fluids in narrow pores: Adsorption, capillary condensation, critical points. *J. Chem. Phys. , 84* (4), 2376-2399.

Fan, C. F., & Cagin, T. (1995). Wetting of Crystalline Polymer Surfaces: A molecular dynamics simulation. *J. Chem. Phys. , 103* (20), 9053-9061.

Fan, X., McLeod, M. C., Enick, R. M., & Roberts, C. B. (2006). Preparation of Silver Nanoparticles via Reduction of a Highly CO2 Soluble Hydrocarbon Based Metal Precursor. *Ind. Eng. Chem. Res. , 45*, 3343-3347.

Fenter, P., Eisenberger, P., Li, J., Camillone III, N., Bernasek, S., & Scoles, G. (1991). Surface of n-octadecanethiol self-assembled on Ag(111) surface: An Incommensurate Monolayer. *Langmuir , 7*, 2013-2016.

Fernandez-Nieves, A., Fernandez-Barbero, A., Vincent, B., & de las Nieves, F. J. (2001). Reversible Aggregation of Soft Particles. *Langmuir , 17* (6), 1841-1846.

Flyvbjerg, H., & Petersen, H. G. (1989). Error Estimates on Averages of Correlated Data. *J. Chem. Phys.* , 461-466.

Frenkel, D., & Smit, B. (2002). *Understanding Molecular Simulation.* Academic Press.

Gao, J., Luedtke, W. D., & Landman, U. (1997). Structure and Solvation Forces in Confined Films: Linear and branched alkanes. *J. Chem. Phys. , 106* (10), 4309-4318.

Gao, J., Qiao, S., & Whitesides, G. M. (1995). Increasing Binding Constants of Ligands to Carbonic Anhydrase by using "Greasy Tails". *J. Med. Chem. , 38*, 2292-2301.

Gatica, S. M., Li, H. I., Trasca, R. A., Cole, M. W., & Diehl, R. D. (2008). Xe adsorption on C60 monolayer on Ag(111). *Phys. Rev. B , 77*, 045414.

Giovambattista, N., Debenedetti, P. G., & Rossky, P. J. (2007). Effect of Surface Polarity on Water Contact Angle and Interfactial Hydration Structure. *J. Phys. Chem. B , 111*, 9581-9587.

Gough, C. A., Pearlman, D. A., & Kollman, P. (1993). Calculations of the relative free energy of aqueous solvation of several fluorocarbons: A test of the bond potential of mean force correction. *J. Chem. Phys. , 99* (11), 9103-9110.

Graupe, M., Takenaga, M., Thomas, K., Colorado Jr, R., & Lee, T. R. (1999). Oriented Surface Dipoles Strongly Influence. *J. Am. Chem. Soc. , 121*, 3222-3223.

Gupta, G., Shah, P. S., Zhang, X., Saunders, A. E., Korgen, B. A., & Johnston, K. P. (2005). Enhanced Infusion of Gold Nanocrystals into Mesoporous Silica with Supercritical Carbon Dioxide. *Chem. Mater.* , 6728-6738.

Harris, J. G., & Yung, K. H. (1995). Carbon Dioxide's Liquid-Vapour Coexistence Curve and Critical Properties as predicted by a Simple Molecular Model. *J. Phys. Chem.* , 12021-12024.

Harrison, K., Goveas, J., Johnston, K. P., & O'Rear, E. A. (1994). Water in Carbon Dioxide Microemulsion with a Fluorocarbon-Hydrocarbon Hybrid Surfactant. *Langmuir , 10*, 3536.

Hess, B. (2002). Determining the shear viscosity of model liquids from molecular. *J. Chem. Phys. , 116* (1), 209-217.

Hess, B. (2007). P-lincs: A parallel linear constraint solver for molecular simulation. *J. Chem. Theory Comp. , 4*, 116-122.

Hrivi, J. T., & Pakkanen, T. A. (2006). Molecular Dynamic Simulations of Water Droplets on Polymer Surfaces. *J. Chem. Phys. , 125*, 144712-.

http://webbook.nist.gov/chemistry/fluid/. (n.d.). Retrieved 2009, from NIST Chemistry Webbook.

Humphrey, W., Dalke, A., & Schulten, K. (1996). VMD-Visual Molecular Dynamics. *J. Molec. Graphics* , 33-38.

Israelachvilli, J. (1992). *Intermolecular and Surface Forces* (2nd Edition ed.). Elsevier Science & Technology Books.

Jadzinsky, P. D., Calero, G., Ackerson, C. J., Bushnell, D. A., & Kornberg, R. D. (2007). Structure of a Thiol Monolayer-Protected Gold Nanoparticle at 1.1A Resolution. *Science , 318*, 430-433.

Jang, S. S., Blanco, M., Goddard III, W. A., Cladwell, G., & Ross, R. B. (2003). The Source of Helicity in Perfluorinated N-Alkanes. *Macromolecules , 36*, 5331-5341.

Johnston, K. P., & da Rocha, S. R. (2009). Colloids in Supercritical Fluids over the last 20 years and future directions. *J. Supercrit. Fluids , 47*, 523-530.

Johnston, K. P., Harrison, K. L., Clarke, M. J., Howdle, S. M., Heitz, M. P., Bright, F. V., et al. (1996). Water in Carbon Dioxide Microemulsions: A New Environment for Hydrophiles including Proteins. *Science* (271), 624.

Jorgensen, W. L. (2002). Private Communication.

Kirsch, P. (2004). *Modern Fluoroorganic Chemistry.* Weinheim: Wiley-VCH.

Korgel, B. A., Fullam, S., Connolly, S., & Fitzmaurice, D. (1998). Assembly and Self-Organization of Silver Nanocrystal Superlattices: Ordered "Soft Spheres". *J. Phys. Chem. B* , 8379-8388.

Krafft, M. P., & Riess, J. G. (2007). Perfluorocarbons: Life Sciences and Biomedical Uses. *J. Polymer Science A: Polymer Chemistry , 45* (7), 1185-1198.

Lee, C. Y., McCammon, J. A., & Rossky, P. J. (1984). The Structure of Liquid Water at an extended hydrophobic surface. *J. Chem. Phys. , 80* (9), 4448-4455.

Li, X., Li, J., Eleftheriou, M., & Zhou, R. (2006). Hydration and Dewetting near Fluorinated Superhydrophobic Plates. *J. Am. Chem. Soc. , 128*, 12439-12447.

Li, X.-M., Reinhoudt, D., & Crego-Calama, M. (2007). What do we need for a superhydrophobic surface? A review on the recent progress in preparation of superhydrophobic surfaces. *Chem. Soc. Rev. , 36*, 1350-1368.

Louis, A. A., Allahyarov, E., Lowen, H., & Roth, R. (2002). Effective force in colloidal mixtures: From depletion attraction to accumulation repulsion. *Phys. Rev. E* , 61407-61411.

Martin, M. G., & Siepmann, J. I. (1998). Transferable Potentials for Phase Equilibria. 1. United-Atom Description of n-Alkanes. *J. Phys. Chem. B* , 2569-2577.

Meredith, J. C., Sanchez, I. C., Johnston, K. P., & de Pablo, J. J. (1998). Simulation of Structure and Interaction Forces for Surfaces Coated with Grafted Chains in a Compressible Solvent. *J. Chem. Phys.* , 6424-6434.

Mohammadi, A. H., Chapoy, A., Tohidi, B., & Richon, D. (2004). Measurements and Thermodynamic Modelling of Vapour-Liquid Equilibria in Ethane-Water Systems from 274.26 to 343.08K. *Ind. Eng. Chem. Res. , 43*, 5418-5424.

Mukerjee, P., & Handa, T. (1981). Adsorption of Fluorocarbon and Hydrocarbon surfactants to Air-Water, Hexane-Water and Perfluorohexane-Water Interfaces. Relative Affinities and Fluorocarbon-Hydrocarbon Non-ideality effects. *J. Phys. Chem. , 85* (15), 2298-2303.

Murray, C. B., Norris, D. J., & Bawendi, M. G. (1993). Synthesis and Characterization of Nearly Monodisperse CdE (E=S, Se, Te) Semiconductor Nanocrystallites. *J. Am. Chem. Soc , 115*, 8706-8715.

Myers, A. L., & Prausnitz, J. M. (1965). Thermodynamics of Solid Carbon Dioxide in liquids at low temperatures. *Ind. Eng. Chem. Fundam. , 4*, 209.

Nicholls, A., Sharp, K. A., & Honig, B. (1991). Protein Folding and Association: Insights from Interfacial and Thermodynamic Properties of Hydrocarbons. *Proteins: Stuc. Func. and Genet. , 11*, 281-296.

Nicholls, A., Sharp, K. A., & Honig, B. (1991). *Software: SURFace Algorithms*. Retrieved 2009, from http://wiki.c2b2.columbia.edu/honiglab_public/index.php/Software:SURFace_Algorithms

Nosonovsky, M., & Bhushan, B. (2009). Superhydrophobic Surfaces and Emerging Applications: Non-adhesion, energy, green-engineering. *Current Opinion in Colloid and Interface Science , 14*, 270-280.

O'Neill, M. L., Cao, Q., Fang, M., Johnston, K. P., Wilkinson, S. P., Smith, C. D., et al. (1998). Solubility of homopolymers and copolymers in carbon dioxide. *Ind. Eng. Chem. Res. , 37*, 3067-3079.

Patel, N., & Egorov, S. A. (2007). Interactions between sterically stabilized nanoparticles in supercritical fluids: A simulation study. *J. Chem. Phys. , 126*, 054706.

Peguin, R. P., & da Rocha, S. R. (2008). Solvent-Solute Interactions in Hydrofluoroalkane Propellants. *J. Phys. Chem. B , 112*, 8084-8094.

Pelley, J. (2004, December 1). Canada Moves to Eliminate PFOS Stain Repellants. *Environmental Science and Technology* , 452A.

Potluri, V. K., Xu, J., Enick, R., Beckman, E., & Hamiltion, A. D. (2002). Peracylated Sugar Derivatives Show High Solubility in Liquid and Supercritical Carbon Dioxide. *Organic Letters* , 2333-2335.

Potter, S. C., Tildesley, D. J., Burgess, A. N., & Rogers, S. C. (1997). A transferable potential model for the liquid-vapour equilibria of fluoromethanes. *Molecular Physics , 92* (5), 825-833.

Preuss, M., & Butt, H.-J. (1998). Measuring the Contact Angle of Individual Colloidal Particles. *J. Colloid and Interface Science , 208*, 468-477.

Rabani, E., & Egorov, S. A. (2002). Integral Equation Theory for the Interactions between Passivated Nanocrystals in Supercritical Fluids: Solvophobic and Solvophilic Cases. *J. Phys. Chem. B* , 6771-6778.

Resnati, G. (1993). Synthesis of Chiral and Bioactive Fluoroorganic Compounds. *Tetrahedron , 49* (42), 9385-9445.

Richmond, T. J. (1984). Solvent Accessible Surface Area and Excluded Volume in Proteins - Analytical Equations for Overlapping Spheres and Implications for the Hydrophobic Effect. *J. Mol. Biology , 178* (1), 63-89.

Rosen, M. J. (1972). The relationship of structure to properties in surfactants. *J. American Oil Chemist's Society , 49* (5), 293-297.

Rossen, W. R. (1996). Foams: Theory, Measurements and Applications. In R. K. Prudhomme, & S. A. Khan (Eds.). New York: Dekker.

Rovida, G., & Pratesi, F. (1981). *Surf. Sci. , 104*, 609.

Sagisaka, M., Koike, D., Mashimo, Y., Yoda, S., Takebayashi, Y., Furuya, T., et al. (2008). Water/Supercritical Carbon Dioxide Microemulsions with Mixed Surfactant Systems. *Langmuir , 24*, 10116-10122.

Sarbu, T., Styranec, T., & Beckman, E. J. (2000). Non-fluorous polymers with high solubility in supercritical CO2 down to low pressures. *Nature* , 165-168.

Saunders, A. E., & Korgel, B. A. (2004). Second Virial Coefficient Measurements of Dilute Gold Nanocrystal Dispersions Using Small Angle X-ray Scattering. *J Phys Chem B* , 16732-16738.

Saunders, A. E., Shah, P. S., Park, E. J., Lim, K. T., Johnston, K. P., & Korgel, B. A. (2004). Solvent Density Dependent Steric Stabilizaton of Perfluoropolyether-Coated Nanocrystals in Supercritical Carbon Dioxide. *J. Phys. Chem. B* , 15969-15975.

Scharlin, P., & Battino, R. (1995). Solubility of CCl2F2, CClF3, CF4 and CH4 in Water and Seawater at 288.15-303.15K and 101.325 kPa. *J. Chem. Eng. Data , 40*, 167-169.

Schmidt, M. W., Baldridge, K. K., Boatz, J. A., Elbert, S. T., Gordon, M. S., Jensen, J. H., et al. (1993). General Atomic and Molecular Electronic Structure System. *J. Comput. Chem. , 14*, 1347-1363.

Schoen, M., & Diestler, D. J. (1998). Analytical Treatment of Simple Fluid Adsorbed in Slit Pore. *J. Chem. Phys.* , 5596-5606.

Sellers, H., Ulman, A., Shnidman, Y., & Eilers, J. E. (1993). Structure and Binding of Alkanethiolates on Gold and Silver Surfaces: Implications for Self-Assembled Monolayers. *J. Am. Chem. Soc. , 115*, 9389-9401.

Shah, P. S. (2003). *Nanocrystal Stabilization, Synthesis and Assembly using Supercritical Fluids.* Austin: University of Texas at Austin.

Shah, P. S., Hanrath, T., Johnston, K. P., & Korgel, B. A. (2004). Nanocrystal and Nanowire Synthesis and Dispersability in Supercritical Fluids. *J. Phys. Chem. B* , 9574-9587.

Shah, P. S., Holmes, J. D., Doty, R. C., Johnston, K. P., & Korgel, B. A. (2000). Steric Stabilization of Nanocrystals in Supercritical Carbon Dioxide Using Fluorinated Ligands. *J. Am. Chem. Soc.* , 4245-4246.

Shah, P. S., Holmes, J. D., Johnston, K. P., & Korgel, B. A. (2002). Size-Selective Dispersion of Dodecanethiol-Coated Nanocrystals in Liquid and Supercritical Ethane by Density Tuning. *J. Phys. Chem. B* , 2545-2551.

Shah, P. S., Husain, S., Johnston, K. P., & Korgel, B. A. (2002). Role of Steric Stabilization on the Arrested Growth of Silver Nanocrystals in Supercritical Carbon Dioxide. *J. Phys. Chem. B* , 12178-12185.

Shah, P. S., Husain, S., Johnston, K. P., & Korgel, B. A. (2002). Role of Steric Stabilization on the Arrested Growth of Silver Nanocrystals in Supercritical Carbon Dioxide. *J. Phys. Chem. B , 106*, 12178-12185.

Smith, W. F., & Forester, T. R. (2003). DLPOLY 2.15. Daresbury, Warrington, U.K.: Daresbury Laboratories.

Song, W., Rossky, P. J., & Maroncelli, M. (2003). Modelling alkane+pefluoroalkane interactions using all-atom potentials: Failure of usual combining rules. *J. Chem. Phys. , 119* (17), 9145-9162.

Stone, M. T., da Rocha, S. R., Rossky, P. J., & Johnston, K. P. (2003). Molecular Differences between Hydrocarbon and Fluorocarbon Surfactants at the CO2/Water Interface. *J. Phys. Chem. B* , 10185-10192.

Sun, S., & Murray, C. B. (1999). Synthesis of Monodisperse Cobalt Nanocrystals and their Assembly into Magnetic Superlattices. *J. Applied Phys.* , 4325-4330.

Tarazona, P., Marconi, U. M., & Evans, R. (1987). Phase Equilibria of Fluid Interfaces and Confined Fluids. *Molecular Physics , 60* (3), 573-595.

Ulman, A. (1989). *J. Mater. Ed. , 11*, 205.

Vafaei, S., & Podowski, M. Z. (2005). Theoretical Analysis on the effect of liquid droplet geometry on contact angle. *Nuclear Engineering and Design , 235*, 1293-1301.

van der Spoel, D., Lindahl, E., Hess, B., Groenhof, G., Mark, A. E., & Berendsen, H. J. (2005). GROMACS: Fast, Flexible and Free. *J. Comp. Chem. , 26*, 1701-1718.

Vidali, G., Ihm, G., Kim, H. Y., & Cole, M. W. (1991). *Surf. Sci. Rep , 12*, 135.

Weast, R. C., Lide, D. R., Astle, M. J., & Beyer, W. H. (1990). CRC Handbook of Chemistry and Physics. Boca Raton FL: CRC Press Inc.

Wen, W.-Y., & Muccitelli, J. A. (1979). Thermodynamics of some Perfluorocarbon Gases in water. *J. Soln. Chem. , 8* (3), 225-246.

Werder, T., Walther, J. H., Jaffe, R. L., Halicioglu, T., & Koumoutsakos, P. (2003). On the Water-Carbon Interaction for use in molecular dynamics simulation of Graphite and Carbon Nanotubes. *J. Phys. Chem. B , 107*, 1345-1352.

Widom, B. (1963). Some topics in the theory of fluids. *J. Chem. Phys. , 39*, 2808-2812.

Wu, L., & da Rocha, S. R. (2008). Application of the Atomic-Force Microscope in the Development of Propellant-based Inhalation Formulations. *Kona-Powder and Particle , 26*, 106-128.

Yee, G. G., Fulton, J. L., & Smith, R. D. (1992). Fourier Transform Infrared Spectroscopy of Molecular Interactions of Heptafluoro-1-butanol or 1-Butanol in Supercritical Carbondioxide and Supercritical Ethane. *J. Phys. Chem. , 96* (15), 6172-6181.

Zichi, D. A., & Rossky, P. J. (1985). Equilibrium Solvation Structure for Solvent-Separated Hydrophobic Bond. *J. Chem. Phys. , 83* (2), 797-808.

Vita

Vishwanath Haily Dalvi was born in Mumbai, India on 12th November 1980 to Haily and Ujjwala Dalvi. He earned his Bachelor of Chemical Engineering (B.Chem.Engg.) degree from the Institute of Chemical Technology, Mumbai (then called the Mumbai University Department of Chemical Technology) in June of 2002. After a short stint in the laboratory of Prof. J. B. Joshi at ICT, he enrolled at the University of Twente in January 2003 receiving an M.S. in Process Design in March 2005. He worked as a contractor with Shell Global Solutions, Amsterdam till August 2005 when he enrolled as a graduate student at Chemical Engineering Department of the University of Texas at Austin where he conducted research under the supervision of Prof. Peter Rossky. He will receive his Ph.D. in Chemical Engineering in December 2009.

Permanent Address: G-12, Saraswat Colony
Sitladevi Temple Road,
Mahim, Mumbai – 400016
India.

This dissertation was typed by Vishwanath Haily Dalvi.